Dissertation
submitted to the
Combined Faculties for the Natural Sciences and for Mathematics
of the Ruperto-Carola University of Heidelberg, Germany
for the degree of
Doctor of Natural Sciences

presented by
Dipl. Phys. Björn Magnus Voss
born in Herdecke

Day of oral examination: 2th of May 2012

Novel single Camera Techniques for 3D3C Lagrangian Trajectory Measurements in Interfacial Flows

Referees:
Priv.-Doz. Dr. CHRISTOPH S. GARBE
Prof. Dr. CAMERON TROPEA

Abstract: This thesis presents two single camera *Particle Streak Velocimetry* (PSV) techniques that were purpose-built for the measurement of Lagrangian *three-dimensional three-component* (3D3C) flow information in the turbulent boundary layer of transparent interfaces. Both techniques are based on a particle streak extraction routine that enables a sub-pixel precise extraction of individual particle trajectories. A periodical intensity modulation of the illumination was implemented to increase the temporal resolution of the extracted Lagrangian trajectories. The achieved high spatial and temporal resolution enables quantitative measurements of Lagrangian flow characteristics in the interfacial region of turbulent flow fields. The first measurement technique, called *bichromatic Particle Streak Velocimetry* (bPSV), uses an absorbing dye and a two-wavelength LED illumination to resolve three-dimensional data that are needed for the extraction of 3D3C trajectories. In the second measurement technique the depth estimation is realized by means of a *focused plenoptic camera* that records long time exposure light fields. Both techniques were applied to measure interfacial flow fields in a turbulent *Rayleigh-Bénard* (RB) convection. On the basis of the Lagrangian particle trajectories obtained in the bPSV measurements, acceleration statistics and particle pair dispersion statistics were evaluated. A comparison of the Lagrangian acceleration distribution with two recently published models yielded good agreements. In the extracted Lagrangian particle pair dispersion, transitions between three turbulent regimes (i.e. the *Batchelor* regime, the *Richardson-Obukhov* (R-O) regime and the diffusive regime) were observed.

Zusammenfassung: Die vorliegende Arbeit befasst sich mit zwei neuartigen (3D3C) Geschwindigkeitsmesssystemen für komplexe 3D-Strömungen in der turbulenten Grenzschicht an transparenten Grenzflächen. Beide Systeme basieren auf der Messung von *Particle Streak Velocimetry* (PSV)-Daten und auf einem sub-pixel genauen Extraktionsalgorithmus für die Extraktion von Lagrange'schen Einzeltrajektorien. Eine periodische Intensitätsmodulation der Beleuchtung wurde benutzt, um das zeitliche Auflösungsvermögen der Systeme zu erhöhen. Die hohe zeitliche und räumliche Auflösung der so bestimmten Partikeltrajektorien ermöglicht die Extraktion von Lagrange'schen Fluss-Charakteristiken in turbulenten Grenzschichten. In der so genannten *bichromatic Particle Streak Velocimetry* (bPSV)-Messtechnik wird ein absorbierender Farbstoff in Kombination mit einer Zwei-Wellenlängen LED-Beleuchtung verwendet, um Tiefeninformationen zu messen, die für eine Extraktion von Lagrange'schen (3D3C) Trajektorien benötigt werden. Das zweite Messsystem nutzt eine fokussierte Plenoptische Kamera zur Messung von Lichtfeldern für die Tiefenschätzung. Beide Geschwindigkeitsmesssysteme wurden eingesetzt, um die wasserseitige Grenzschicht an der freien Oberfläche einer turbulenten *Rayleigh-Bénard* (RB) Konvektion zu vermessen. Die Ergebnisse der bPSV-Messung wurden im Folgenden verwendet, um Lagrange'sche Beschleunigungsstatistiken und Lagrange'sche Paar-Separationsstatistiken zu berechnen. Die so gewonnenen Beschleunigungsstatistiken zeigen eine gute Übereinstimmung mit zwei kürzlich veröffentlichten Modellen, und in den Separationsstatistiken wurden in der Theorie vorhergesagte Übergänge zwischen dem *Batchelor* Regime, dem *Richardson-Obukhov* (R-O) Regime und dem anschließenden diffusen Regime beobachtet.

Für meine wundervolle Agnieszka.

Contents

1 Introduction

1.1 Motivation

Processes that control the transport of momentum, heat and mass across fluid boundary layers are of major importance in many industrial applications, environmental processes and in fluid-dynamic research. Since turbulent transport in the boundary layer of an interface plays a major role in the understanding of these processes, many investigators focused on the theoretical description of turbulent flow fields in the presence of an interface as well as on the development of numerical and experimental techniques. Although all these efforts have spawn a detailed theoretical description, e.g. the advection-diffusion equation and the Navier-Stokes equation, the physical workings are far from being completely understood.

A proper understanding of interfacial turbulent flow fields is, for example, important for many industrial applications and in the field of engineering. One example from this field is the experimental study by Burgmann et al. (2008), who recorded volumetric measurements of the turbulences occurring in the boundary layer of an airfoil that moves fast in a surrounding medium. Furthermore, interfacial flow fields are of major importance in many industrial applications when it comes to the exchange of heat between a fluid and an interface. This happens in various applications such as combustion engines, film-cooling systems or heat exchangers (Cho and Greene, 2011; Hanjalić and Launder, 2011).

Interfacial flow field measurements can also be found in the field of medical research. This is due to the fact that many biological processes are influenced by the movement of the surrounding medium. Cell biological studies by (Akimoto et al., 2000; Butler et al., 2001) showed for example that the membrane fluidity as well as the proliferation of aortic endothelial cells depend on the shear stress caused by the surrounding fluid. Another example for the importance of interfacial flow fields in the field of medical research is presented by Kim et al. (2006) who showed that the interfacial flow fields at the walls of blood vessels have a large influence on the thrombus formation.

Another example is the influence of interfacial transport processes on the air-sea heat and gas exchange as described by Garbe et al. (2004). In this study thermographic image sequences were analyzed and a so-called "surface renewal model" was proposed that describes the exchange rates of mass and heat by means of a surface renewal rate. Another study in the same field published by Banner and Peirson (1998) used a wind-wave tank to measure interfacial flow structures below a wind-driven air-water

surface. A better understanding of this air-sea interaction that is controlled by processes in the turbulent interfacial region can help to improve the predictions of present climate models (Wanninkhof et al., 2009).

Due to the chaotic nature of turbulent flow fields, an analysis can not be accomplished by means of the equations of motion developed for the characterization of viscous non-turbulent flow fields. Therefore, the concepts for the analysis of turbulence have changed from the thorough description of individual turbulences towards the formulation of theoretical models that are valid for these classes of turbulences, i.e. boundary layer flow fields, jets, buoyancy driven turbulence and wakes. These models typically rely on the definition of characteristic measures describing the turbulence and on the definition of scaling variables. Scaling variables allow the formulation of scale-invariant turbulence models that provide a description of entire turbulence classes and allow a comparison of turbulent processes observed on different scales. Up to now, turbulence models depend inherently on numerical and experimental studies that are needed to determine correct model parameters for different boundary conditions and to validate the correctness of the models.

Two general strategies were followed in literature for the experimental measurement of turbulence characteristics in flow fields. One strategy is based on the measurement of Eulerian flow fields. The main idea of all approaches following this strategy is to measure flow fields in a Eulerian frame of reference and to extract the sought characteristics by a statistical analysis of these measurements. The second strategy for the analysis of turbulence is based on the extraction of Lagrangian flow information typically obtained from particle tracking experiments. Methods based on this strategy commonly use a statistical analysis of the measured Lagrangian particle trajectories for the extraction of characteristic measures that describe the turbulence.

While transport processes in an isotropic, homogeneous turbulence can be estimated from a set of model assumptions and scaling parameters, the estimation of turbulent transport mechanisms in the boundary layer of an interface presents a special challenge. This class of turbulences is no longer isotropic since the turbulent eddies that move perpendicular to the interface are inhibited in the interfacial region. A description of the turbulent processes by means of the common scaling parameters is also difficult since the scales in the direction of the interface may also differ from the scales in the perpendicular direction due to the anisotropy.

Therefore, the formulation of models for the description of interfacial turbulence is crucially dependent on flow measurements in the boundary layer. These measurements are needed for a validation of the models and to determine correct model parameters. Because of the intrinsic three-dimensionality and the anisotropic nature of turbulent boundary layer flow fields, a proper characterization needs to be based on volumetric measurements that incorporate all three velocity-components, i.e. *three-dimensional three-component* (3D3C) information.

Common methods that aim to solve the challenging task of measuring 3D3C flow information can be distinguished according to the technique used to obtain three-dimensional (3D) velocity information and the methods used to measure volumetric datasets. The most popular method to access *three-components* (3C) of the velocity field is to measure the out-of-plane velocity using stereoscopic methods (Prasad, 2000), extended by a technique called *multi-plane* Particle Image Velocimetry *(PIV)* using multiple laser sheets (Brücker, 1996; Cenedese and Paglialunga, 1989; Kähler and Kompenhans, 2000; Liberzon et al., 2004; Müller et al., 2001) or intensity graded light sheets (Dinkelacker et al., 1992) for the reconstruction of the third velocity component.

In the recent past many methods were proposed to access volumetric information from 3D flow fields. This was achieved using holographic measurements (Hinsch, 2002; Sheng et al., 2008), by combining PIV with *Doppler global velocimetry* (PIV/DGV) (Wernet, 2004), using tomography (Elsinga et al., 2006; Schröder et al., 2008), defocussing-based approaches (Pereira et al., 2000, 2007; Willert and Gharib, 1992), scanning-light-sheet methods (Brücker, 1995; Burgmann et al., 2008; Hoyer et al., 2005) and absorption based methods (Berthe et al., 2010; Jehle and Jähne, 2008).

Another requirement that arises when it comes to the measurement in thin boundary layers concerns the spatial resolution perpendicular to the boundary layer. This resolution has to be very high because the boundary layer thicknesses observed in the laboratory environment are typically small compared to the characteristic length scale of turbulence below the boundary region.

Unfortunately, most of the previously named 3D3C techniques are optimized for a fixed measurement volume that is typically cubic or hexahedral shaped. Common workarounds that enable a restriction of these volumes, e.g. by using absorbing dyes, do not increase the spatial resolution of the data in the restricted volume.

Measurement methods that are capable to fulfill all previously described requirements for measurements of interfacial turbulences are rare. The most promising approaches with respect to interfacial 3D3C measurements are a stereo-based approach by Turney et al. (2009), an absorption-based technique presented by and Jehle and Jähne (2008) and a holographic approach by Sheng et al. (2008). These methods rely on costly setups using high-speed cameras and complex illumination setups. Moreover, the stereo-based and the holographic approach depend on an additional interface tracking technique since they record flow information in an absolute frame of reference that needs to be related to an interface position.

Therefore, this thesis aims to the development of alternative Lagrangian techniques dedicated for the measurement of 3D3C flow fields in interfacial boundary layers. The temporal and spatial resolution of the proposed techniques have to be within the same order of magnitude than the microscales of the observed turbulences to enable a proper characterization of interfacial turbulent flows fields.

1.2 Objectives of this Study

The aim of this study was the development of two techniques dedicated to the volumetric measurement of Lagrangian 3D3C characteristics in the boundary region of a transparent gas-liquid interface. Due to the multiple scales that are present in turbulent interfaces the spatial and temporal resolution has to be of the same order of magnitude as the smallest scales that can be observed in the turbulence. Because of the anisotropic nature of the boundary layer, the method aims to resolve a thin layer of the interfacial region with a high precision in the direction which is perpendicular to the interface. For the extraction of turbulence characteristics based on Lagrangian acceleration statistics, the temporal resolution of the method should be in the same order of magnitude as the time scale defined by the Kolmogorov microscales of turbulence.

Another target during the development was that the method should be based on a single camera setup to make it applicable for situations where the optical access precludes the usage of multiple-camera setups or when the financial resources prohibit such a system. An additional advantage of using a single camera technique is that the calibration effort is much smaller than the effort needed for the setup of a multi-camera solution.

The precision and the applicability of the developed techniques should be assessed by means of test measurements. Additionally, the water-sided interfacial turbulence of *Rayleigh-Bénard* (RB) convection should be characterized by means of the developed methods.

1.3 Outline

The basic concepts, strategies and techniques that were used for the development of the presented 3D3C measurement techniques are outlined in the following paragraphs.

For all particle-based flow measurements that were conducted in the scope of this thesis neutrally buoyant silver coated hollow ceramic spheres with $100\,\mu$m diameter were used for the tracing of turbulent flow fields. Depending on the environment and the expected turbulence, these tracer particles can be replaced by any other reflecting particles that have a diameter smaller than the characteristic length-scale of the observed turbulence.

During the course of this study a single-camera *Particle Streak Velocimetry* (PSV) measurement technique with a volumetric *light-emitting diode* (LED)-illumination was developed. The recorded PSV-sequences contain long-exposure images that show moving particles as streak patterns. To overcome the loss of temporal resolution that is introduced by the long exposure times, a periodical signal of a known frequency was modulated on the light sources. An image of the resulting particle streak patterns that

reflect the periodical modulated illumination is shown in Figure 3.2 on page 41. The periodical gray-value signal along these patterns allows the extraction of the instantaneous particle velocity that can be computed for every point along the center line of the trajectory.

For the resolution of volumetric data two different depth-extraction techniques were developed. The first measurement method is the so-called *bichromatic Particle Streak Velocimetry* (bPSV)-technique. It relies on a *bichromatic depth extraction* approach that was originally proposed by Jehle and Jähne (2008). It uses a single gray-value camera for the acquisition of PSV-image series. An absorbing dye is solved in the fluid for the depth estimation. Afterwards, the depth is computed from the reflected intensities of two light sources that illuminate the particles with different wavelengths. This method makes use of Lambert Beer's Law and the wavelength-dependent absorption characteristic of the dye. It inherently provides depth information relative to the interface, because the illuminating light is only absorbed on its way through the liquid. Additionally, the resolution in z-direction, i.e. perpendicular to the interface, can be adapted by changing the concentration of the absorbing dye. Therefore, it is possible to restrict the measurement volume to thin regions in the boundary layer of an interface.

The second measurement technique developed in the scope of this thesis is called *plenoptic Particle Streak Velocimetry* (pPSV). This technique is based on light field measurements by means of a *focused plenoptic camera*. In this camera a micro-lens array is placed between the camera objective and the sensor array. It samples four-dimensional light fields that comprise directional information as well as intensity information of the incident light. These light fields allow to render depth maps and "all-in-focus" images with an increased focal depth.
The major advantage of this depth extraction technique is that it allows the extraction of *three-dimensional* (3d) data from the light field itself and is thus not dependent on additional cameras, expensive illumination strategies or the use of an absorbing dye. Additionally, the calibration effort is negligible compared to other state of the art techniques for volumetric 3d imaging.

By combining the instantaneous velocity and the horizontal particle trajectories with the depth information obtained from one of the proposed depth extraction techniques, it is possible to compute 3D3C-trajectories of the imaged tracer particles. A subsequent matching routine applied to these data enables a matching of multiple particle streaks to long trajectories that describe the movement of a tracer-particle over multiple images in the recorded PSV-sequences.

On the basis of these long 3D3C particle trajectories several turbulence characteristics such as the Lagrangian acceleration distribution and the 3d Lagrangian two-particle dissipation can be extracted.

To prove the applicability and to validate the precision of the presented measurement techniques, the PSV extraction routine was applied to a set of semi-artificial benchmark data sets that allow to assess the precision of the instantaneous velocity. These data sets were computed based on a set of PIV benchmark-measurements published by Berthe et al. (2010).

After a characterization of the precision that can be expected in the measurements both techniques (i.e. the bPSV-technique and the pPSV-technique) were used to measure the interfacial flow field in the water-sided boundary layer of a turbulent *Rayleigh-Bénard* (RB) convection. The measurement of these turbulent flow fields is a challenging task for many reasons. The two most obvious reasons are:

Firstly, the characteristic length scale of this turbulence is larger than the size of the boundary layer. Therefore, the extraction of proper turbulence characteristics relies on a high resolution in the direction perpendicular to the interface, while the horizontal size of the measurement volume has to be larger than the characteristic length scale of the turbulence.

Secondly, the large difference between the microscopic scale and the characteristic length scale of the turbulence involves a tracking of single particles over long periods of time with a high temporal and spatial resolution. That makes this type of turbulence measurement challenging for any technique.

Nonetheless, it was possible to use the developed method for the extraction of meaningful turbulence characteristics from the boundary layer region. The results are in accordance with the results of other studies aiming the characterization of turbulent processes.

1.3.1 Structure of this Thesis

The present thesis is organized in the following way. An overview over existing methods and studies published in the field of particle-based flow measurements and turbulence analysis is given in Chapter 2 ("Background"). The aim of this chapter is to lay a cornerstone for the understanding of the following chapters, and to justify the need for a dedicated measurement technique to assess 3D3C-information of turbulent processes in the boundary layer various interfaces.
In this context, results of previous numerical studies and experiments will be summarized. This chapter especially focuses on techniques that were used to assess volumetric 3D3C flow information. At this point, a detailed description of the bichromatic depth extraction technique that was developed by Jehle and Jähne (2008) will also be given. In the following section of this chapter the principle of the second depth estimation technique based on a *focused plenoptic camera* will be introduced in detail. A concise knowledge about these methods, their possibilities and shortcomings is vital for an understanding of the challenges that arise when it comes to the measurement of

turbulent flow information in the boundary layer of an interface. Furthermore, this chapter provides the basics for an understanding of the used statistical Lagrangian measures that were extracted within the scope of this thesis.

The basic principles and the underlying concept of the developed measurement techniques are explained in detail in Chapter 3 ("Measurement Technique"). This includes an explanation of mathematical concepts as well as a description of the tensor-based image processing routines and the signal processing algorithms that were implemented. Additionally, this chapter describes the calibration routines that were used for the calibration of both developed depth estimation techniques.

The experimental setup and the hardware used to control the image acquisition, the illumination and the synchronization are explicitly described in Chapter 4 ("Experimental Setup"). Furthermore, this chapter comprises a detailed description of the interaction between all these hardware components. In addition to the description of the experimental setup of the measurement device, this chapter also introduces the setup of the vessel that was used to generate a turbulent RB-convection.

Chapter 5 ("Data Processing") presents the complete chain of operations that was implemented to extract precise and robust flow information from the recorded PSV-sequences. This includes the radiometric and the geometric calibration of the gray-value camera as well as the tensor-based feature extraction and the frequency analysis that yields Lagrangian trajectories. Finally, this chain of operations builds a routine for the statistical evaluation of the measured turbulences that computes a set of Lagrangian characteristics from the measured particle trajectories. In the end, this chapter also describes the computation of the semi-artificial data sets that were used to validate the frequency-based velocity estimation.

All the results obtained from the numerical experiments using the semi-artificial data sets and from the measured characteristics extracted from the turbulent RB convection are summarized and explained in Chapter 6 ("Results and Discussion"). This chapter also provides an approximation of the expected measurement error and a quantitative comparison of the obtained turbulence characteristics with results from previous studies.

Chapter 7 ("Conclusion") summarizes the achievements of this study as well as its results and its shortcomings. Furthermore, this chapter gives a short outlook containing a description of possible modifications and extensions to improve the quality of the extracted turbulence characteristics.

Supplementary content in form of data sheets and tables is bundled in Chapter A ("Appendix") at the very end of this thesis. This additional information is not necessary for a general understanding of this work. Still this work contains some links to these data to provide the ambitious reader with background information.

2 Background

The present chapter provides a conceptual background of the physical properties and the characteristic measures used in this thesis. It starts with a description of turbulent flow fields by means of dimensionless scaling parameters as well as by the commonly used Kolmogorov microscales is explained.

The subsequent section introduces two important turbulence characteristics, i.e. the Lagrangian acceleration statistic and the Lagrangian pair-dispersion statistic.

In the following section a brief introduction to particle-based measurement techniques and their ability for interfacial measurements is given.

The last section in this chapter comprises an introduction to the principle of plenoptic imaging.

2.1 Turbulence

"Big whirls have little whirls,
That feed on their velocity;
Little whirls have lesser whirls,
And so on to viscosity."
(L. F. Richardson)

As mentioned in the introduction of this thesis, the scientific description of turbulent flow fields is based on models that address single turbulence families such as boundary layer flow fields, jets, buoyancy driven turbulence and wakes. Typically, these models use a set of parameters and some scaling variables for the description of a specific turbulence. The use of scaling parameters is well established in the field of fluid mechanics since they allow to adapt models to various boundary conditions determined by external parameter like the fluids viscosity, different temperature gradients or the spatial boundaries of an experiment.

2.1.1 Scaling Parameters

The umbrella term *Rayleigh-Bénard* (RB) convection describes all the buoyancy driven convective flow fields that are heated from below and cooled from above. In the field of fluid-dynamics, RB convections can be seen as a classical problem that is probably

treated in every undergraduate lecture given on fluid-dynamics. Turbulent RB flow fields belong to the most studied and best characterized turbulences that exist. This is because the generation of this kind of turbulence in a laboratory environment is quite simple.

To enable quantitative comparisons of the results obtained in this thesis with the outcome of other studies, we derived several scaling parameters from the measured data.
One of the most prominent scaling parameters used to scale models for the description of convection-driven turbulence is the *Rayleigh Number Ra*. This number describes the relation between the convective heat transfer in a buoyancy-driven turbulent flow field and the conductive heat transfer. In turbulent RB flow fields this parameter is defined as follows:

$$Ra = \frac{\alpha_i g \Delta T H^3}{\nu \kappa}. \tag{2.1}$$

Here α_i is the isobaric thermal expansion coefficient, the gravitational acceleration is given by g, and ΔT is the temperature difference that causes the RB convection. The two parameters in the denominator are material characteristics of the fluid. Here κ is the thermal diffusivity and μ is the kinematic viscosity of the fluid, and H describes the characteristic length-scale of the convection.

A more phenomenological scaling parameter that is often used to scale models describing turbulent RB convections is the dimensionless *Reynolds number Re*. It combines information from the characteristic length scale l and the characteristic velocity u observed in the turbulence with the fluids kinematic viscosity (Ahlers et al., 2009; Tennekes and Lumley, 1992).

$$Re = \frac{ul}{\nu} \tag{2.2}$$

To get a better idea of the meaning of this scaling parameter, one can imagine it as the ratio between the internal forces defined by the product ul and the viscous forces represented by the kinetic viscosity. The characteristic length scale and the characteristic velocity of a turbulence can be estimated from the results of the turbulence measurements. Here l is given by the *integral length scale* that can be approximated by the size of the largest eddies in the turbulent flow field, and u corresponds to the velocities observed within these eddies.
A very detailed review on large scale dynamics in turbulent RB convections and the correlation between heat transfer and the most prominent dimensionless scaling parameters, i.e. the *Rayleigh number*, the *Reynolds number* and the also often used *Prandtl number*, was published by Ahlers et al. (2009). This publication also describes the

dependency of the thermal and the kinetic boundary layer on the previously named scaling parameters.

According to the detailed introduction to ways to characterize turbulent flow fields given in (Tennekes and Lumley, 1992), the next important characteristic measure that can be used to characterize turbulent processes is the dissipation rate of energy. This so-called *energy dissipation rate* $\langle \epsilon \rangle$ can also be approximated from the observed length scales (Tennekes and Lumley, 1992) using:

$$\langle \epsilon \rangle \sim \frac{u^3}{l} \tag{2.3}$$

The above definitions allow the derivation of the well known Kolmogorov microscales that provide a microscopic turbulence scaling by means of a length scale $\eta_{\mathrm{K}} = \left(\nu^3 / \langle \epsilon \rangle \right)^{1/4}$, a time scale $\tau_{\mathrm{K}} = \left(\nu / \langle \epsilon \rangle \right)^{1/2}$ and a velocity scale $u_{\mathrm{K}} = \left(\nu \langle \epsilon \rangle \right)^{1/4}$.

By using the approximation (2.3) and the previously defined dimensionless *Reynolds number* (2.2), these three microscales can also be approximated from the observed characteristic length scales.

$$\eta_{\mathrm{K}} \quad \approx \quad l Re^{-3/4} = \left(\frac{\nu^3 l}{u^3} \right)^{1/4} \tag{2.4}$$

$$\tau_{\mathrm{K}} \quad \approx \quad \frac{l}{u} Re^{-1/2} = \left(\frac{\nu l}{u^3} \right)^{1/2} \tag{2.5}$$

$$u_{\mathrm{K}} \quad \approx \quad u Re^{-1/4} = \left(\frac{\nu u^3}{l} \right)^{1/4} \tag{2.6}$$

These Kolmogorov microscales define a measure for the smallest turbulent structures that are expected to occur in a flow field. The energy contained in these smallest structures is no source for smaller turbulences but dissipates completely by means of viscous processes into thermal energy.

2.1.2 Lagrangian Statistics

On the basis of flow measurements characterizing the movements of single tracer particles in a fluid, Lagrangian statistics can be used to extract characteristic measures for the description of turbulent processes. Most models that describe turbulent processes on the basis of these Lagrangian statistics use the Kolmogorov microscales to provide a scale-invariant description of the underlying dynamics.

The two Lagrangian statistics that will be analyzed within the scope of this thesis are the *three-dimensional* (3d) Lagrangian acceleration statistic and the Lagrangian particle pair separation.

Acceleration Statistics

In a Eulerian frame of reference, the acceleration of a flow field can be defined by the total derivative of the flow velocity.
This can be derived by

$$a_i = \frac{\mathrm{d}v_i}{\mathrm{d}t} \equiv \partial_t v_i + v_k \partial_k v_i. \tag{2.7}$$

It can be seen that the acceleration separates in a Eulerian local acceleration $\partial_t v_i$ and a more global part that is given by a nonlinear advection term $v_k \partial_k v_i$ (Aringazin and Mazhitov, 2004). In this equation $\partial_k = \partial/\partial k$ describes the spatial derivative in the Cartesian reference system of the laboratory, and $\partial_t = \partial/\partial t$ is the temporal derivative. The indices $i, k \in \{1, 2, 3\}$ correspond to the different spatial directions. The indices in this section are used according to *Einsteins summation convention* (Einstein et al., 1916).

The acceleration statistic is a quite meaningful turbulence parameter since it is directly connected to the 3d *Navier-Stokes equation* (NSE) for incompressible flows (Tropea et al., 2007) that is defined by

$$\underbrace{\partial_t v_i}_{\substack{\text{unsteady} \\ \text{acceleration}}} + \underbrace{v_k \partial_k v_i}_{\substack{\text{convective} \\ \text{acceleration}}} = -\frac{1}{\rho} \underbrace{\partial_k p}_{\substack{\text{pressure} \\ \text{gradient}}} + \underbrace{\nu \partial_k^2 v_i}_{\substack{\text{viscous} \\ \text{term}}} + \underbrace{f_i}_{\substack{\text{additional} \\ \text{forcing}}}. \tag{2.8}$$

In this equation ρ is the fluids density, p is the pressure, and ν is the kinematic viscosity. The additional summand f_i describes a forcing that is usually only relevant at large characteristic spatial scales (Aringazin and Mazhitov, 2004).

The NSE can be rewritten with (2.7) including the acceleration into this equation.

$$a_i = -\frac{1}{\rho} \partial_i p + \nu \partial_k^2 v_i + f_i. \tag{2.9}$$

Lagrangian measurement methods such as *Particle Tracking Velocimetry* (PTV) or *Particle Streak Velocimetry* (PSV) are a common tool for the measurement of acceleration characteristics in turbulent flows.

The basic idea of all Lagrangian approaches is to measure time series $x_i(t)$ that describe the position of individual tracer particles. Most approaches use a finite-differences strategy to extract the Lagrangian velocity $u_i(t)$ and the $a_i(t)$ in a subsequent step. These measures can be computed from the first and the second time derivative

$$u_i(t) = \partial_t x_i(t) \tag{2.10}$$
$$a_i(t) = \partial_t^2 x_i(t) \tag{2.11}$$

In his review article on Lagrangian acceleration statistics, Aringazin and Mazhitov (2004) state that the measurement of acceleration statistics in a locally isotropic turbulence requires a very high accuracy of the tracking system. The experiment for the extraction of Lagrangian accelerations should be able to access time scales that are smaller than the Kolmogorov time scale τ_K of the measured turbulence. The underlying aim of all experiments that extract acceleration statistics in turbulent flow fields is to assess information on the pressure gradient term in (2.9).

Recent developments in the field of Lagrangian measurement techniques as well as in the field of *direct numerical simulations* (DNS) have triggered a set of studies focusing on the extraction of Lagrangian acceleration statistics with resolutions that lie in the order of magnitude of the Kolmogorov time scale τ_K.

For a better understanding of the underlying processes, various models were proposed to describe the acceleration statistics of isotropic turbulences. These models mostly focus on the acceleration distribution in turbulences and formulate *Probability Density Functions* (PDF)s that model these distributions on the basis of a set of physical assumptions made on the underlying fluid-mechanical processes. A detailed derivation of the most promising models developed in the recent past is given in a review paper by Aringazin and Mazhitov (2004).

In this thesis we focus on two Lagrangian acceleration distribution models. The first one is based on a phenomenological function that was used to model experimental data in a study made by Voth et al. (2002), and the second one is based on a *Random Intensity of Noise* (RIN) approach, and was derived by Beck (2002, 2003).

The model used in the experimental study by Voth et al. (2002) is based on the observation that the center part of the Lagrangian acceleration histogram shows a Gaussian behavior, while the tails of the distribution extend far beyond those of a normalized Gaussian bell-curve of the same variance. Therefore, this study adds a linear dependency to the width parameter of a Gaussian bell curve. The resulting

Probability Density Function (PDF) used to model the results of this study is given by the following equation.

$$P_I(a) = C_a \exp\left(-\frac{a^2}{\left(1 + |a\beta_a/\sigma_a|^{\gamma_a}\right)\sigma_a^4}\right) \tag{2.12}$$

In this equation C_a is a normalization factor, and σ_a corresponds to the width of the underlying Gaussian distribution. The additional model parameters β_a and γ_a control the flatness of the tails of the distribution.

The second parametrization model used in this thesis was developed on the basis of theoretical considerations based on Tsallis non-extensive statistics (Tsallis, 1988). The major assumption of this model is that the acceleration of infinitesimal fluid particles moving in a fully developed turbulence can be explained by a conditional PDF

$$P_{II}(a) = \int_0^\infty \mathrm{d}\beta P\left(a|\beta\right) f\left(\beta\right). \tag{2.13}$$

The first part of this equation can be derived using the one-dimensional Langevin equation for the Lagrangian acceleration to a Gaussian form (Aringazin and Mazhitov, 2004).

$$P(a|\beta) = C(\beta) \exp\left(-\beta a^2/2\right) \tag{2.14}$$

Here $C(\beta) = \sqrt{\beta/2\pi}$ is a normalization factor.
This approach is based on the idea that the model parameter β is a random parameter that prescribes external statistics. Therefore, this parameter introduces an additional PDF $f(\beta)$ in the Lagrangian acceleration model (2.13).

As motivated in (Aringazin and Mazhitov, 2004) a χ-square distribution of order ($n = 1, 2, 3, \ldots$) is a reasonable assumption for the model parameter β.

$$f\left(\beta\right) = \frac{1}{\Gamma\left(n/2\right)} \left(\frac{n}{2\beta_0}\right)^{n/2} \beta^{n/2-1} \exp\left(-\frac{n\beta}{2\beta_0}\right) \tag{2.15}$$

Using this distribution of the randomly distributed positive parameter β together with the Gaussian distribution given in (2.14) the original PDF (2.13) can be solved to

$$P_{II}\left(a\right) = \frac{C}{\left(a^2 + n/\beta_0\right)^{(n+1)/2}} \tag{2.16}$$

The final extension added to this model is a Gaussian truncation of the power-law tails that automatically arises if one assumes β to contain a non-fluctuating part. This non-fluctuating part is parametrized by a_c in the model derived by Aringazin and Mazhitov (2004).

$$P_{II}\left(a\right) = \frac{C \exp\left(-a^2/a_c^2\right)}{\left(a^2 + n/\beta_0\right)^{(n+1)/2}} \tag{2.17}$$

A more detailed description of this model and alternative RIN models for the description of Lagrangian acceleration statistics can be found in the studies by Voth et al. (2002) and Aringazin and Mazhitov (2004).

Two-Particle Dispersion

The cornerstone for the development of dispersion-based statistical flow characterization was laid by Taylor (1922), who proposed the usage of the Lagrangian single-particle dispersion. His work was also the inspiration for the so-called Lagrangian two-particle dispersion first developed by Richardson (1926). For the quantitative description of mass clouds relative to their center of mass, Richardson defined a so-called distance neighbor function $q(\vec{r}, t)$ that can be seen as a PDF defined for the times t and the distance vectors $\vec{r}$.

The definition of this Lagrangian statistic was also applied in the reverse direction. Instead of asking: "How will the particle pair distance evolve in future", one can also ask: "What is the history of this particle pair?". Concerning the previously named PDF this means to ask: "Given a particle pair at time t with distance $r(t)$, what is the probability that these particles had the distance $r(t - \tau)$ in the past?" Similar to the original definition this concept, called *backward dispersion*, was first developed for the single particle case by Corrsin (1952). In this theoretical study the author uses a combination of Lagrangian and Eulerian approaches to describe the heat transfer in an isotropic turbulence. The two-particle *backward dispersion* was proposed later by Durbin (1980).
Nowadays, a large variety of models for the description of turbulent mixing are based on the *backward dispersion* concept.

As the large number of studies that followed and refined the understanding of turbulent processes on the basis of Lagrangian particle dispersion provides enough material to fill complete textbooks, this section restricts to a short summary of the theory of two-particle dispersion. Additional information on this turbulence measure can be found in (Boffetta et al., 2000; Otte, 2001; Salazar and Collins, 2009).
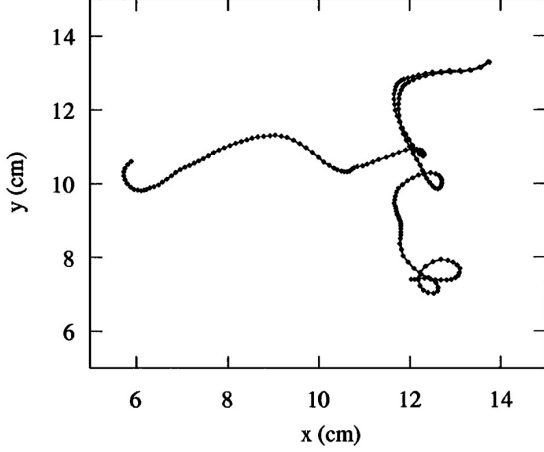
Figure 2.1: Two-dimensional trajectories of a typical particle pair. This picture was taken from a study by Jullien et al. (1999). The initial separation of these particles was 0.3mm and the sampling rate, i.e. the time between two successive dots, is 0.2s.

The underlying kinetic equation that influences the separation vector $\vec{r}(t)$ defining the distance between a given pair of particles can be formulated according to Salazar and Collins (2009) in its integral form.

$$\frac{\mathrm{d}\vec{r}}{\mathrm{d}t} = \vec{w}(t) \tag{2.18}$$

$$\vec{r}(t) = \vec{r}_0 + \int_0^t \vec{w}(t) \tag{2.19}$$

In this integral formulation, $\vec{w}(t)$ is the relative Lagrangian velocity between the two particles, and $\vec{r}_0 = \vec{r}(0)$ is the initial pair separation vector that describes the distance between both particles at the time $t = 0$. Unfortunately the amount of information contained in the functional description of the temporal development of $\vec{r}(t)$ is rather small. Therefore, Lagrangian turbulence statistics use averages computed over a large ensemble of particle pairs. This average growth rate of the particle separation can be defined by

$$\left\langle r^2(t) \right\rangle_L = \langle \vec{r}(t) \cdot \vec{r}(t) \rangle_L . \tag{2.20}$$

This measure has proved to be a valuable parameter for the characterization and for the description of turbulent processes (Salazar and Collins, 2009). The brackets $\langle\ \rangle_L$ indicate an averaging of a large ensemble of Lagrangian particle pairs. This average of such an ensemble containing N elements can be computed using

$$\left\langle r^2(t) \right\rangle_L = \frac{1}{N} \sum_{i=0}^{N} r_i^2(t) \tag{2.21}$$

16

By using (2.18), (2.19) and (2.20), one can formulate a differential equation that describes the dependencies of this turbulence characteristic on the initial separation and the relative velocity vector.

$$
\begin{aligned}
\frac{1}{2}\frac{\mathrm{d}\left\langle r^2\right\rangle_L}{\mathrm{d}t} &= \left\langle \vec{r}(t)\cdot\vec{w}(t)\right\rangle_L \\
&= \left\langle \vec{r}_0\cdot\vec{w}(t)\right\rangle_L + \int_0^t \left\langle \vec{w}(t')\cdot\vec{w}(t)\right\rangle_L \mathrm{d}t'
\end{aligned}
\tag{2.22}
$$

The non linear equation (2.22) depends directly on the relative separation velocity. Therefore, a theoretical modeling of this dependency is rather complex. Most theoretical studies are based on the integral formulation of (2.22)

$$
\frac{1}{2}\left\langle |\vec{r}(t) - \vec{r}_0|^2\right\rangle_L = \int_0^t \int_0^t \left\langle \vec{w}(t')\cdot\vec{w}(t'')\right\rangle_L \mathrm{d}t'\mathrm{d}t''.
\tag{2.23}
$$

The process of dispersion of a tracer particle pair that started with a small initial separation which is much smaller than the Kolmogorov length scale η_{K} can be separated in three different regimes defined by the characteristic scales of the observed turbulence (Salazar and Collins, 2009).

1. The *dissipation subrange*: This regime comprises particle pairs with very small distances, i.e. $r(t) = |\vec{r}(t)| \ll \eta_{\mathrm{K}}$. The Kolmogorov microscale η_{K} is defined in (2.4). In this subrange the relative velocity $w(t)$ can be approximated linearly by a expansion in r.

2. The *inertial subrange*: This subrange lies between the microscale defined by Kolmogorov and the so-called integral length scale L that can be estimated from the size of the large scale eddies occurring in the observed turbulence. Therefore, the inertial subrange is defined as $\eta_{\mathrm{K}} \ll r(t) \ll L$.

3. The *diffusion subrange*: Particle-pair dispersions that are much larger than the integral length scale are contained in this subrange, i.e. $L \ll r(t)$.

In the second subrange, in which the pair separation is of the same order of magnitude as the characteristic length scale of the turbulent eddies, the movement of the eddies becomes the dominant transport mechanism. For the case of a homogeneous and isotropic turbulence, Richardson (1926) proposed a diffusion equation to describe the dispersion within this *inertial subrange*. This PDF was later refined by Obukhov (1941), who determined a description of the diffusion coefficient. As described in detail by Salazar and Collins (2009), this theoretical development yielded a functional description for the mean square displacement that can be modeled by the so-called *Richardson-Obukhov* (R-O) law.
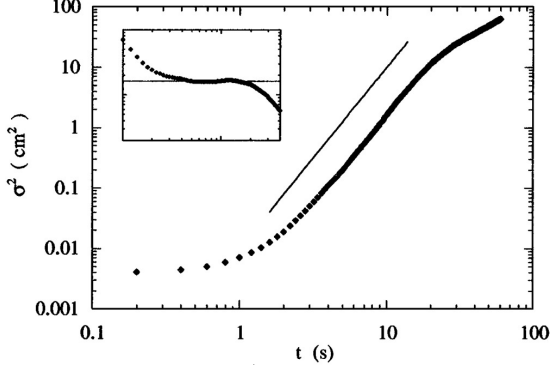
Figure 2.2: Time evolution of the mean squared pair separation. The t^3 dependency in the R-O regime is indicated by a straight line. The subplot shows the same data scaled with t^{-3}. In this visualization the R-O regime causes a plateau. This figure was taken from a study by Jullien et al. (1999).

$$\left\langle r^2(t) \right\rangle_L = g_r \left\langle \epsilon \right\rangle t^3. \tag{2.24}$$

In this equation $\langle \epsilon \rangle$ is the energy dissipation and g_r is a dimensionless constant that can be approximated to be $g_r \approx 0.5$ (Schumacher, 2009).

On the basis of these developments, Batchelor (1950) applied Kolmogorov's K41 theory and formulated a model that describes a solution of (2.23) for short and intermediate observation times (i.e. for $t \ll t_b$ and for $t_b \ll t \ll T_L$). The upper boundary of the intermediate time range is defined by the Lagrangian integral time scale. It has to be pointed out that the following model is only valid if both the initial separation $\vec{r}_0$ and the final separation $\vec{r}(t)$ are within the *inertial subrange*.

$$\frac{1}{2}\frac{\mathrm{d}}{\mathrm{d}t}\left\langle |\vec{r}(t)|^2 \right\rangle_L - \left\langle \vec{r}_0 \cdot \vec{w}(t) \right\rangle_L = \begin{cases} \frac{11}{3}C_2\left(\langle\epsilon\rangle\, r_0\right)^{2/3} t & \text{for } t \ll t_b \\ \frac{3}{2}g\left\langle\epsilon\right\rangle t^2 & \text{for } t_b \ll t \ll T_L \end{cases} \tag{2.25}$$

In this model, C_2 is the second-order Kolmogorov constant for the structure function, and the Batchelor time is defined as

$$t_b \equiv r_0^{2/3} \left\langle \epsilon \right\rangle^{-1/3}. \tag{2.26}$$

In its integral form that corresponds to the expression given in (2.23), the equation given in (2.25) can be written as follows:

$$\left\langle |\vec{r}(t) - \vec{r}_0|^2 \right\rangle_L = \begin{cases} \frac{11}{3}C_2\left(\langle\epsilon\rangle\, r_0\right)^{2/3} t^2 & \text{for } t \ll t_b \\ g\left\langle\epsilon\right\rangle t^3 & \text{for } t_b \ll t \ll T_L \end{cases} \tag{2.27}$$

This differentiation also separates two temporal regimes. The first one is the small scale *Batchelor* regime that explains the pair dispersion of particle pairs in the *inertial subrange* directly after the start of the observation. The second temporal regime

defined by the lower equation is the so-called *Richardson-Obukhov* (R-O) regime. It predicts a t^3 proportionality of the particle pair separation growth for particles in the *inertial subrange* at intermediate times. The transition between these regimes is shown in Figure 2.2. Most publications that describe the particle pair dispersion in the *inertial subrange* and the transition from the *Batchelor* regime to the R-O regime use a t^{-3} scaling of the data. In this representation, which is also shown in the small sub-plot in Figure 2.2 the R-O regime forms a plateau. For times that are much larger than the Lagrangian integral time scale T_L, the particle separation curve in this figure assumes a t^1 proportionality that is caused by normal, large scale diffusion (Boffetta et al., 2000).

2.2 Particle Based Measurement Techniques

The measurement of fluid flow fields by means of small, neutrally buoyant tracer particles that assume the velocity of the fluid has become standard in the field of fluid mechanics. In the last decades various methods were proposed that are based on this technique. Because of the huge diversity of methods in this field it is not possible to give a thorough overview of all these methods within the scope of this thesis. Therefore, this section is restricted to the introduction of methods proposed in the recent past for the measurement of three-dimensional and interfacial flow fields. A more complete introduction to the different methods that exist in the field of particle-based flow field measurement is given in the review papers (Adrian, 1991, 2005).

2.2.1 *Particle Image Velocimetry* (PIV)

In a classical PIV measurement setup, the neutrally buoyant particles are seeded into the fluid and illuminated by means of a planar laser sheet. The light that is reflected from the tracer particles is typically recorded by a *charge-coupled device* (CCD) camera. Typically the optical axis of the camera is perpendicular to the laser sheet. In the evaluation of the recorded PIV image sequences a small correlation window is used to compute a displacement vector field that describes the drift of the recorded particles in consecutively recorded images. In the recent past various extensions to the classical PIV technique were proposed. Most of the extensions were introduced to extend the dimensionality of the measured data, i.e. to measure *three-dimensional three-component* (3D3C) information. Other approaches extended the classical PIV approach to assess interfacial flow information from the boundary layer region of an interface.
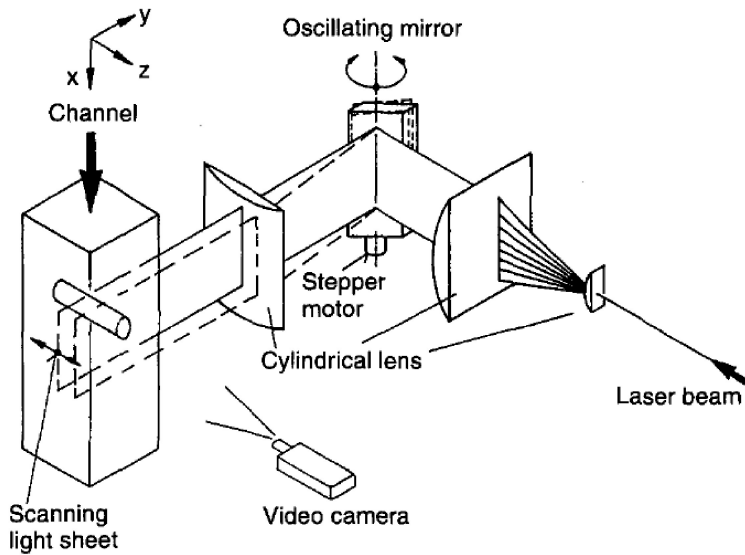
Figure 2.3: Multi-plane scanning system. The laser beam is widened by a first cylindrical lens and then scanned through the measurement volume using an oscillating mirror and a second cylindrical lens. This image was taken from Brücker (1995).

Three-dimensional *Particle Image Velocimetry* (PIV)

The first extensions that aimed for the measurement of the out-of-plane movement in a two-dimensional laser sheet used stereo camera setups with two or three cameras (Arroyo and Greated, 1991; Fouras et al., 2008). These approaches were further extended by (Brücker, 1995; Schröder and Kompenhans, 2004) who used multiple planes that were realized in a scanning light sheet setup as shown in Figure 2.3. In this setup the laser beam is widened to a sheet by a first cylindrical lens and then scanned through the volume of interest by means of an oscillating mirror and a second cylindrical lens. Another method to realize multiple planes is to use color coded light sheets and color sensitive image acquisition devices as proposed by Brücker (1996) and McGregor et al. (2007).

A different strategy commonly used to extract three-dimensional data in PIV measurements is the use of holographic systems. This Holographic PIV technique is described in detail by (Barnhart et al., 1994; Hinsch, 2002). Both the multi-plane approach and the holographic approach allow the extraction of a full volumetric 3D3C flow information and a tracking of individual tracer particles in the so-called *Particle Tracking Velocimetry* (PTV). In contrast to the correlation-based PIV measurement, the results from PTV measurements can be used to extract Lagrangian particle trajectories that describe the movement of infinitesimal fluid volumes in the measured flow field. Unfortunately the data recorded by means of this technique are rather sparse. This is because PTV does not work for high particle seeding densities.

A third common strategy to resolve three-dimensional flow field information uses a tomographic measurement setup. In Tomographic PIV (Elsinga et al., 2006) the full 3D3C flow field can be recorded using multiple cameras. Unfortunately, this method

is connected with a high calibration effort, and the seeding density is constrained by the number of cameras that are used.

Another common technique that can be used to record 3D3C PTV measurements is Defocussing PIV (Grothe and Dabiri, 2008; Pereira et al., 2000; Willert and Gharib, 1992). This technique uses a pinhole mask with a multiplicity of apertures or multiple cameras arranged in a known pattern. This allows to obtain multiple images of the same particle in one measurement. These images form geometrical patterns that scale according to the distance of the individual tracer particle from the focal plane. A Lagrangian particle tracking can be performed on the basis of this information about the depth.

The last extension that allows to measure volumetric 3D3C data using PIV techniques is an absorption based method originally proposed by Debaene (2005) and Kertzscher et al. (2008). They used an absorbing dye to measure the depth from the length of the absorption path of the illuminating light through the fluid.

Interfacial Approaches

As mentioned in Chapter 1 of this thesis, the volumetric measurement of flow fields in the boundary layer of an interface presents a special challenge for particle-based measurement techniques.

A first obstacle is that most common techniques for the measurement of 3D3C data are optimized for a fixed measurement volume that is typically hexahedral shaped. Therefore, a restriction of the measurement volume to a thin layer in the boundary of a possibly non-planar interface presents a major challenge.

Secondly most measurement techniques only work below a certain particle seeding density. Therefore, it is difficult to increase the particle density in the volume of interest to a sufficiently high value because the signals from tracer particles that are not in the interfacial region may interfere with the measurement.

A third challenge is the relation of measured flow vectors with the position of the interface. Since most methods measure in an absolute frame of reference, i.e. not relative to the interface, it is necessary to estimate the exact position of the interface and to align this information with the measured flow fields.

Additionally, all multi-plane methods face another problem. Because of reflections in the interface an adjustment of a scanning unit as shown in Figure 2.3 on page 19 presents a highly complex problem.

According to Berthe et al. (2010), Holographic PIV is a more promising technique for 3D3C measurements in an interface. The only restriction is its bad depth resolution that would especially interfere when it comes to the measurement of moving or non-planar interfaces. Nonetheless, this problem might be solved in the future with the development of better high resolution imaging systems. Another promising approach was published by Turney et al. (2009), who used a stereo camera setup, fluorescent
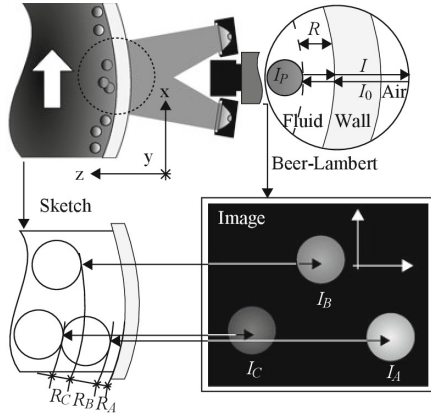
Figure 2.4: Measurement setup used in the "Wall PIV" experiments proposed by Berthe et al. (2010). Particles in the interfacial boundary layer are recorded through the transparent interface. In the fluid the light is absorbed due to a solved dye. Therefore, the intensity of the imaged particles depends on their depth R behind the interface. This figure was taken from (Berthe et al., 2010).

tracer particles and an absorbing dye to restrict the measurement volume to the interfacial region.

The studies by Debaene (2005), Kertzscher et al. (2008), Jehle and Jähne (2008) and Berthe et al. (2010) go one step further. The measurement techniques used in these studies encode the particle depth by means of an absorbing dye. The extraction of the real depth is then simply done on the basis of Beer-Lambert's law for absorption:

$$I = I_0 \exp\left(-\epsilon c R\right) \tag{2.28}$$

In this equation I_0 represents the intensity at the interface, and I is the intensity that is observed in the measurement after the absorption in the dyed fluid. Here c is the dye concentration, ϵ is the absorption coefficient, and R is the distance between the interface and the particle (cf. Figure 2.4).

Since the intensities that can be measured by means of these methods also depend on the reflectance of the particle coating and the particle size, Jehle and Jähne (2008) used two light sources with different wavelengths that are absorbed differently by the dye. From the intensity ratio of the reflected light from both light sources it is possible to eliminate these dependencies as described in detail in Chapter 3 of this thesis.

To estimate the precision that can be reached by using the absorption-based depth estimation, Berthe et al. (2010) made some test measurements. In these measurements a single particle was mounted on the head of a high-precision milling cutter (at the Department of Precision Engineering and Micro Technology (MFG), TU Berlin). The milling cutter allows three-dimensional movements with a precision up to 100 nm in all three directions. Single shot PIV image sequences were recorded by means of a Fastcam Super10K camera and an inversely mounted Nikon Nikkor 50 mm 1:1.8 lens.

Figure 2.5: Temporal integrated PIV benchmark data sets for the validation of the bichromatic wall-PIV method. These pictures were taken from Berthe et al. (2010)
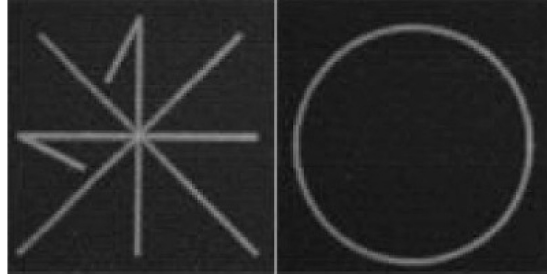
During the measurement the particles were moved with constant velocity on different trajectories (cf. Figure 2.5) near a transparent interface in a dyed liquid. In the present thesis these data sets were used to generate semi-artificial datasets for the validation of the frequency-based velocity estimation as described in Chapter 5.

2.2.2 *Particle Streak Velocimetry* (PSV)

The underlying concept that distinguishes *Particle Streak Velocimetry* (PSV) measurements from the previously introduced methods is that this method uses long exposure times to obtain blurred particle streaks. To the best of my knowledge this method was first introduced by Fage and Townend (1932) in a study to visualize characteristics of turbulent flow fields in circular and rectangular pipes. Afterwards streak photometry was also used to visualize flow characteristics by Prandtl (1957). First measurements to obtain quantitative information from particle streak images were conducted by (Adamczyk and Rimai, 1988; Dickey et al., 1984; Dimotakis et al., 1981). All three studies used computerized evaluation routines to extract the mean direction and the mean velocity by subtracting the end-points of each streak. The study by Wung and Tseng (1992) can be seen as an early precursor of the technique presented in this thesis since this was the first time when temporal information was coded along the streak structures by changing the intensity of the illumination during exposure.

Three-dimensional *Particle Streak Velocimetry* (PSV)

In the recent past many approaches were made to extend the PSV method that was originally developed to measure two velocity components in a plane, i.e. *two-dimensional two-component* (2D2C). Typically, these extensions aim for the measurement of the third velocity component (Müller et al., 2001; Wung and Tseng, 1992) or of volumetric data (Biwole et al., 2009; Dixon et al., 2011; Rosenstiel and Rolf-Rainer Grigat, 2010; Sinha and Kuhlman, 1992). A newly proposed method published in Dixon et al. (2011) even uses a holographic particle streak velocimetry technique to measure volumetric flow features. In this approach blurred holograms are recorded by imaging particles that move during the exposure time. From the radial intensity

profiles of the particles in the hologram the magnitude and direction of the in-plane velocity can be computed.

2.3 Plenoptic Imaging

The inspiration for the development of plenoptic cameras originates from light field-measurement setups using large camera arrays to capture a single scene from different viewpoints.

The recent developments in the field of plenoptic cameras (Georgiev and Lumsdaine, 2010; Lumsdaine and Georgiev, 2009) enable their use for quantitative measurements with a spatial resolution that is sufficient for particle-based flow measurements. These cameras measure four dimensional light fields with a single exposure through a single objective. Compared to a conventional image that only contains information about the intensity of incident light $\mathbf{g} = (g_x, g_y)$ at each pixel, light field-images also comprise information about the angle of incidence

$$\mathbf{l} = (g_x, g_y, \phi_x, \phi_y). \tag{2.29}$$

In this equation (g_x, g_y) is the sensor position of the sampled light field and (ϕ_x, ϕ_y) is the direction of the incident light field.

A single light field image can be used to compute several image features such as:

- a *depth map* of the imaged scene (Bishop and Favaro, 2011)

- projective 2D images with *different focal lengths* (Ng et al., 2005)

- projective 2D images with *different points of view* (Ng et al., 2005)

- *"'all-in-focus"'* images (i.e. full depth of field views) (Perez Nava and Luke, 2009)

The standard geometry of a plenoptic camera uses a micro-lens array that is positioned behind the objective and in front of the CCD sensor. Here the main lens, i.e. the lens of the camera objective, is focused on the micro-lens array, and the lenses of the array are focused at optical infinity (Lumsdaine and Georgiev, 2009). This type of plenoptic camera (hereinafter referred to as *standard plenoptic camera*) has a high angular resolution, but unfortunately the spatial resolution is restricted by the size of the micro-lenses in the array.

In contrast to the standard setup, the *focused plenoptic camera* uses a micro-lens array that is not positioned in the focal plane of the camera objective. Here the micro-lenses are located in a way that they image the focal plane of the main camera lens on the detector. The main advantage of focused plenoptic cameras is the relatively high spatial resolution reached on the expense of a lower angular resolution (Adelson and Wang, 1992).

To describe the general principle of both plenoptic camera types, we make use of a matrix-based formalism for the description of optical transformations that take place in the plenoptic camera. A nice introduction to the used matrix methods is given by Gerrard and Burch (1994).

To simplify the problem, we reduce the four-dimensional light field $\mathbf{l}$ defined in (2.29) to a two-dimensional $g - \phi$ plane. This means, a two-dimensional light field l can be seen as a 2D density function in the ray-space. Basic optical transformations in this space can be described as operations performed on single rays $r = (g, \phi)$ that form the light field.

Translation   A ray from a light field that is transformed in an optical system due to a translation over a certain distance t in the direction of the optical axis can be described by a matrix multiplication (Gerrard and Burch, 1994)

$$(g', \phi') = r \cdot \mathbf{T}_t = (g, \phi) \cdot \begin{pmatrix} 1 & t \\ 0 & 1 \end{pmatrix} = (g + t\phi, \phi). \tag{2.30}$$

This result is not surprising since a translation causes a linear change in the position and no change in the direction of the ray.

Refraction on a Lens   A similar linear dependency can be formulated for the transformation that describes the refraction of a ray on a lens with focal length f. In contrast to the previously described transformation here the spatial coordinate does not change since the refraction at a lens only changes the angular information of the rays in the light field.

$$(g', \phi') = r \cdot \mathbf{L}_f = (g, \phi) \begin{pmatrix} 1 & 0 \\ -\frac{1}{f} & 1 \end{pmatrix} = (g, \phi - \frac{1}{f}g) \tag{2.31}$$

Given these two matrix operations for the description of basic optical transformations, we can formulate a model to describe an optical setup that consists of a lens followed by a free space of length t.

$$r' = \mathbf{TL}r \tag{2.32}$$

A transformation of the complete radiance density function given by a light field $l(r)$ due to an optical setup can be described by the same linear model (assuming non-absorbing transmission through the whole optical system) (Gerrard and Burch, 1994; Lumsdaine and Georgiev, 2009). This allows the formulation of a conservation law for the radiance density function given in the light field $l(r)$.

$$l'(r') = l(r) \tag{2.33}$$

Since the linear transform is allowed in both directions, the transformation of the light field can also be expressed by means of the inverse transformation and the original r.

$$l'(r) = l(\mathbf{A}^{-1}r) \tag{2.34}$$

In the sensor plane of the imaging device, the density function is integrated over all possible ray-directions and reduced to a single gray-value for each sampled position on the sensor.

$$I(g) = \int_\phi l\left(r\left(g,\phi\right)\right)\,\mathrm{d}\phi \tag{2.35}$$

These equations can be used to describe a simplified model of a standard CCD camera that consists of a lens in front of a sensor array that integrates the radiant density function over a given exposure time. The integration over all angles of the incident light field in (2.35) is the reason for the loss of angular information in a standard camera.

2.3.1 The Standard Plenoptic Camera

The basic concept of a traditional plenoptic light field camera (as proposed by Ng et al. (2005)) is shown in Figure 2.6 on page 27. Here a micro-lens array is placed in the focal plane of the main lens in front of the sensor array. The micro-lens array is focused at optical infinity, and the incident light focused by the main lens is therefore decomposed into its angular components by the micro-lenses. As a consequence, the area behind a micro-lens contains the angular information of the light field captured by the corresponding micro-lens in the focal plane.

This explains that the spatial resolution of this plenoptic camera type is restricted by the size of the micro-lenses, whereas the angular resolution depends on the sampling of the area behind the individual micro-lenses.

Focusing on the beam path of a single micro-lens, as shown on the right hand side in Figure 2.6 on page 27, the radiance density in the plane of the lens-array is given by $l(g,\phi)$. Therefore, the radiance density in the sensor plane $l_f(g,\phi)$ array can be described as a transformation of l. This transformation can be expressed by the combination of a refraction due to a lens $\mathbf{L}_f$ (the micro-lens) and a translation $\mathbf{T}_f$ (in the space between lens-array and imaging sensor array).

$$\mathbf{A_f} = \mathbf{T}_f\mathbf{L}_f = \begin{pmatrix} 0 & f \\ -\frac{1}{f} & 1 \end{pmatrix} \tag{2.36}$$

After application of this optical transformation the resulting light field l_f can be computed using (2.34) and (2.36).

$$l_f(r) = l(\mathbf{A}_f^{-1}r) = l(g - f\phi, \frac{1}{f}\phi) \tag{2.37}$$
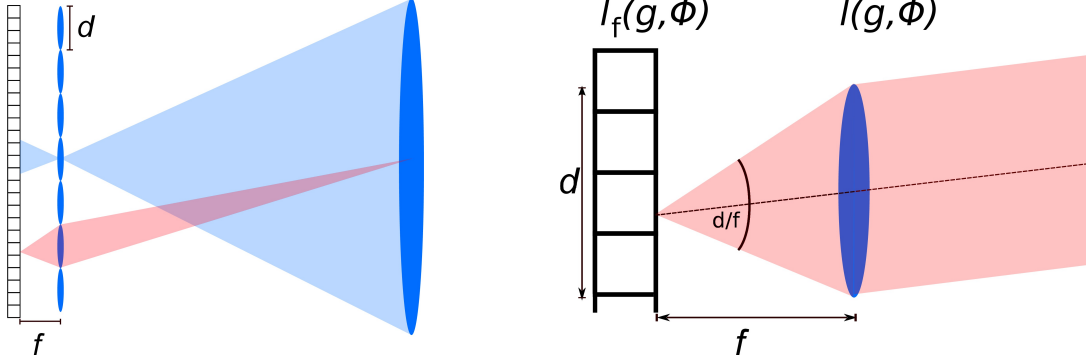
Figure 2.6: Optical beam path of a traditional plenoptic camera. In the *left* image the position of the micro-lens array behind the main lens of the objective is visualized. The array is positioned in the focus of the main lens. Behind the array the light is decomposed into its angular components. The *right* image shows a detailed view on a single micro-lens. The focus position on the sensor array of the camera is determined by the angle of the incident light.

As described by Lumsdaine and Georgiev (2009), the resulting image behind a single micro-lens is given by the integration that is performed in the single pixels of the sensor array.

$$I_f(g) = \int_\phi l_f(g, \phi)\, \mathrm{d}\phi = \int_\phi l\left(g - f\phi, \frac{1}{f}\phi\right)\, \mathrm{d}\phi \tag{2.38}$$

The integration range for the angular integration of l spans an angular area of $\frac{d}{f}$, as shown in the image on the right hand side of Figure 2.6 on page 27. Assuming that the radiance density l is constant over the micro-lens for a given ϕ, the intensity I_f at a point g on the sensor array can be written as

$$I_f(g) = \frac{d}{f} l\left(0, \frac{1}{f}\phi\right). \tag{2.39}$$

This equation shows clearly that the image behind one micro-lens corresponds to a single position $g = 0$ in the plane of the micro-lens array. The spatial position in this micro-lens image encodes the directional distribution of the incident light at $g = 0$.

Therefore, the spatial sampling of this camera type is given by the positions and size of the micro-lenses, whereas the angular sampling is done over a range of $\frac{d}{f}$. This sampling behavior of the standard plenoptic camera is also shown on the left hand side in Figure 2.7 on page 27. In the $g - \phi$ plane the spatial sampling takes place in g-direction. The size d of the red squares indicating single sampling points is restricted by the size of the micro-lenses in the array. In ϕ direction the sampling resolution is restricted by the number of pixels behind a single micro-lens, and the angular range is given by the ratio d/f as shown in Figure 2.6.
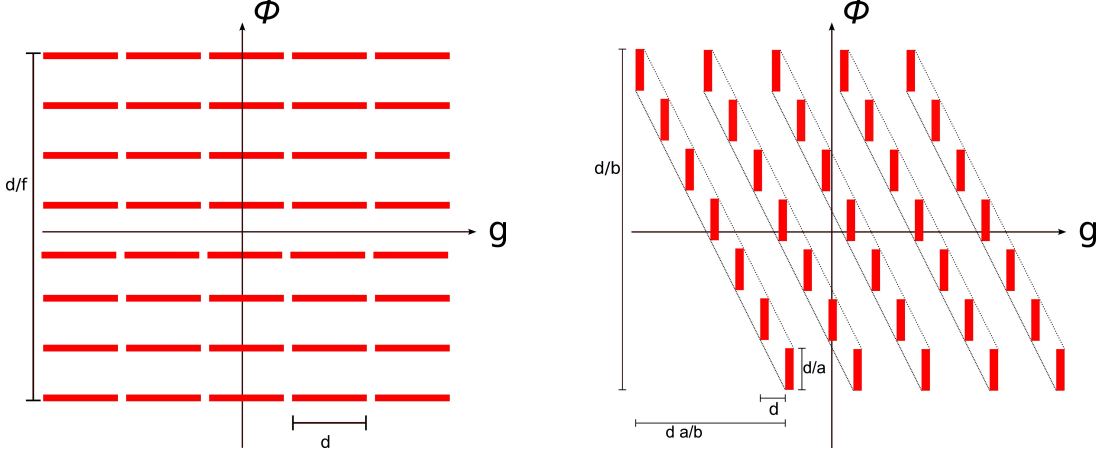
Figure 2.7: Sampling behavior of the traditional and the *focused plenoptic camera. On the left hand side* the sampling of the traditional plenoptic camera is shown. The spatial resolution in g direction is restricted by the size of the lenses in the micro-lens array. The resolution in ϕ direction depends on the number of pixels on the sensor array behind a single micro-lens. The image *on the right hand side* shows the sampling behavior of a *focused plenoptic camera.* Here each diagonal line corresponds to a single micro-lens in the array.

2.3.2 The Focused Plenoptic Camera

A slightly different strategy is used in the *focused plenoptic camera* concept. Here the micro-lens array is also positioned between the main lens of the camera objective and the sensor array, but not in focal plane of the main lens. The following description of the focused plenoptic concept concerns the camera type described by (Perwass, 2011; Wanner et al., 2011), and the mathematical derivation of the optical features and properties was inspired by Lumsdaine and Georgiev (2009).

The optical beam path of this camera model is shown in Figure 2.8. The image on the left hand side shows the position of the micro-lens array behind the focal plane of the main lens. Here the distance between the sensor array and the micro lenses a and the distance to the focal plane b have to fulfill the lens equation

$$\frac{1}{a} + \frac{1}{b} = \frac{1}{f}.\tag{2.40}$$

This optical constellation ensures that the image produced at the focal plane of the main-lens (in a distance b to the micro-lens array) is imaged correctly on the sensor array.

The optical transformation of the radiance at the main focal plane $l_a(g, \phi)$ to the radiance distribution at the sensor array behind the micro-lens array can be described
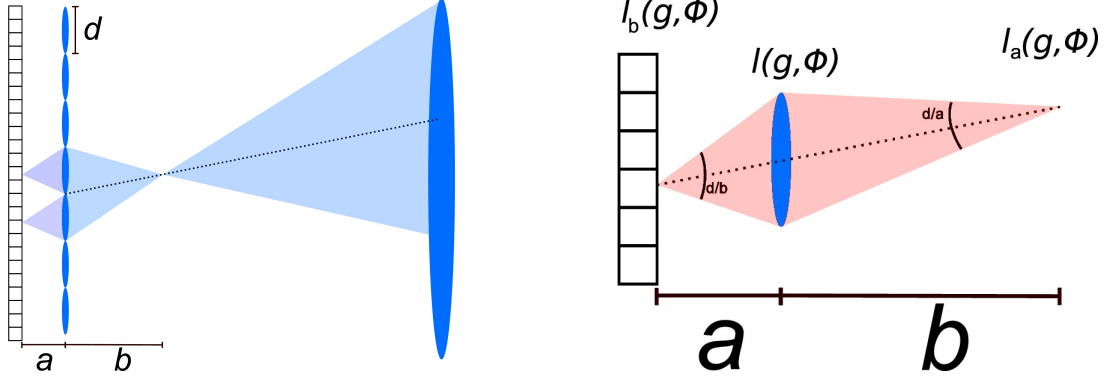
Figure 2.8: Optical beam path of a focused plenoptic camera. *left* The micro lens array is placed between the focal plane of the main-lens of the camera objective and the imaging sensor array. *right* Optical path for a single micro lens.

by the matrix formalism introduced in the previous section.

Therefore, l_b can be computed using (2.34) by

$$l_b(r) = l_a \left(\mathbf{A}_{ba}^{-1} r \right). \tag{2.41}$$

Here the transformation matrix $\mathbf{A}$ is determined by the two translations a and b and the refraction at the micro lenses (focal length f) as follows:

$$\mathbf{A}_{ba} = \mathbf{T}_b \mathbf{L} \mathbf{T}_a = \begin{pmatrix} -\frac{b}{a} & 0 \\ -\frac{1}{f} & -\frac{a}{b} \end{pmatrix}. \tag{2.42}$$

Therefore, the resulting radiance distribution is given by

$$l_b(r) = l_a \left(-\frac{a}{b} g, -\frac{b}{a} \phi - \frac{1}{f} g \right). \tag{2.43}$$

The spatial signal $I_b(g)$ recorded by the sensor array is formed by an integration of the radiance distribution l_b over a range of ϕ given by the fraction d/b.

$$I_b(g) = \int_\phi l_b(g, \phi) \, \mathrm{d}\phi = \int_\phi l_a \left(-\frac{a}{b} g, -\frac{b}{a} \phi - \frac{1}{f} g \right) \mathrm{d}\phi \tag{2.44}$$

As shown in the right image in Figure 2.8 on page 28 only a single value of ϕ in the integral corresponds to the value of $I_b(g)$ for a certain g. As a consequence the integral in Figure 2.44 can be rewritten to

$$I_b(g) = \frac{d}{b} l_a \left(-\frac{a}{b} g, -\frac{1}{b} g \right). \tag{2.45}$$

This simplification which is a central assumption made by Lumsdaine and Georgiev (2009) is only valid if l_a is constant across $\phi = \frac{1}{b}g$.

The micro-lens array in the focused plenoptic camera incorporates a mapping of the radiance in the main focal plane that introduces a scaling of the images by a factor b/a. As a result, objects that have a different distance to the camera and that are therefore focused to a different plane inside the camera are mapped onto the image sensor with a different scaling.

Spatial Resolution   One of the major advantages of the *focused plenoptic camera*, compared to its precursor approach (i.e. the standard plenoptic camera), is the higher spatial resolution of the recorded radiance $l(g, \phi)$ that represents the sampled light field. Lumsdaine and Georgiev (2009) state that this *spatial resolution* is given by the product of the scaling factor $\frac{b}{a}$ and the resolution of the sensor array that was used to acquire $I_b(g)$. The sampling behavior of the focused plenoptic camera is visualized in the right image in Figure 2.7 on page 27. In this visualization each diagonal line corresponds to a single micro-lens. A single pixel on the sensor array samples a single spatial position g and a span $\frac{d}{a}$ in ϕ of the radiance distribution at the main-focal plane $l_a(r)$ at a.

Angular Resolution   This manifestation of the plenoptic camera concept has a much lower angular resolution. This is because the angular domain is sampled by $\frac{a}{b}$ non-overlapping directional samples as shown in the right image of Figure 2.7 on page 27. Therefore, the correlation between the spatial and the angular resolution is exactly anti-proportional.

In contrast to the traditional plenoptic camera, the spatial resolution depends linearly on the resolution of the image sensor and the size of the overlapping regions imaged by the micro-lenses.
The relation between the spatial and the angular resolution of this camera type can simply be adapted by tuning the fraction $\frac{a}{b}$. The only restriction is that a and b have to fulfill the lens equation (2.40).

Spatial Rendering   As mentioned earlier, it is possible to compute different views and "all-in-focus" images as well as depth maps from a single plenoptic light field captured by means of a *focused plenoptic camera*.

In a recent publication Wanner et al. (2011) proposed a simple straightforward approach for the rendering of so-called "all-in-focus" images. This term stands for rendered images that make use of the whole information contained in a light field measurement to compute an image where all objects, even those in different depths, are focused.
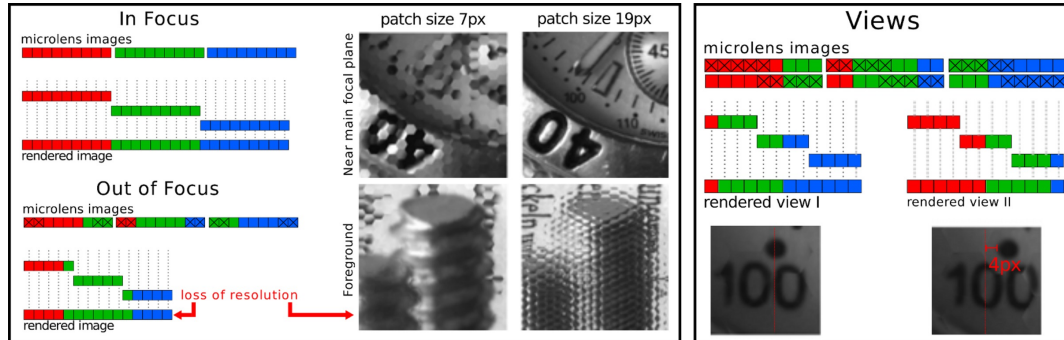
Figure 2.9: Rendering of images from plenoptic light field measurements. *Left:* rendering of different focal positions from the same light field measurement by combining image patches with different sizes; *Right:* rendering of different view-points from a single light field measurement by shifting the patches that were cut from the light field image. This figure was published by (Wanner et al., 2011).

The $\frac{b}{a}$ scaling introduced by the mapping of the main-focal plane onto the image sensor due to the micro-lenses encodes a depth-information in the recorded light field as shown in Figure 2.9. An object that is not in the focus plane of the main-lens will be mapped by the main-lens to a different focal plane in front of the micro-lens array. The consequence of this different distance to the array is a different scaling factor $\frac{\breve{b}}{\breve{a}}$. Therefore, the size of the object in the micro-lens patch on the image sensor array will be smaller than the size of an "in-focus" object.

This knowledge can be used to compute different focal-plane representations from a single light field image by cutting and arranging lens-patches of different sizes. As shown in the right image of Figure 2.9, an "out-of-focus" plane can be moved into focus by cutting out a smaller center area of the single micro-lens images and rearranging these patches. It can also be seen in this image that the resolution decreases when focusing on focal-planes that are further away from the main-focal plane.

For the computation of these "all-in-focus" images, Wanner et al. (2011) render a set of images based on different micro-lens patch sizes. Each image in this set corresponds to a different focal plane in the measurement. By minimizing a cost function that is based on the perpendicular gray-value gradients at the boundaries of the micro-lens patches, the correct focal-depth for all micro-lens patches in the image is estimated locally. This focus-map determines the size of the focus-patches that are cut from the micro-lens images as shown in Figure 2.9. In a next step these patches are magnified in order to obtain equi-sized patches. In the last step an "all in focus" image is built by arranging these patches to a new image.
The focus-map can also be seen as a depth map since the local position of the focal plane can be used in a "depth-from-focus" like approach to obtain depth information

of the recorded scene.

Variation of the Viewpoint The viewpoint on the recorded scene can also be varied within the sampled range of ϕ. In the recorded data from the *focused plenoptic camera*, this change of the viewpoint can be achieved by moving the center of the micro-lens patches before cutting them to set the correct focal plane. This concept is shown in the right image of Figure 2.9.

To render *view I* the center of the micro-lens patches is moved to the right, and for the computation of the second viewpoint *view II* the image patches are taken from the very left part of the micro-lens images. The result is a shifted viewpoint as shown in the lower part of the right image in this figure.

In a different depth estimation approach these viewpoints that are contained in the light field images are used to compute a depth-map from the recorded data by means of a simple stereo approach (Jähne, 2005).

3 Measurement Technique

This chapter comprises a detailed description of the particle-based measurement techniques that were purpose-built for measurements of volumetric *three-dimensional three-component* (3D3C) flow information within the boundary layer of an interface.

The presented methods are hybrid approaches which use a combination of existing methods and extensions to these methods. The main ideas and strategies that built the underlying concept of these methods will be explained as well as the technical realization.

The first section (Section 3.1) of this chapter introduces the basic principle of the *Particle Streak Velocimetry* (PSV)-method. This flow field measurement method uses long exposure times to record the trajectories of tracer particles in a fluid. All particles that are illuminated during this time reflect light on the imaging device and are thus imaged as streak structures in the recorded images.

An important and novel extension that was made in this study is the introduction of an intensity modulated light source. The purpose of this special illumination was to code temporal information in the images. As shown later, it is possible to decode the velocity course of single particles during one exposure by means of a frequency analysis of the spatial periodical intensity signal along the corresponding streak structures.

The second section (Section 3.2) focuses on the extraction of volumetric *three-dimensional* (3d) data. Here a two-wavelength illumination and an absorbing dye were used. The different absorption characteristic of the dye for both wavelengths allows an extraction of the particle depth from the reflected intensities. In contrast to other absorption-based depth extraction approaches, the usage of a second wavelength introduces a higher robustness and precision of the depth estimate. Furthermore, the measured depth-information is already in a reference frame that is relative to the interface. In contrast to all other published methods that were invented for extraction of interfacial flow information the absorption-based depth extraction technique is able to extract Lagrangian flow information relative to the interface without using an additional interface-tracking setup. The basic principles of this method, called *bichromatic Particle Streak Velocimetry* (bPSV), were already presented to the scientific community in (Voss and Garbe, 2010; Voss et al., 2010).

Section 3.3 describes the concept of an alternative single camera depth-extraction approach. It uses a special imaging device called *focused plenoptic camera* that samples a four-dimensional light field. By extending the developed PSV measurement approach

with this new imaging hardware, this thesis proposes a second strategy for the measurement of volumetric 3D3C flow information by means of a single camera.

As described in detail in this chapter, four-dimensional light fields were measured in long-time exposure images containing all information that is needed to reconstruct the velocity and the trajectories of the tracer particles within the volume of interest.

Unfortunately the depth information of the particle trajectories can only be measured in an absolute frame of reference. Therefore, the application of this technique for the measurement of interfacial flow fields becomes difficult. Nonetheless, the combination of the proposed PSV approach with a plenoptic imaging device presents an adequate alternative to state-of-the-art *Particle Streak Tracking* (PST) methods.

The following section (Section 3.4) describes the merging of multiple particle streaks from subsequent images of a PSV image-sequence to long trajectories. This allows the tracking of single tracer particles through multiple images, i.e. over a long period of time. Basically this can be achieved by a matching routine that finds streaks in subsequent images which belong to the same tracer particle. As described in this section, the matching is realized by means of an adaptive Mahalanobis distance metric. The merging of trajectories that contain streaks from multiple subsequent images from a PSV measurement is solved using cubic spline-fit routines based on a least-squares regression.

The last section (Section 3.5) explains the statistical measure that was used to characterize the turbulent flow fields measured within the scope of this thesis. It is based on the particle acceleration and on the dispersion rate of particle pairs.

3.1 *Particle Streak Velocimetry* (PSV)

For the particle-based measurement of Lagrangian flow information close to a present interface a PSV approach was chosen. In standard PSV measurements, tracer particle images are recorded in long exposure measurement with constant illumination. As described in the previous chapter, most of these techniques use laser sheet illuminations. The consequence is a two-dimensional restriction of the measurement volume and the components of the extracted velocity vectors. Additionally, all previous published PSV-approaches such as (Adamczyk and Rimai, 1988; Dickey et al., 1984; Dimotakis et al., 1981) suffer from the long exposure times that yield a bad temporal resolution. Even newest approaches such as (Dixon et al., 2011; Rosenstiel and Rolf-Rainer Grigat, 2010) only provide averaged information about velocity of the tracer particles during the exposure time. This restriction is caused by the long exposure. It can be seen as a temporal integration that causes a loss of temporal information.

Bichromatic Measurements   To overcome all these restrictions, we combined the classical PSV approach, summarized in Section 2.2.2, with a bichromatic depth extraction

routine. This routine is based on a volumetric two-wavelength illumination and an absorbing dye. Additionally, an intensity modulated illumination was used to gain the temporal resolution of the extracted velocity information. The main advantages of this measurement technique are the following:

- It is a low cost solution for volumetric 3D3C flow field measurements since only a single gray-value camera, an absorbing dye, reflecting tracer particles and a *light-emitting diode* (LED) illumination are needed.

- Because only one camera is used (imaging the interface from above), the calibration is much simpler compared to alternative systems such as holographic methods or stereo-based approaches.

- It is a perfect solution for interfacial measurements since the measured data are already in a reference frame that is relative to the interface. This makes an additional interface-tracking routine dispensable.

Plenoptic Measurements A second technique for the volumetric measurement of 3D3C PSV data was tested within the scope of this thesis. Here a single *focused plenoptic camera* (Lumsdaine and Georgiev, 2009) was used for the depth estimation. Similar to the bichromatic PSV experiments, the exposure time of this camera was set to high values, to realize a temporal integration that results in particle streaks (shown in Figure 3.2 on page 41). The light source, used in these experiments, was also intensity modulated with a sine function to enable the extraction of an instantaneous velocity, using a frequency analysis. For the particle streak extraction routine the light fields that were recorded by means of the *focused plenoptic camera* were processed to render "all-in-focus" images. In these images all objects, even those in different depths, are displayed "in-focus" to allow the extraction of particle streaks from all focal planes within the measurement volume. Additionally, the particle depth information was extracted from depth-maps that were also rendered using the information contained in the recorded light fields.

Calibration A proper radiometric and geometric calibration of the whole setup including the imaging devices and the illumination is a basic condition to measure precise volumetric 3D3C flow information using the *bichromatic Particle Streak Velocimetry* (bPSV)-technique or the *plenoptic Particle Streak Velocimetry* (pPSV)-technique. Especially the camera used for the bichromatic depth estimation requires a sound radiometric calibration since the quality of the depth estimate depends crucially on the precision of the measured absolute gray-values. Therefore, the gray-value camera that is used for the bPSV measurements was characterized according to the *European Machine Vision Association* (EMVA)-1288 standard (EMVA, 2010) to determine the radiometric camera properties. A detailed description of the calibration and its results is given in Section 5.1 of this thesis.

The geometric calibration is rather simple since only a single camera with an optical axis perpendicular to the interface is used. To determine the pixel-size and the concomitant magnification, a mm-Grid (shown in Figure 3.6 on page 53) was placed in the air-water interface and in a depth of 10mm below the interface.
In all measurements that were recorded during this project the perspective distortion, caused by the larger distances within the volume of interest, was found to be significantly smaller than the error observed in the spatial calibration of the pixel size. A detailed description of the precision of the measurement systems is given in Chapter 5

For the extraction of meaningful depth information from the depth-maps that were extracted from the light field measurements, recorded by means of the plenoptic camera, a seven point calibration was conducted previous to each measurement. In this calibration a random-noise pattern (shown in Figure 3.6 on page 53) was placed in different depths within the measurement volume. For each depth, a depth-map was computed from the recorded light field using the evaluation software *RXLive* provided by the camera-manufacturer (Perwass, 2011). This depth-map computation is based on the principles explained in Section 2.3. Afterwards a linear regression was used to compute a scaling factor that allows the conversion from the integer values of the depth-map to real depth values. The resulting depth values are all given relative to the focal plane of the main lens. ([DN] $\Rightarrow$ [mm]).

Particle Kinematics   In the planing and analysis of every particle-based flow measurement the question arises whether the particle movement complies properly with the movement of the surrounding fluid. A common way to quantify this compliance analytically is based on the argument of Stokes for a low Reynolds number flow around a sphere (Dring, 1982; Grant, 1997; Tropea et al., 2007).
The following derivation is valid for a slow motion of a viscous fluid around a sphere. In his well known *Stokes equation* for the drag of a sphere George Gabriel Stokes (1819–1903) described the drag of a sphere with diameter d_p that is surrounded by a parallel fluid stream as follows:

$$D = 3\pi\nu d_p U \tag{3.1}$$

In this equation U represents the relative fluid velocity of the stream with respect to this sphere and ν is the viscosity of the fluid.
The amount of total drag can be split into two parts. One fraction caused by the difference in the pressure distribution around the sphere and a second fraction due to frictional forces. It can be shown that the fraction caused by a pressure imbalance contributes with one third to the total drag. The remaining two thirds originate from the friction caused drag (Biswas, 2003). Therefore the drag coefficient can be defined to be

$$C_D = \frac{D}{0.5\rho U^2 A}, \tag{3.2}$$

where A is given by the frontal area of the sphere ($A = 0.25 \cdot \pi d_p^2$).

More precisely, the equation of motion for a small particle moving in a viscous environment can be formulated, according to Tropea et al. (2007), as follows:

$$\frac{\pi d_p^3}{6}\rho_p \dot{v} \;=\; \underbrace{\frac{\pi d_p^3 \rho_f}{6}\frac{\mathrm{D}\mathbf{V}}{\mathrm{D}t}}_{\text{non-inertial force}} + \underbrace{\frac{\pi d_p^3\left(\rho_p - \rho_f\right)}{6}g}_{\text{net body force}} \tag{3.3}$$

$$\underbrace{-\,3\pi\nu d_p\left((v-U) - \frac{1}{18}d_p^2\nabla^2 U\right)}_{\text{quasi-steady viscous force}} \tag{3.4}$$

$$\underbrace{-\,\frac{3}{2}\pi\nu d_p^2\int_0^\infty \frac{\mathrm{d}}{\mathrm{d}\tau}\left((v-U) - \frac{1}{18}d_p^2\nabla^2 U\right)\frac{\mathrm{d}\tau}{\sqrt{\nu\left(t-\tau\right)}}}_{\text{time history (Bassed) force}} \tag{3.5}$$

$$\underbrace{-\,\frac{1}{12}\pi d_p^3\frac{\mathrm{d}}{\mathrm{d}t}\left((v-U) - \frac{1}{40}d_p^2\nabla^2 U\right)}_{\text{added mass force}} + \underbrace{\mathbf{L}}_{\text{lift force}} \tag{3.6}$$

In this equation ρ_p and ρ_f are the densities of the particle and of the fluid respectively. The variable g determines the gravitational acceleration.
Rotating particles or particles that move within a rotational flow field such as a shear layer are subject to the so-called "lift force" $\mathbf{L}$.

When it comes to small tracer particles, the right-hand term of the equation of motion is dominated by the Stokes drag, which is described by the "quasi-steady viscous term". To compute the *slip-velocity* ΔU that is given by the difference between the fluid velocity U and the velocity of the tracer particles v, the time derivatives can be approximated as follows:

$$\frac{\mathrm{D}U}{\mathrm{D}t} \approx \frac{\mathrm{d}v}{\mathrm{d}t}. \tag{3.7}$$

Therefore the *slip-velocity* is given by

$$\Rightarrow \Delta U = U - v \approx \frac{d_p^2\left(\rho_p - \rho_f\right)}{18\nu}\frac{\mathrm{d}v}{\mathrm{d}t}. \tag{3.8}$$

The acceleration of the particle is given by the temporal derivative of its velocity v.
As described for example by Grant (1997), these equations can be used to estimate the ability of tracer particles to follow spatial or temporal gradients within the fluid-flow.

For a characterization of this particle property, the differential equation in (3.8) can be solved to

$$v = U \left(1 - \exp\left(\frac{-t}{\tau} \right) \right).$$ (3.9)

The characteristic response time τ that describes how fast the particles assume the local flow velocity U is therefore given by

$$\tau = \frac{(\rho_p - \rho_f)\, d_p^2}{18\nu}$$ (3.10)

In all experiments that were conducted during this study, neutrally buoyant particles were used that fulfill the following requirement

$$\frac{\rho_p - \rho_f}{\rho_f} \approx 0.$$ (3.11)

The error that is introduced by particles that do not exactly follow the fluid movement can therefore be eliminated by choosing adequate tracer particles. This becomes a problem when measuring in a gaseous environment, were the density ratio of available particles is typically of the order $\frac{\rho_p}{\rho_f} = \mathcal{O}(10^2)$ (Tropea et al., 2007). Since we aim to develop a measurement method for the water-sided boundary layer, this is easily achievable since neutrally buoyant tracer particles for *Particle Image Velocimetry* (PIV) measurements in fluids are commercially available in various sizes between $1\,\mu$m and $100\,\mu$m and for different fluid densities with low density variations.

Scattering Properties   The size of the tracer-particles is restricted according to two requirements. On the one hand, the tracer particles have to be sufficiently large to scatter enough light. Small particles below a certain size do not reflect enough light to measure their signal on the imaging device. On the other hand, the particles should be much smaller than the smallest expected flow structure. Particles with sizes that are in the order of magnitude of the characteristic size of the flow field only provide averaged flow information.

For a better understanding of the reflectance properties of tracer particles, an understanding of the underlying scattering mechanism is inevitable.
A common strategy to identify the dominant scattering mechanism of the interaction between electro-magnetic waves of a certain wavelength λ and particles of a certain diameter d is the classification by means of the dimensionless *Mie parameter* (Raffel et al., 1998)

$$\alpha_{mie} = \frac{\pi d}{\lambda}$$ (3.12)

By using this parameter that describes the ratio between the circumference of a tracer particle and the wavelength of the electro-magnetic radiation, a dominant scattering mechanism is determined by the following differentiation.

$\alpha_{mie} \ll 1$**:** If the tracer particle is much smaller than the wavelength of the illumination, the dominant scattering mechanism can be described by the Rayleigh scattering theory. Here the polarization of light that is scattered in an angle of $90°$ is perpendicular to the incident light. The forward and backward scattered light contains both directions.

$\alpha_{mie} \approx 1$**:** If both the size of the tracer particle and the wavelength of the illumination, are within the same order of magnitude, the scattering is described best by the Mie theory. A detailed description of the Mie theory and its consequences is given in (Raffel et al., 1998) and (Tropea et al., 2007).

$\alpha_{mie} \gg 1$**:** For particles that are much larger than the wavelength of the illumination, the scattering is described best by means of the geometric scattering theory. In this theoretical description light waves are abstracted as light rays. These rays can be transformed in the following by Snell's law and Fresnel's formulas to describe reflection and refraction processes.

The tracer particles that were used within the scope of this study clearly belong to the third category. Therefore, the scattering behavior can be described by the geometric scattering theory. As a consequence, cross-section of a tracer-particle is of the same order of magnitude as its cross-sectional area (Jeys et al., 2007).

3.1.1 Particle Streak Model

The main idea of *Particle Streak Tracking* (PST) or *Particle Streak Velocimetry* (PSV) techniques is that tracer particles are imaged over a certain, long exposure time t_{exp}, instead of imaging the tracer in single shot recordings with a very short integration time. The intensity distribution on the *charge-coupled device* (CCD)-array at a certain point in time $I(\vec{x})$ can be described by the well known *Airy-Function*, which in polar coordinates (ρ, φ) is given by

$$I(\rho, \varphi) = \left(\frac{2J_1(ka\rho)}{ka\rho}\right)^2 I_0. \tag{3.13}$$

Here J_1 is the first order *Bessel Function*, $k = \frac{2\pi}{\lambda}$ is the wavenumber and a controls the radius. As shown in Figure 3.1 on page 40 this function can be approximated by a Gaussian bell-curve as follows (Leue et al., 1996). The logarithm of the *Airy-Function* can be decomposed in a second order Taylor expansion
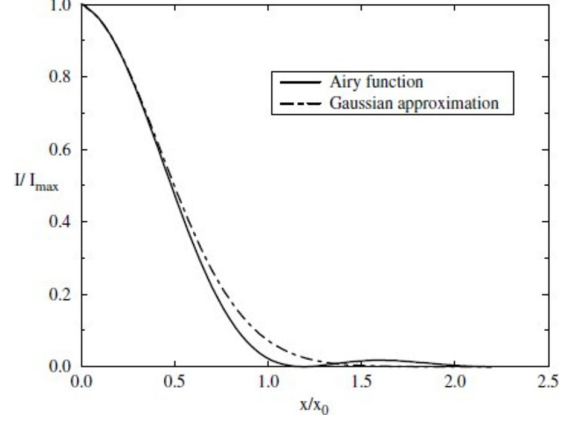
Figure 3.1: Intensity distribution of the Airy function and its approximation by a Gaussian bell-curve (Raffel et al., 1998).

$$\ln\left(I\left(\rho, \varphi\right)\right) = \ln\left(I_0\right) - \left(\frac{ka\rho}{2}\right)^2 + \mathcal{O}\left(\rho^4\right). \tag{3.14}$$

By replacing $\sigma = \frac{\sqrt{2}}{ka}$, the first and second order terms can be rewritten to a Gaussian bell-curve in polar coordinates.

$$I\left(\rho, \varphi\right) \approx I_0 \exp\left(-\frac{1}{2}\left(\frac{\rho}{\sigma}\right)^2\right) \tag{3.15}$$

The gray-value distribution $g(\vec{x})$ on the CCD-Chip, caused by the intensity distribution of a particle that travels along a trajectory $\vec{X}(t)$, $t \in (0, t_{exp})$ during the exposure time t_{exp}, can therefore be modeled by a simple time integral

$$g\left(\vec{x}\right) = \frac{1}{t_{exp} - t_0} \int_{t_0}^{t_{exp}} G_\sigma\left(\vec{x} - \vec{X}\left(t\right)\right) dt. \tag{3.16}$$

In this model, $G\left(\cdot\right)$ is a two-dimensional Gaussian distribution. For a set of N tracer particles with trajectories $\vec{X}_l(t)$, $t \in (0, t_{exp})$ with $l = 0, \ldots, N - 1$, the gray-value distribution in a PSV-image is given by the sum over all trajectories.

$$g_N\left(\vec{x}\right) = \frac{1}{t_{exp} - t_0} \sum_{l=0}^{N-1} \int_{t_0}^{t_{exp}} G_\sigma\left(\vec{x} - \vec{X}_l\left(t\right)\right) dt \tag{3.17}$$

The resulting images contain information of the particle trajectories because the paths of all particles are mapped as streak-structures on the image plane.

For the extraction of these particle streaks an extraction routine was developed that is based on this model. As described in detail in Section 5.2, it computes the sub-pixel precise position of the center-line, the width and the intensity course of the recorded streak-patterns.
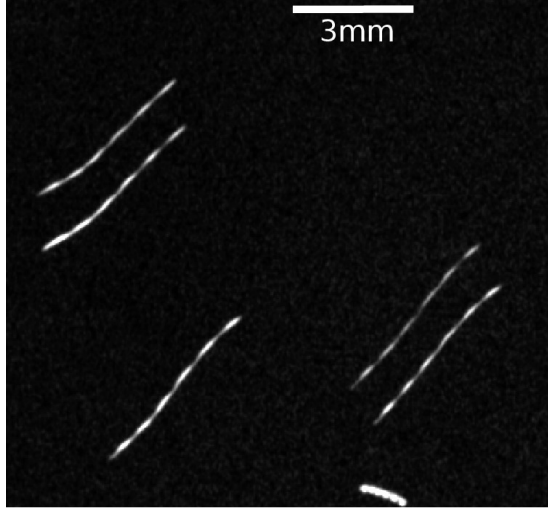
Figure 3.2: PSV image recorded using an intensity modulated light source. The exposure time in this measurement was set to $t_{exp} = 1\,\text{s}$, and the frequency of the intensity modulation function was set to $F = 6\,\text{Hz}$. In this measurement silver coated hollow ceramic spheres with $100\,\mu\text{m}$ diameter were used.

3.1.2 Periodical Intensity Modulation

The main idea of this novel approach is to use a periodic illumination to code the course of the particle velocity in the long-exposure image. It can then be recovered by means of a frequency analysis that is applied on the spatial gray-value signal, along the center-line of the streak-structures. The strategy is similar to the one used for the speed measurements based on the Doppler effect. The velocity estimation strategy is based on the observation that a slow particle illuminated with an intensity modulated light source results in a short streak with a higher spatial frequency, compared to the streak of a faster particle that results in a long streak with a lower spatial frequency.

In this work an intensity modulated illumination was used to overcome the loss of temporal information due to the integration in (3.16). As already published in (Voss and Garbe, 2010; Voss et al., 2010), the reflected signal of a periodical modulated light source on the streak structures can be used to compute the horizontal velocity of the particles from the ratio of the constant illumination frequency $F[\text{Hz}]$ and the spatial frequency along the recorded streak $f(c)[1/\text{px}]$.

$$v_h(c) = \alpha \frac{F}{f(c)} \tag{3.18}$$

In this equation $\alpha[\text{mm}/\text{px}]$ is the pixel size. It is used to convert the velocity unit from $[\text{px}/\text{s}]$ to $[\text{mm}/\text{s}]$.
This scaling parameter has to be determined previous to each measurement in a calibration measurement as described in the previous section.

In terms of the derived PSV-model, the introduction of an intensity modulation in the illumination of the experiment can be expressed by a sine function, multiplied to the

integral in (3.17).

$$g_N\left(\vec{x}\right) = \frac{1}{t_{exp} - t_0} \sum_{l=0}^{N-1} \int_{t_0}^{t_{exp}} \left(1.5 - \sin\left(2\pi F t\right)\right) G_\sigma\left(\vec{x} - \vec{X}_l\left(t\right)\right) dt \qquad (3.19)$$

The modulation frequency F of the illumination and the exposure times t_{exp} used in the experiment have to be chosen according to the expected velocities in the observed flow field. As a result of calibration measurements with various frequencies, exposure times and velocities, two rules for the parametrization of frequency and exposure time can be formulated.

1. The number of periods Ft_{exp} should be larger than 5 to assure a correct extraction of the instantaneous frequency. Thus follows

$$\Rightarrow F \geq \frac{5}{t_{exp}}. \qquad (3.20)$$

2. In order to image nice streak structures, the exposure time should be long enough, so that streaks caused by slow particles are long enough to enable a proper feature extraction. It was found empirically that the product of the horizontal particle velocity v_{px} [px/s] and exposure time t_{exp} [s] should be at least 50[px], leading to

$$\Rightarrow t_{exp} \leq \frac{50}{v_{px}}. \qquad (3.21)$$

Figure 3.2 on page 41 shows a real measurement obtained in one of the turbulent *Rayleigh-Bénard* (RB)-convection experiments that were conducted during this study. The exposure time in this case was $t_{exp} = 1\,\mathrm{s}$, and the intensity modulation frequency was set to a value of $F = 6\,\mathrm{Hz}$. A detailed description of the experimental setup that was used to record these image is given in Chapter 4.

3.1.3 Velocity Estimation

For the velocity estimation, a frequency analysis method with a high resolution in the frequency domain and in the spatial domain is needed.

The simplest way to extract the frequency of a one-dimensional signal is to apply a *Discrete Fourier Transform* (DFT). By inspecting the signal in the Fourier domain, one can easily determine its dominant frequency. This dominant frequency is a feature that characterizes the whole signal. Therefore, it could be used to compute an average particle velocity. For a detailed extraction of the particle velocity at each position along the streak, it is desirable to extract the frequency with a high precision in both frequency domain and time domain. Due to Heisenberg's Uncertainty principle, a precise

measurement of frequency and position has a natural limit. The result of the Fourier Transform has a maximal precision in the frequency domain, but unfortunately no precision at all in the spatial domain. This means, a local change of the signal at a single position in space will change the corresponding signal in the *Fourier Domain* globally. In the field of signal processing, many promising attempts to extract signal frequencies with the highest possible precision in frequency and temporal domain were made. The most promising approaches are the *Windowed Fourier Transform* (sometimes also called *short time Fourier Transform* (STFT) (Gabor, 1946) that uses a normalized, real valued and symmetric window function to restrict the frequency information from the Fourier Transformation to a local area, the *Hilbert Huang Transform* (HHT) which can be used to extract an *instantaneous frequency* and a *instantaneous amplitude* of the input signal (Huang et al., 1999, 1998; Smith, 2007) and the *Wigner-Ville Transform* that can be seen as a method for measuring the local time-frequency energy (Martin and Flandrin, 1985). In order to obtain an *instantaneous frequency* information that enables the extraction of the particle velocity at every point on the streak, we perform a HHT on the gray-value signals that were extracted along the center-lines of the streaks. The HHT is a combination of an *Empirical-Mode-Decomposition* (EMD) and a signal processing transformation called *Hilbert Transform* (HT). Additionally, we make use of the extracted *instantaneous amplitude* signal since it contains information on the particle depth.

The velocity estimation routine can be divided into three main tasks that also determine the structure of the extraction algorithm.

- The adjustment of the periodical gray-value signal. In this signal processing step a non-periodical offset is subtracted that was previously computed using an *Empirical-Mode-Decomposition* (EMD).

- The computation of instantaneous signal properties, i.e. the *instantaneous frequency* $f(c)$ and the instantaneous amplitude $a(c)$ for each point c on the center-line by means of a HT.

- The velocity estimation using (3.18), the instantaneous frequency $f(c)$, the illumination frequency F and the pixel size α.

The following two subsections describe methods that were developed in the field of time series analysis. Therefore all given references will describe the EMD and the HT for time-dependent signals. For the purpose of this study, the frequency analysis has to be performed on spatial signals. Therefore all definitions were changed to describe spatial signals that are dependent on the position on the center-line c. As a result, all computed frequencies are given in units of [$1/\text{px}$] instead of [$1/\text{s}$].
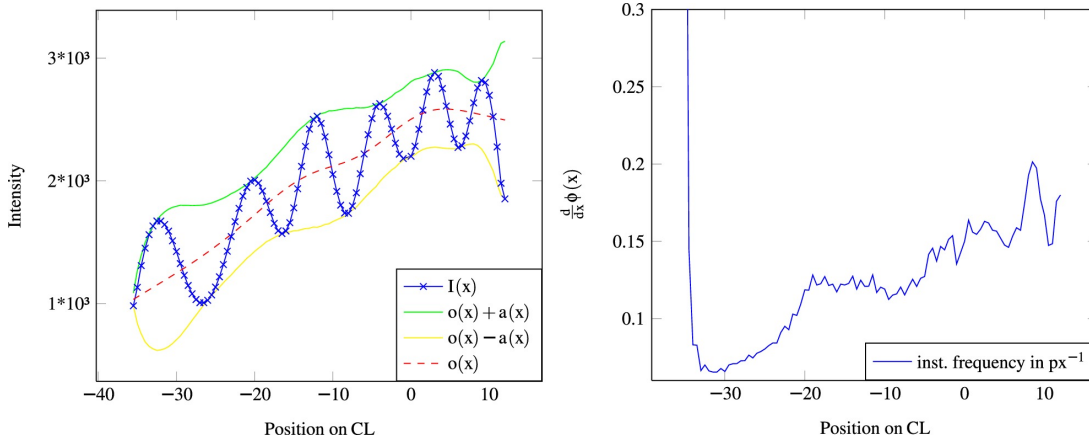
Figure 3.3: Frequency analysis of a gray-value signal from a single streak in a bPSV measurement. **Left:** Result of the *Empirical-Mode-Decomposition* (EMD). The measured gray-value signal (blue) is decomposed in a periodic signal (not shown) and a non-periodical offset (dashed red line). The sum and the difference of the *instantaneous amplitude* and the offset form an envelope of the signal (yellow and green). **Right:** Instantaneous frequency of the signal shown in the upper plot computed by means of the *Hilbert Huang Transform* (HHT).

Empirical-Mode-Decomposition (EMD)

In order to separate the periodic content of the gray-value signal from the non-periodical offset and from high frequent noise, an EMD was used. This method was first introduced by Huang et al. (1996) and is based on the assumption that every signal consists of different intrinsic modes of oscillations which comprises the same number of extrema and zero-crossings. Furthermore, it assumes that each oscillatory mode is symmetric with respect to a local mean.

This local mean is given by the mean of two envelope functions defined by a spline fit through the local maxima and a spline fit through the local minima of the oscillatory mode.

In a later publication, Huang et al. (1999) describe two conditions that have to be fulfilled by a valid *intrinsic mode function* (IMF) to obtain meaningful results in the frequency analysis.

1. The difference between the number of extrema and the number of zero-crossings that are contained in a valid IMF must be less or equal one.

2. At any point on a valid IMF the local mean value defined by the mean of the two envelope functions is zero.

The first condition can be seen as a restriction of the IMFs that avoids higher frequent riding waves. The second restriction is necessary to avoid unwanted fluctuations that

may be introduced by asymmetric wave-forms. These fluctuations would yield large errors in the *instantaneous frequency* that is computed from the dominant IMF of the signal.

***Empirical-Mode-Decomposition* (EMD)**   The strategy of the EMD is to extract a set of IMFs that are contained in a signal by applying a sequence of iterative repeated siftings. A detailed description of the algorithm is given in Chapter 5 of this thesis. Its pseudo-code can be found on page 96.

The result is a decomposition of the original signal $X(c)$

$$X(c) = \sum_{j=1}^{n} c_j + r_n \tag{3.22}$$

that consists of a set of n IMFs c_i, $(i \in \mathbb{N} | 0 < i \leq n - 1)$ and a non-periodical rest r_n.

The gray value signals that were extracted along the center-lines of the particle streak-structures typically consist of three modes:

1. The first one is a high frequent IMF that contains noise that was induced by pixel-wise differences of the CCD-sensor and by numerical artifacts in the *Levenberg-Marquardt* (LM) fit used in the center-line extraction algorithm (cf. Chapter 5).

2. The second IMF holds the dominant mode that is determined by the particle speed and the frequency of the intensity modulation function.

3. The last mode comprises the non-periodical offset r_n.

In the following frequency analysis by means of a HT, only the IMF that contains the dominant mode is considered. From now on this one-dimensional, spatial signal will be labeled as $X(c)$.

Frequency Analysis using the *Hilbert Transform* (HT)

The frequency analysis of the periodical gray-value intensity course $X(c)$, obtained from each streak-structure, is based on the computation of the corresponding *analytical signal* $Z(c)$. In this context the variable c describes the position on the center-line and is given in units of [px]. The spatial *analytical signal* is a complex conjugated pair that consists of the signal $X(c)$ itself and the corresponding complex signal $Y(c)$. In its polar representation

$$Z(c) = X(c) + Y(c) = a(c)e^{i\phi(x)}, \tag{3.23}$$

the spatial analytical signal is determined by an amplitude function $a(c)$, i.e. the *instantaneous amplitude* of the signal, and its *phasing* $\phi(c)$. By definition an *analytic signal* has no negative-frequency components and thus is causal in the frequency-domain (Smith, 2007). As explained by Huang et al. (1999), there are an infinite number of definitions for the complex part of a real-valued signal, but there is only one unique way that makes (3.23) an *analytic signal*. In its integral form the HT of an arbitrary spatial signal $X(c)$ is defined by the convolution integral

$$Y(c) = \mathcal{H}_t\left(X\left(x\right)\right) = \frac{1}{\pi} P \int \frac{X\left(c'\right)}{c - c'} \mathrm{d}c'. \tag{3.24}$$

Where P is the *Cauchy principal value* (named after Baron Augustin Louis Cauchy, August 21, 1789 – May 23, 1857). In this equation P is introduced to avoid the singularity at $c' = c$. As described in detail by Tricomi (1951), the definition of the HT given in (3.24) is valid for all functions in the Lebesgue spaces (L^P).

The *instantaneous amplitude* $a(c)$ and the *instantaneous phasing* $\phi(c)$ of the polar representation of the spatial *analytical signal* can be computed from the complex conjugated pair $X(c)$ and $Y(c)$ using the following relations.

$$
\begin{aligned}
a\left(c\right) &= \sqrt{X^2\left(c\right) + Y^2\left(c\right)} \\[1em]
\phi\left(c\right) &= \arctan \frac{Y(c)}{X(c)}
\end{aligned}
\tag{3.25}
$$

Knowing the *instantaneous phasing* of a spatial signal $X(c)$ and its course, the *instantaneous frequency* of this signal can be derived from the first spatial derivative of its phasing.

$$f(c) = \frac{\mathrm{d}\phi\left(c\right)}{\mathrm{d}c} \tag{3.26}$$

The right image in Figure 3.3 on page 44 shows the result of the frequency analysis used in this work on the basis of a gray-value course extracted from a single streak. It was measured in a turbulent RB-convection using the setup presented in Chapter 4 of this thesis. The result of the EMD is illustrated on the right hand side of this figure. The blue crosses represent the gray-value information extracted by means of the center-line extraction algorithm (cf. Chapter 5). The red dashed line shows the non-periodical offset $o(c)$ computed in the EMD. The green and the yellow line illustrate that the sum and the difference of the offset and the *instantaneous amplitude* $a(c)$ build an envelope for the original signal. The *instantaneous frequency* $f(c)$ is plotted as a function of its position on the center-line.

The large deviations at the beginning and the end of the frequency signal are boundary effects that arise due to the convolution in (3.24). The high frequent modulations along the frequency signal are caused by numerical effects in the frequency computation.

Given the spatial *instantaneous frequency* along the center line of a particle streak and the constant illumination modulation frequency, the particle velocity can be computed using (3.18).

3.2 Bichromatic Depth Extraction

The development of a PSV technique that enables a bichromatic depth extraction and its implementation is one of the main achievements made in this dissertation. The depth extraction by means of the absorption of two different wavelengths due to an absorbing dye presents a simple, low price solution for particle based three-dimensional measurements of volumetric flow information.
As outlined in Section 2.2, this technique is especially useful for volumetric measurements of flow features in the boundary layer of an interface since all data are measured in a reference frame relative to the interface. This makes an additional interface tracking and a matching of the interface position and the measured flow information dispensable.

3.2.1 Basic Principle

The development of a two-wavelength method for absorption-based depth estimation was motivated by a method used in bio-fluid-mechanics (Debaene et al., 2005). In this study the exponential absorption-characteristic of an absorbing dye was used to extract the depth of tracer particles in a fluid. However, the intensity of the light that is reflected from the particles does not only depend on their depth as determined in Lambert-Beer's law (c.f (3.27)). It also depends on their reflectance properties. The latter are mainly dominated by the size of the particles and their coating. In (Debaene et al., 2005) great care was taken to use only particles of identical size. However, this is impractical for a number of applications and also error-prone. In illuminating the particles with two wavelengths, the distance of the particles from the interface can be computed directly from the intensity ratio of the reflected light independently of the reflectance properties.

The bichromatic depth estimation as introduced by Jehle and Jähne (2008) utilizes an absorbing dye and two light sources with different wavelengths λ_i, $i = \{1, 2\}$. In combination with a standard PIV approach it was successfully applied to the free air-water surface of a laminar falling film and a buoyancy-driven convective turbulence (Jehle and Jähne, 2008). The applicability of this measurement technique to real-world flow fields was proved by a comparison of the results obtained in the falling-film experiment with the theoretical prediction. In medical research the bichromatic approach was combined with an optical-flow based method to obtain interfacial flow fields in a displacement pediatric blood pump (Berthe et al., 2009). This study provides
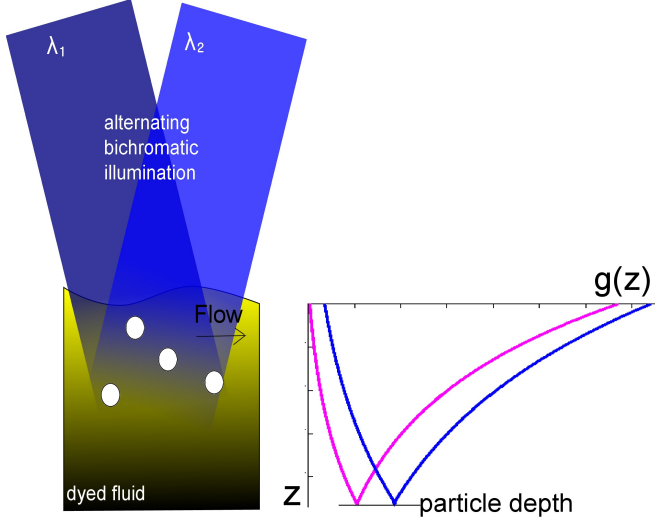
Figure 3.4: Schematic sketch of the volumetric two-wavelength illumination. Due to the different extinction coefficients ϵ_i of the dye for the wavelengths λ_i $i = 1, 2$ we introduced a second independent variable for a more robust computation of the particle depth.

a detailed analysis of the measurement errors of the absorption-based depth estimation on the basis of a single particle experiment and some simulated data sets.

The main idea of the bichromatic depth estimation is to choose a dye with a wavelength-dependent extinction coefficient ϵ_i that differs significantly for the wavelengths of the used light sources. For each wavelength λ_i, the intensity decay in the dyed liquid due to absorption can be described by Lambert-Beer's Law as function of the distance from the interface. Since this study concentrated on the horizontal air-water interface, this distance will be denoted hereafter by the depth z,

$$I(z, \lambda_i) = I_0(\lambda_i) \ \exp\left(-\frac{z}{\epsilon_i}\right). \tag{3.27}$$

Here $I(z, \lambda_i)$ is the intensity of the particle and $I_0(\lambda_i)$ is the intensity directly at the interface (i.e, at $z = 0$). In an ideal world with spherical, equi-sized tracer particles with equal reflectance properties, a perfectly homogeneous illumination and with a perfect camera, one wavelength would be enough to compute the depth of a certain particle from the logarithm of the reflected light. However since in a real world measurement all these deviations from a "perfect measurement" corrupt the depth estimation, we introduce a second light source with a different wavelength. Due to the different extinction coefficient of the second wavelength, its light is absorbed differently. This additional independent variable in the depth estimation enables more robust depth estimates.

By computing the intensity ratio of both wavelengths $I_1 = (z, \lambda_1)$ and $I_2 = (z, \lambda_2)$, the bias introduced by small variances in the particle size and the reflectivity cancels out and does not influence the quality of the depth estimation. Therefore, the depth

z results from:

$$z = \underbrace{\frac{z_{*1}z_{*2}}{z_{*1} - z_{*2}}}_{\gamma}\left(\ln\left(\frac{I_1}{I_2}\right) + \underbrace{\ln\left(\frac{I_{02}}{I_{01}}\right)}_{\kappa}\right),$$

$$z = \underbrace{\gamma\kappa}_{\text{offset}} + \underbrace{\gamma}_{\text{slope}}\ln\left(\frac{I_2}{I_1}\right). \tag{3.28}$$

This equation shows that the particle depth depends linearly on the logarithm of the intensity-ratio I_1/I_2.

This linear dependency can be described by an offset $\gamma\kappa$ and a slope γ. The offset is given by the incident intensities and the penetration depths of the dye for the given wavelengths. The slope γ only depends on these penetration depths z_{*1} and z_{*2}. Both variables γ and κ can be seen as constant during a measurement. Since they depend crucially on experimental parameters like dye concentration and absolute intensity of the LED-arrays, these parameter need to be measured previous to each measurement in a calibration experiment described in Chapter 4.

3.2.2 *bichromatic Particle Streak Velocimetry* (bPSV)

Since it is not possible to measure the intensity of both reflected light sources simultaneously, we have to illuminate the particles in an alternating way. To make sure that the information of both light sources was written along the particle streak structures, we tested two different intensity modulation patterns shown in Figure 3.5 on page 50.

The illumination pattern shown on the left hand side ensures that there are two positions in each period, when only one light source shines with its maximum intensity. To distinguish both wavelengths, the maximum intensity of the violet LED-array ($\lambda = 405\,\text{nm}$) was always chosen to be less bright than the blue LED-array ($\lambda = 465\,\text{nm}$) for all measurements that were recorded with this illumination pattern. Taking into account the higher extinction coefficient of the dye for violet light, it follows that the darker areas in the gray-value signal along the center-line of the particle streak correspond to the violet light source.

The second illumination pattern is shown on the right hand side of Figure 3.5. Here the intensity of one LED-array is modulated by a sinusoidal function while the other light source is shining with a constant intensity. This ensures that the minima in the gray-value signal on the center-line correspond to the intensity of the second light source, whereas the maxima are a superposition of both light sources shining with full intensity.
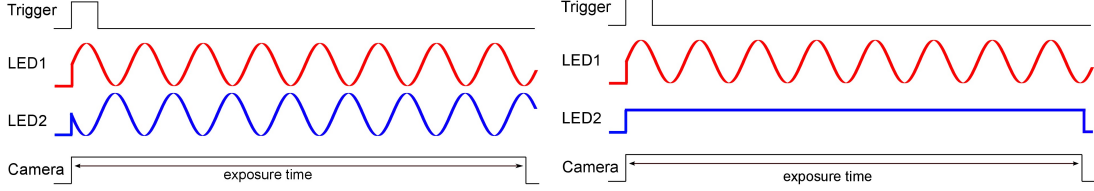
Figure 3.5: Two different trigger modi. *left: Illumination Pattern 1* When the trigger signal from the trigger board arrives, both LED-arrays are modulated with a phase shifted sinusoidal function. The 180° phase shift is used to ensure that there are two points where only one light source is turned on. The CCD-array of the camera integrating the incident light during the whole exposure time. *right: Illumination Pattern 2* The trigger signal causes one LED-array to start a sinusoidal modulated illumination while the other light source is set to a constant intensity.

For the computation of a reliable and continuous depth signal on the basis of (3.28), it is important to know the intensities of both light sources for every point on the center-line. These continuous intensity signals $I_1(c)$ and $I_2(c)$ are computed from the non-periodical offset $o(c)$ and the *instantaneous amplitude* $a(c)$ obtained in the HHT. The exact formula for the continuous depth signal $z(c)$ depends on the illumination pattern and can be derived as follows:

Illumination Pattern 1: In the first illumination pattern (cf. Figure 3.5, *left*), one light source intensity is given by the gray-value of the minima of the signal and one by its maxima. Therefore, the continuous depth signal can be computed from the sum and the difference of $o(c)$ and $a(c)$ using (3.28),

$$z(c) = \gamma\kappa + \gamma \ln \left(\frac{o(c) + a(c)}{o(c) - a(c)} \right). \qquad (3.29)$$

The courses of $I_2(c) = o(c) + a(c)$ and $I_1 = o(c) - a(c)$ are plotted in Figure 3.3 on page 44.

Illumination Pattern 2: For the second illumination pattern (cf. Figure 3.5, *right*) the first intensity I_1 that corresponds to the sinusoidal modulated light source is given by twice the amplitude of the gray-value signal, whereas the second intensity I_2 corresponds to the difference of offset and amplitude,

$$z(c) = \gamma\kappa + \ln \left(\frac{o(c) - a(c)}{2a(c)} \right). \qquad (3.30)$$

The resulting depth feature vector describes the course particle depth for each position on the streaks center-line. This particle streak feature is computed for all extracted streaks. It will be used as described in Section 3.4 to compute a spline representation of the three-dimensional trajectory of particles that were tracked over several bPSV images.

3.3 Plenoptic Depth Extraction

This section comprises the description of the second depth extraction technique used in combination with the developed PSV extraction algorithm. It uses a *focused plenoptic camera* that records four-dimensional light fields in long time exposure measurements.

3.3.1 *plenoptic Particle Streak Velocimetry* (pPSV)

The main idea that motivated the measurement series with a focused plenoptic camera was as follows:
A novel, single camera measurement technique for the measurement of volumetric flow information in an Eulerian frame of reference can be easily implemented by applying the developed PSV flow feature extraction on data measured by means of a plenoptic light field camera.

In contrast to the previously described approach that combines a bichromatic depth estimation with the developed PSV, this hybrid approach could be used to measure volumetric particle trajectories with a larger depth range, but in an Eulerian frame of reference. Therefore, this method is not suitable for the measurement of interfacial phenomena, but due to its intuitive simplicity it can be seen as a proper alternative to other state of the art *Particle Tracking Velocimetry* (PTV) approaches.

In this second series of experiments a *focused plenoptic camera* as described by Lumsdaine and Georgiev (2009) was used to sample four-dimensional light fields. For a summary of the basic principles that are used to acquire these light fields by means of plenoptic imaging, we refer to the introduction given in Section 2.3

Similar to the bichromatic approach, the exposure of the *focused plenoptic camera* was set to relatively long exposure times. From the resulting images, light fields were extracted using the rendering algorithms provided by the software-packages *RaytrixViewer* and *RaytrixLive* (Perwass, 2011). These algorithms are based on the principles of plenoptic imaging described in Section 2.3. In the context of this study we extracted two feature images from the recorded light fields:

"all-in-focus" images: These rendered images are computed by an adaptive algorithm, that locally corrects the plane of focus to obtain an image where all imaged objects (even those in different depth) are focused ("in-focus").

"depth-maps": Based on the angular information that is contained in the light field recordings, it is possible to compute a depth-map of the scene. In the *plenoptic Particle Streak Velocimetry* (pPSV)-approach, this information replaces the depth information obtained by means of the two-wavelength method.

For the illumination, a single blue LED-array ($\lambda_1 = 465\,\text{nm}$) was intensity-modulated using a sinusoidal function. The second (violet) light source ($\lambda_2 = 405\,\text{nm}$) was not used in these series of experiments since the pPSV-method does not rely on a bichromatic depth extraction.

For the evaluation of these measurements some minor adaptations of the existing particle streak extraction routine were necessary.

- For the streak extraction of particle streaks from the plenoptic light fields, the "all-in-focus" images were used as input for the streak-extraction routine. Since the rendering routine only produces 8bit images, the streak-extraction algorithms had to be adapted to enable both 8bit and 16bit precision in the gray-values.

- Since the bichromatic depth estimation was replaced by the stereo based approach used in the *RaytrixViewer* (Perwass, 2011), the intensity analysis described in Section 3.2 was replaced by a lookup function that connects the particle streak position with the depth-map.

The main distinction to the bichromatic depth estimation approach is that the measured flow information is in an absolute frame of reference and thus not measured relative to an interface. Furthermore, the obtained data comprise a much larger depth range. Therefore, the combination of a plenoptic camera with the presented particle streak technique using a frequency-based velocity estimation is insufficient for the measurement of interfacial processes in a relative frame of reference. Nevertheless, it presents a handy measurement technique for the volumetric measurement of flow characteristics in an environment, where other techniques that rely on a complex calibration of multiple view angle are difficult or impossible to apply.

To validate the applicability of this new camera technique in combination with the developed PSV approach, a set of test measurements were carried out in a turbulent Rayleigh-Bénard convection.

A summary of the results obtained in these series of measurements is given in Chapter 6 of this thesis.

For the bPSV measurements that were conducted in the context of this thesis a commercially available focused plenoptic camera (Model: RX11 by *Raytrix GmbH* (Perwass, 2011)) was used.
The image acquisition as well as the setting of frame-rate and exposure-time was controlled using the acquisition software *"RaytrixLive"*. A free version of this software is available on the web-page of the manufacturer (http://www.raydtrix.de) for demonstration purposes.
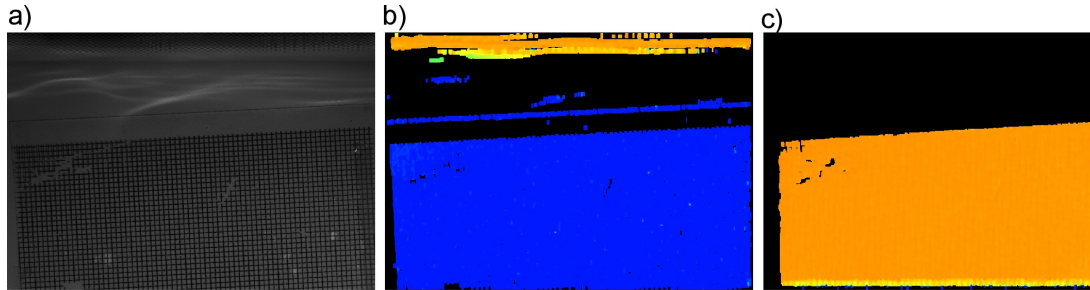
Figure 3.6: a) Focus corrected image of a mm-grid used as calibration target. The grid was placed in the principal focal plane at *depth0* (50 mm behind the interface air-water interface). **b)** Color-coded depth-map of the calibration target at *depth0*. Blue encodes information from deeper layers, and yellow indicates depths in the surface. In the upper part of this depth-map the water surface can be seen in yellow and orange. The depth information was computed from the light field images by a stereo algorithm provided by the camera manufacturer. **c)** Color-coded depth-map of the calibration target at *depth1* (directly at the position of the air-water interface).

Depth Calibration

For the depth calibration of the plenoptic camera, a calibration target with a mm-grid was placed in the principal focal plane of the camera. By focusing the camera objective on this plane, this is automatically the largest distance that can be measured. The light field of the target at this reference-depth is referred to as *depth0*. In the next step, the target is moved a known distance along the optical axes towards the camera, and a second calibration image (*depth1*) is recorded (c.f. Figure 3.6). These light field measurements of *depth0* and *depth1* are then used to scale the measured depth-maps computed by the stereo-algorithm of the manufacturer. In later versions of the calibration routine seven depths were used, and the scaling parameter was estimated in a least squares line-fit.

The focus-corrected images of the mm-grid were also used to correct the perspective projection distortion and to determine the pixel size. An image of the target with the mm-grid as well as a depth-map for *depth0* and *depth1* are shown in Figure 3.6 on page 53. The precision of the depth information extracted from the light field images is highly dependent on the performance of the depth estimation algorithm on the given data. For all feasibility measurements presented in this thesis a stereo based depth estimation algorithm was used that is part of the image acquisition software *"RaytrixLive"* (Perwass, 2011). Additionally, a calibration target with a random noise pattern was mounted on three inclined planes with known angles ($\alpha = [25° \pm 0.5°, 38° \pm 0.5°, 51° \pm 0.5°]$). The obtained depth-maps are shown in Figure 3.7 a). For the evaluation the depth signal was averaged over a width of 100 px perpendicular to the slope. Areas without depth information were ignored during the averaging. In the next step the change of the pixel size for different depths was estimated from the calibration

measurement	slope [°]	reconstructed slope [°]
slope1 (25Deg)	25 ± 0.5	25.29
slope2 (38Deg)	38 ± 0.5	37.46
slope3 (51Deg)	51 ± 0.5	52.21

Table 3.1: For an evaluation of the precision of the depth measurement, a random noise target was mounted on inclined planes with three different angles. The reconstructed slopes are summarized in this table.
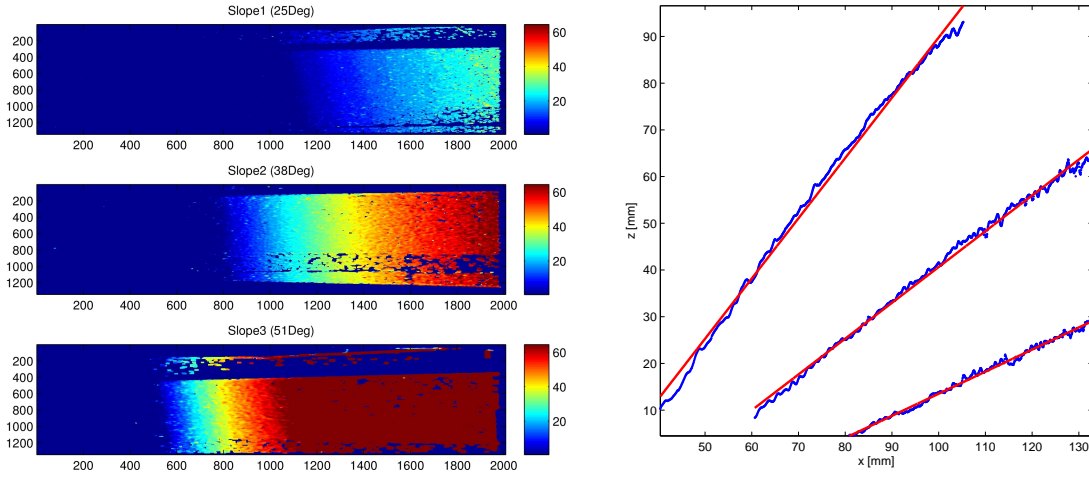

Figure 3.7: left: Color-coded depth-maps of three inclined plane calibration targets with a random noise pattern. The targets are inclined at the angles $\alpha = [25° \pm 0.5°, 38° \pm 0.5°, 51° \pm 0.5°]$ **right** The depth signal along the slope was corrected for a perspective distortion that causes a change of the pixel size in depth and calibrated using six depth measurements at known depths. The three red lines are the result of a linear fit and correspond to the angles $\tilde{\alpha} = [25.29°, 37.46°, 52.21°]$

measurements and the depth signals of the three slopes were corrected for this change. In the end the slopes were reconstructed from the depth signals using a simple linear fit. The reconstruction error of the three slopes is smaller than 2% of the measured depth (Shown in figure Figure 3.7 on page 54 and table Table 3.1 on page 54).

For all *focused plenoptic cameras* the depth range has the same size as the extended depth in the rendered "all-in-focus" images (cf. Section 2.3 on page 23). This focal depth depends on the geometrical arrangement of the camera objective, the micro-lens array and the detector of the camera. In the calibration measurements that were conducted during this thesis, we observed the following correlation between the horizontal dimensions and the depth that can be resolved by the plenoptic camera:

> The depth range of the *focal plenoptic camera* is always of the same
> order of magnitude as the horizontal dimensions of the imaged vol-
> ume.

This correlation between the dimensions of the measurement volume of the plenoptic
camera can only be changed by a general rearrangement of the optical components
within the *focused plenoptic camera*.

3.4 Lagrangian Trajectories

Since the image series recorded by the bichromatic PSV setup and the plenoptic PSV
setup only have small delays between subsequent exposures compared to the exposure
time, the information obtained from single images of the PSV series can be combined.
This is achieved in a matching procedure that combines extracted particle streaks from
multiple subsequent images. Due to this matching it is possible to track single tracer
particles over long periods in time.

Additionally, the inherent problem of directional ambiguity can be solved in the above
mentioned matching procedure. Up to now, it has only been possible to compute
the particle velocity course but not its sign, i.e. it has not been possible to indicate
whether a particle was moving in forward or backward direction. By incorporating
the information of the precursor image and the successor image, a streak matching
algorithm was developed that solves this directional ambiguity and tracks the tracer
particles through the recorded PSV-image stacks. One of the cornerstones of this
matching algorithm is the adaptive Mahalanobis distance that combines the Euclidean
distance information between the streak endings with other streak features to avoid
wrong matchings of particle streaks that correspond to different particles in the fluid.

The result of this matching are long streak trajectories. These trajectories describe
the horizontal paths of the imaged tracer particles by a combination of the center-lines
and a spline interpolation for the spaces between the streaks.

The particle depth and the velocity of the single streaks can also be merged using a
smoothing spline approach to obtain full 3D3C Lagrangian trajectories for the com-
plete measurement volume. On the basis of these trajectories, statistical measures like
acceleration statistics or particle pair dispersions can be computed to gain insight into
characteristics of the recorded flow field.

3.4.1 Particle Streak Matching

The goal of the particle streak matching is to find all sets of streaks structures in a
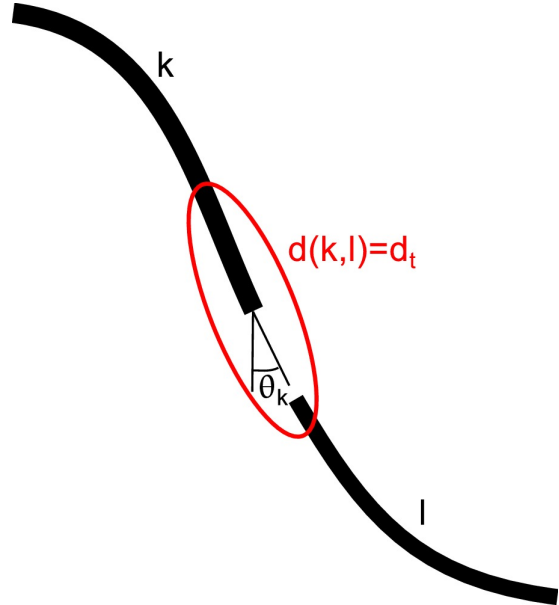PSV-image sequence that correspond to the same tracer particles. This is achieved

Figure 3.8: The adaptive Mahalanobis distance metric (3.32) is defined by an angle θ, a width scaling W and a length scaling L. Since it forms ellipsoidal equidistant lines, the threshold for a feasible assignment d_t also forms an ellipse (red line). In the matching routine a pair is assumed to be a feasible matching if their distance is smaller than d_t.

by a sequential algorithm that starts with the set of all streaks in the first image. All streak endings are used as seed points for trajectories. In the next step these seed points are combined with streak endings from the next image if their adaptive Mahalanobis distance is below a certain threshold. In the following iterations, all trajectories that have no member in the current image are disabled and all streaks in the current image that are not part of a trajectory are used to seed trajectories for the following iterations.

A more detailed description of this particle streak matching routine is given in Chapter 6 of this thesis.

3.4.2 Adaptive Mahalanobis Distance Metric

A central reason for the good performance of the matching algorithm is the used adaptive Mahalanobis distance metric. It allows a distance definition that is not only dependent on the Euclidean distance between two streak endings, but also incorporates the features of the involved particle streaks.

For a comparison of the proposed adaptive distance metric and the common Euclidean distance, we define the latter metric by the Euclidean norm of the distance vector as follows. The Euclidean distance $d_e\left(\cdot, \cdot\right)$ for two streak endings at the positions $\vec{e}_1 = (x_1, y_1)$ and $\vec{e}_2 = (x_2, y_2)$ is defined as

$$d_e\left((\vec{e}_1, \vec{e}_2)\right) = \sqrt{(\vec{e}_1 - \vec{e}_2) \cdot (\vec{e}_1 - \vec{e}_2)'}. \tag{3.31}$$

To implement a robust matching of particle trajectories in consecutive images, the matching routine uses the width σ and the orientation at the streak end (extracted from the *local orientation ϕ*) to define a proper distance measure and a threshold for a feasible trajectory matching. In a first step of the matching algorithm, both streak ends $\mathcal{E}_1 = \{\vec{e}_1, \sigma_1, \phi_1\}$ and $\mathcal{E}_2 = \{\vec{e}_2, \sigma_2, \phi_2\}$ at the end-point positions $\vec{e}_1$ and $\vec{e}_2$ are inspected. Based on the given features, an adaptive Mahalanobis distance metric $d\left(\cdot, \cdot\right)$ between two arbitrary streak endings k and l is defined by

$$
\begin{aligned}
d\left(\mathcal{E}_k, \mathcal{E}_l\right) \quad &= \sqrt{(\vec{e}_k - \vec{e}_l)^t (D^t M D)^{-1} (\vec{e}_k - \vec{e}_l)} \\[2mm]
\text{with } D \quad &= \begin{pmatrix} \cos\left(\phi_l\right) & \sin\left(\phi_l\right) \\ -\sin\left(\phi_l\right) & \cos\left(\phi_l\right) \end{pmatrix} \text{ and } M = \begin{pmatrix} L & 0 \\ 0 & W \end{pmatrix}.
\end{aligned}
\tag{3.32}
$$

For a visualization of this adaptive distance metric, Figure 3.8 on page 56 shows a single equidistant line (red line). One can clearly see that the orientation of the main axis of the ellipsoid formed by the equidistant line is inclined by the local orientation ϕ_l. The scaling of the distance metric in both directions (ϕ_l and $\phi_l + 90°$) is given by two independent parameters that are based on streak features. The variable W is the perpendicular scaling parameter which depends on the streak width σ and is defined to be $W = \frac{\sigma_k + \sigma_l}{2}$. In streak direction, the scaling parameter L was chosen to be proportional to the streak length.

By defining this adaptive distance metric, one can set a distance threshold $d\left(\cdot, \cdot\right) \leq d_t$ that allows much larger Euclidean distances in streak direction than perpendicular to θ_k, for a feasible matching of two streak ends.

As shown in Figure 3.9 on page 58, the definition of an adaptive non-isotropic distance metric causes the matching to favor streak assignments in streak direction. For a detailed description of the matching algorithm we refer to its pseudo code on page 101 in Chapter 5.

3.4.3 Lagrangian Trajectory Construction

A recorded streak-image sequence can now be used to successively put together a structure called trajectory. This structure consists of multiple particle streaks that originate from a set of subsequent streak-images. In the iterative matching routine, only streaks with an adaptive Mahalanobis distance smaller than d_t were merged to a trajectory.

The preliminary result of the previous chain of image processing and signal analysis operations are a set of feature vectors, each containing information about a single trajectory and the velocity of a single tracer-particle in the measurement. Each trajectory
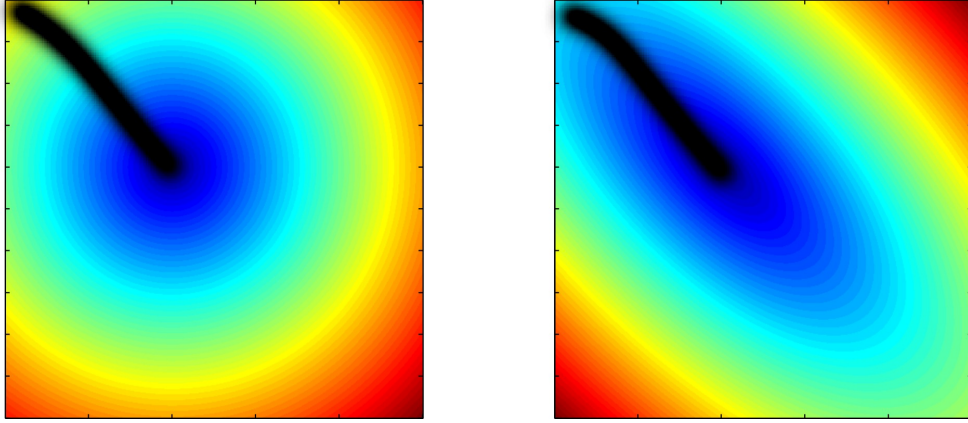
Figure 3.9: Comparison of the Euclidean and the adaptive Mahalanobis distance metric. In both images blue corresponds to low distance values and red indicates larger distances. The *left* image shows the color-coded Euclidean distance values around the ending of a streak (black line). The distances are distributed isotropically around the end of the streak. The image on the *right* hand side shows the non-isotropic distance distribution of the adaptive Mahalanobis metric, defined in (3.32)

feature vector is a set of several particle streak feature vectors corresponding to single images in the PSV-measurement.

Still there are several shortcomings in these feature vectors that need to be overcome. Firstly, the sampling of the horizontal position is equidistant for every single streak that is contained in a trajectory, but the gaps between the streaks introduce a non-equidistant sampling of the horizontal position along the center-line of the complete trajectory. This causes problems for two reasons:

1. The non-equidistant sampling of the feature vectors complicates the computation of derivatives by means of convolution with an appropriate filter kernel.

2. For the computation of time-dependent Lagrangian trajectories and the connected statistical measures, a functional description of the features is needed which defines all features for every point on the trajectory.

The second shortcoming in the feature vectors regards the depth and velocity information. Additionally to the previously mentioned sampling problem, these data are noisy and corrupted by larger measurement errors at the streak endings. These errors also shown in Figure 3.3 on page 44 are caused by boundary artifacts that occur during the convolution of the periodical gray-value signal with the Hilbert-Kernel.

A solution to both previously described shortcomings was implemented using a cubic spline function. This function allows a smooth interpolation of the horizontal information that yields a functional description for all points along the center-line of a

trajectory. On the other hand a smoothing spline can be used in a weighted regression to correct for the noise and errors at the streak endings in the depth signal and the in extracted velocity vectors.

Further details on the mathematical background and the routines used to compute the spline interpolation and the smoothing splines are given in Chapter 5.

After the computation of a spline interpolation and smoothing of all features in a trajectory's feature vector, an iterative sampling routine is used to compute the Lagrangian position $\vec{x}(t)$ and the Lagrangian velocity $v_h(t)$, from these functional descriptions of the 3d position $\vec{x}(c)$ and velocity $v_h(c)$. This is achieved by adding a time dependency to the position on the center line $c \in CL$. Starting with $t_0 = 0$ at the first point of the center-line $c(t = 0) = 0$, the Lagrangian variables are sampled in small, equidistant time-steps t_ϵ along the center line position c in the following way.

$$
\begin{aligned}
c(t + t_\epsilon) &= c(t) + v_h\left(c\left(t\right)\right) \cdot t_\epsilon & (3.33)\\
\vec{x}(t) &= \vec{x}\left(c\left(t\right)\right) & (3.34)\\
v_h(t) &= v_h\left(c\left(t\right)\right) & (3.35)
\end{aligned}
$$

Additionally to the three-dimensional Lagrangian particle position vector $\vec{x}(t)$, a three-component velocity vector is computed by decomposing $v_h(t)$ into v_1 and v_2. The third velocity component is given by the temporal derivative of the depth $v_3 = dz/dt$.

3.4.4 Trajectory Self-Validation Scheme

After the construction of each Lagrangian trajectory, we use the velocity from (3.35) for a self-validation. By integrating $v_h(t)$ over time, a *trajectory length* is computed. This length can be compared with the sum over the lengths of all streaks corresponding to the trajectory. A large difference between these two measures indicates an error in the velocity extraction or an incomplete trajectory. For the following experiments, we allow a maximal deviation of $10\,\%$. All trajectories that are above this threshold are rejected.

3.5 Lagrangian Particle-Pair Dissipation Statistics

As motivated in Section 2.1, Lagrangian two-particle dispersion statistics are a commonly used and intuitive statistical measure for the characterization of turbulent flow fields.
This statistical measure was first proposed by Richardson (1926) in a systematical study on isotropic turbulence. It is of fundamental importance for the understanding and characterization of many industrial applications and environmental processes. The Lagrangian pair dispersion rate characterizes for example the growth relative to the

center of mass of clouds in the atmosphere, contaminations in the ocean or chemical species in a turbulent reactor.

The computation of this characteristic measure on the basis of the Lagrangian trajectories $\vec{x}(t)$ is rather simple. According to the mathematical derivation given in Section 2.1 of this thesis, the Lagrangian two-particle dispersion can be computed from a set of Lagrangian trajectories. It is computed on the basis of a distance vector $\vec{R}(t)$ that describes the time-dependent Euclidean distance $d_c(\cdot)$ between the positions $\vec{x}_i(t)\, i \in \{1, 2\}$ of two tracer particles that are moved by a turbulent flow field and an initial distance $R(0) = r_0$.

$$\vec{R}(t) = \vec{x}_2(t) - \vec{x}_1(t) \tag{3.36}$$

The Lagrangian two-particle dispersion is defined as follows:

$$\langle |\vec{R}(t) - \vec{R}(0)|^2 \rangle_L. \tag{3.37}$$

In this equation $\langle \cdot \rangle_L$ denotes the average over an ensemble of Lagrangian particle tracks.

Since in the present approach all tracer particles are distributed randomly in the liquid, it is impossible to seed a set of particle pairs with an initial distance at random positions in the turbulent flow field.

In order to obtain a number of particle pairs that is large enough for valid Lagrangian statistics, all particle trajectories that coexist in at least one measurement of the PSV image series are extracted into a set of trajectory-pairs $\mathbf{P}$. For all trajectory-pairs $P_i \in \mathbf{P}$, the distance vector $\vec{R}_i(t)$ is computed in the next step using (3.36). Out of all members in $\mathbf{P}$, those were extracted that fulfilled $|\vec{R}_i(t_p)| = |\vec{x}_{i2}(t_p) - \vec{x}_{i1}(t_p)| \leq r_0$ at some point in time t_p. From this point in time until the trajectory-pair P_i does not longer coexist, this particle pair contributes to the Lagrangian average $\langle \cdot \rangle_L$ in (3.37).

A detailed description of the algorithms for the extraction of the Lagrangian particle pair dissipation behavior is given in Chapter 5 of this thesis. The results of the characterization of a turbulent Rayleigh-Bénard convection that was studied using the presented bPSV approach are given in Chapter 6.

4 Experimental Setup

The complete measurement setup, including all hardware components used in the experiments presented in this thesis, is described in detail in this chapter. Since two *Particle Streak Velocimetry* (PSV)-techniques based on different depth extraction techniques are presented in this work, this chapter introduces the *focused plenoptic camera* that was used in the *plenoptic Particle Streak Velocimetry* (pPSV) measurements as well as the gray-value camera that recorded the data in the *bichromatic Particle Streak Velocimetry* (bPSV) experiments.

The first section (Section 4.1) in this chapter focuses on the two-wavelength illumination arrangement that was installed to modulate arbitrary intensity signals on two *light-emitting diode* (LED) arrays. As described in Chapter 3, this intensity modulation is essential for the extraction of an instantaneous velocity from the PSV data sets. Besides, the two different wavelengths of the light sources are the basis for the absorption-based depth estimation used in the bPSV-approach.

The absorbing dye *Tartrazine* (E112) used to encode the particle depth by means of the two-wavelength illumination in the bPSV measurements is characterized in Section 4.2.

The third section (Section 4.3) comprises a detailed description of the cameras that were used to record the light fields for the plenoptic approach and the gray-value images used for an absorption-based depth estimation. In the following section (Section 4.4), all hardware components used for the synchronization of the image acquisition and the intensity modulation are described.

Section 4.5 gives a detailed description of the rectangular vessel that was purpose-built for the generation of a defined and stable turbulent *Rayleigh-Bénard* (RB) convection. This vessel was constructed and characterized in two bachelor projects by Niegel (2010) and Kunz (2011).

A schematic sketch of the hardware arrangement is shown in Figure 4.1 on page 62. The camera and the LED arrays are mounted on a measurement-platform that was placed approx. 30 cm above the interface. The optical axis of the camera is set to be perpendicular to the interface. To enable a homogeneous illumination of the volume of interest that lies in the boundary layer of the interface directly below the camera, the light sources are directed towards the measurement volume under the camera and defocused to a point far behind the volume of interest.

During the pPSV measurements a *focused plenoptic camera* was used and the measurement volume was only illuminated by a single LED array. In the bPSV measurements
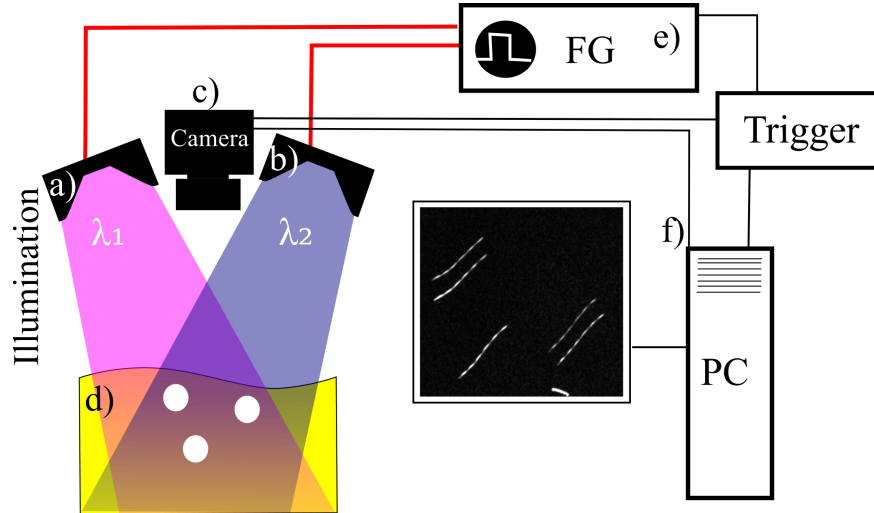
Figure 4.1: This figure shows a sketch of the experimental setup. a) and b) represent the LED arrays with $405nm$ and $465nm$; c) $5Mpx$ CCD camera that records 12bit gray-value images; d) measurement volume seeded with silver-coated hollow glass spheres with 100μm diameter and E112; the intensity modulation of both light sources and the synchronization with the frame-grabber is achieved by using an arbitrary function generator e) and a trigger card in the desktop PC used for the data acquisition.

both LED arrays were used, and the image sequences were recorded by a simple gray-value camera.

Previous to each bPSV experiment, the dye concentration is set to a value that causes a penetration depth of typically 1 cm. The exact absorption characteristic at this given concentration is determined by means of a calibration measurement described in Chapter 3.

After this calibration the fluid is seeded with neutrally buoyant silver-coated hollow ceramic spheres. These spheres have a mean diameter of 100μm and a mean density of $0.9 \pm 0.3 \frac{\text{g}}{\text{cm}^3}$ (Potters Industries Inc. Conduct-O-Fil® AGSL150-16TRD). The modulation function that controls the intensity of the LED light sources is generated as a voltage signal by means of an *Arbitrary Waveform Generator* (AFG). Afterwards this signal is converted to a current-signal by a purpose-built amplifier circuit board. The complete system is controlled by an automated *measurement-control-software* implemented on a *Personal Computer* (PC). This software sets all the parameters of the used hardware components and controls the synchronization of the periodical intensity signal and the image acquisition.

4.1 Illumination

For the intensity modulated illumination of the volume of interest, two very bright LED arrays (*ENFIS UNO Tile Array Blue 465 nm* and *ENFIS UNO Tile Array Violet 405nm*) were used. Each of these arrays consists of 5×5 LEDs that are mounted in a 9 mm $\times$ 9 mm grid on a circuit board. To ensure a fast removal of arising heat, the circuit board is attached to a copper plate.

The three main characteristics that have to be considered when choosing LED light sources for the volumetric illumination of a particle-based flow experiments are the following:

- The heat that arises because of thermal effects within the LED arrays has to be removed efficiently from the circuit board to avoid damage on the light sources and to guarantee a linear response of the intensity on the input-current.

- The intensity distribution of the light sources has to be constant in the complete volume of interest. Inhomogeneities of the light intensity may introduce measurement-errors especially in the absorption-based depth estimation used in the bPSV-measurements.

- The response-time of the light source on changes of the current has to be short. This is essential because long response-times would corrupt the intensity modulation used for the velocity estimation in the presented approaches.

For the removal of the expected thermal power that was estimated from the numbers given in the LED-data sheet (cf. Figure A.1 on page 161 and Figure A.2 on page 162), two fan-cooled aluminium heat-sinks (*C33224-002 Intel Socket-478 Cooler*) were mounted by means of thermal conductive glue on the backside of the copper plates of the LED light sources. A (*TRACOPOWER - TXL 025-12S - PSU, ENCLOSED, 25W, 12V*) power-supply was used to provide the current for the heat sinks of both LED arrays.

From the data in Table 4.1 on page 64, one can see that the input power P of both LED arrays is equal to 38 W. Assuming that all power which is not converted into photons remains as heat on the circuit board, the thermal power P_{therm} that needs to be removed by means of a cooling solution can be computed from the difference of the input power and the radian flux Φ_R.

$$P_{\text{therm}} = P - \Phi_R. \tag{4.1}$$

Therefore, a thermal power of $P_{\text{therm}}(405\,\text{nm}) = 32.900\,\text{W}$ has to be removed from the violet LED array, and a power of $P_{\text{therm}}(465\,\text{nm}) = 31.930\,\text{W}$ has to be removed from the backside of the blue LED array to avoid damage and to guarantee a linear response of the light sources over a long time. According to the data sheets, the chosen CPU

Item	$\lambda_1 = 405\,\mathrm{nm}$			$\lambda_2 = 465\,\mathrm{nm}$		
	min	typ	max	min	typ	max
Rated current $I_f[\mathrm{mA}]$		2000			2350	
Forward voltage $V_f[\mathrm{V}]$	16	19	22	14	16	20
Peak wavelength $\lambda_\mathrm{p}[\mathrm{nm}]$	400	405	412	450	465	470
Dominant wavelength $\lambda_\mathrm{d}[\mathrm{nm}]$				455	470	475
Spectral width $\Delta\lambda[\mathrm{nm}]$	10	16	22	15	23	30
Total radiant flux $\Phi_\mathrm{R}[\mathrm{mW}]$	4000	5100		4000	6070	
Radiant flux density $\Phi_\mathrm{R}/A[\mathrm{mW/cm^2}]$	8000	10200		8000	12140	
Total Luminous flux $\Phi_\mathrm{L}[\mathrm{lumens}]$	220	350				
Luminous flux density $\Phi_\mathrm{L}/A[\mathrm{lm/cm^2}]$	440	700				
Total electrical power $P[\mathrm{W}]$		38			38	

Table 4.1: Characteristics of the LED arrays (ENFIS Ltd., 2008a,b); A more detailed description of the characteristics of these LEDs is given in Figure A.1 on page 161 and Figure A.2 on page 162.

heat-sink accomplishes a cooling for processors up to $P = 100\,\mathrm{W}$ which is more than enough to remove the heat that is generated by the LED arrays.

As explained in Chapter 3, it is essential that the light sources used in the bPSV measurements have two wavelengths that cause a different absorption behavior by the used dye. As shown in Figure 6.2 on page 116 in Section 6.1, the precision of the depth estimate is much better for larger differences in the wavelength-dependent extinction coefficient $\epsilon(\lambda_i)$. The light sources used in this study were chosen in a way that their wavelengths are at positions in the extinction spectrum of the dye which have a large difference in the extinction coefficient (cf. Figure 4.3 on page 66).

4.1.1 Optical setup of the light sources

As visualized in the sketch of the experimental setup (cf. Figure 4.1 on page 62), the light sources were mounted on both sides of the camera. In order to ensure a homogeneous illumination of the volume of interest, a plan-convex lens was mounted in front of each LED array by means of a lens tube that was fixed on the copper-plate to avoid irritations by scattered light.
The focus of these lenses was set to a position far behind the volume of interest to achieve a flat, homogeneous illumination distribution. The optical axis defined by the LED arrays and the plano-convex f27 lenses in front of the arrays are inclined with respect to the optical axis of the camera to achieve a superposition ob both light sources in the measurement volume below the camera.
The homogeneity of the intensity distribution was tested by means of a white, diffuse

reflecting target placed in the volume of interest. Images that were recorded by means of the gray-value camera were used to evaluate the constancy of the irradiation in the measurement volume.

4.2 *Tartrazine* (E112)

For the absorption based depth-estimation in the bPSV-measurements, the food-dye *Tartrazine* (E112) was used. In other sources this dye is also called *Cl Food Yellow 4* or *FD & C Yellow No. 5*. It has a molecular weight of $534 \, \text{g/mol}$ and is typically available in form of orange powder. Solved in liquid, it educes a strong yellow color. The dye is easily soluble in water and sparingly soluble in ethanol (EFSA, 2009).

According to the detailed introduction in (EFSA, 2009), E112 consists essentially of "3-carboxy-5-hydroxy-1-(4'-sulphophenyl)-4-(4'-sulphophenylazo) pyrazole trisodium salt and subsidiary coloring matters together with sodium chloride and/or sodium sulphate as the principal uncolored components".

The small amounts of E112 used in the experiments during this study were purchased from the dye manufacturing company *Kremer Pigmente GmbH & Co. KG Hauptstraße 41-47, D-88317 Aichstetten/Allgäu.*

For a characterization of the extinction behavior, the absorption spectra of E112 were measured for different concentrations using a *HP 8453E UV-visible* spectrometer system. The acquired spectra are shown in the left image in Figure 4.3 on page 66

On the basis of these absorption measurements, the extinction-coefficients were determined. The measured extinction characteristic is plotted as a function of the wavelength on the right hand side of Figure 4.3 on page 66. These results reinforce the previously published measurements of the extinction behavior of E112 by Jehle (2006).

As shown in the plot of the extinction spectrum, E112 has different extinction-coefficients at the wavelengths of the LED arrays. For the illumination with the violet light source that has a peak-wavelength of $\lambda_1 = 405nm$ the extinction coefficient is given
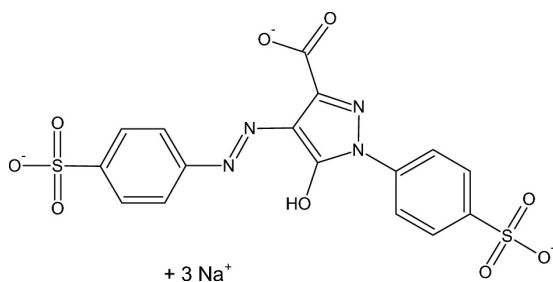
Figure 4.2: Structural formula of *Tartrazine* (E112), Stoichiometry: $C_{16}H_9N_4Na_3O_9S_2$, Molecular weight: $534.36 \, \text{g/mol}$, This image was taken from (EFSA, 2009).
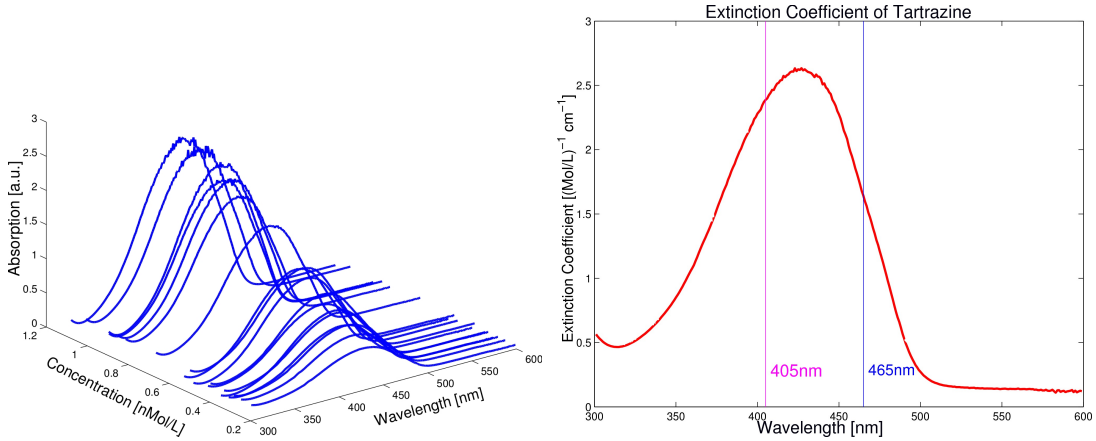
Figure 4.3: Absorption behavior of *Tartrazine* (E112). The absorption characteristic for various concentrations was measured by means of a *HP 8453E UV-visible* spectrometer system. On the basis of these absorption characteristics the wavelength-dependent extinction coefficient visualized on the right hand side was computed.

by $\alpha_{405\,\text{nm}} \approx 2.4 \frac{1}{(\text{mol/L})\text{cm}}$. The extinction-coefficient for the blue light source ($\lambda_2 = 465\,\text{nm}$) can be determined to be $\alpha_{465\,\text{nm}} \approx 1.6 \frac{1}{(\text{mol/L})\,\text{cm}}$.

Additionally to the difference in the absorption behavior, this dye has a row of other advantages that make it a suitable dye for the absorption-based depth-extraction by means of a two-wavelength illumination.

- In the dosage that is needed to restrict the measurement area to the upper centimeter under the interface, E112 is non-toxic in contact with human skin and even oral intake causes no harm (EFSA, 2009).

- Various in-vivo and in-vitro studies prove that E112 causes no mutagenic-effects on the genome (EFSA, 2009).

- Due to its high availability and its usage as a common food-dye, E112 is a low-cost solution.

A much more detailed characterization of this dye can be found in (EFSA, 2009). This study summarizes all technical data as well as the manufacturing process and the food-chemical background. Furthermore, it is an extensive characterization of its biological and toxicological characteristics.

4.3 Imaging Hardware

This section comprises a description of the two cameras and the additional imaging hardware used in the scope of this thesis for the acquisition of PSV image-series.

Item	Value	Comment
Chip	2/3" EXview HAD PS IT CCD	
Pixel size	$3,45\,\mu\mathrm{m} \times 3,45\,\mu\mathrm{m}$	
Resolution	2448×2050	(5 MPixel)
Depth range	$8/10/12\,\mathrm{bit}$	B/W
Framerate	15 fps	(Fullscan)
Power	over CameraLink	
Binning (1x2)	Vertical, Partial Scan	
Hardware Preprocessing	3×3-Filter	Built-in Test Pattern
Shutter	Normal / Trigger Shutter	
Weight	$130\,\mathrm{g}$	
Size	$44\,\mathrm{mm} \times 44\,\mathrm{mm} \times 57.5\,\mathrm{mm}$	(B x H x L)
General Purpose IO	1 x Trigger In, 4 x Output	
Additional features	Mirror Image, Binarization	

Table 4.2: Characteristics of the gray-value camera (*XCL-5005 B/W, Sony Electronics Inc.*). These data were taken from the data sheet (Sony Electronics Inc., 2008)

In all bPSV measurements that use the absorbing dye E112 and a two-wavelength illumination to resolve volumetric data, an industrial gray-value camera was used. The second camera that is presented in this section is a *focused plenoptic camera*. It was used for the measurement of four-dimensional light fields that were recorded in the pPSV experiments.

4.3.1 Gray Value Camera

The particle streak images of the bPSV-measurements were recorded using a 12 bit gray-value camera (*XCL-5005 B/W, Sony Electronics Inc.*) with 5 Mpx resolution. This camera-type is purchased for industrial image-acquisition purposes. An overview of the main features of the camera given by the manufacturer is summarized in Table 4.2 on page 67.

Additional camera-characteristics that provide a detailed description of sensor response were determined in a set of characterization measurements described in Chapter 5. The results of these characterization measurements are summarized in Section 6.1.

4.3.2 Camera Objective

For the acquisition of the bPSV image series, a Fujinon HF35SA-1 2/3" 35 mm camera objective was used. As described in the data sheet shown in the appendix chapter of this thesis (Figure A.4 on page 164), this objective was designed for the usage on

Item	Value
Effective resolution	3 MPixel
Sensor array	35 mm × 35 mm array with 10.7 MPixel; Interline-CCD-Sensor; Color/Mono
Depth resolution	30 - 100 different depth layers in the depth-maps; 3D stereo; Rendering of different view-points
Focal range	10× higher than with conventional cameras; Rendering of "all-in-focus" images
Framerate	Up to 10 fps via CameraLink, 6.2 fps via *Gigabit Ethernet* (GigE)
Depth range	8 bit and 12 bit
Interface	GigE and CameraLink
Objective mount	F-Mount / Nikon, Canon-Mount, M58
Hardware requirement	Microsoft Windows XP/Vista/7, NVIDIA GeForce GTX-580

Table 4.3: Key-features of the *focused plenoptic camera* (Model: R11, Raytrix GmbH, Kiel, Germany); These data were taken from the camera data sheet provided by the manufacturer (Raytrix GmbH, 2012) (cf. Figure A.5 on page 165).

5Mpixel cameras. The wide aperture (F1.4) enables the acquisition of clear images in low-intensity environments. Additionally, the manufacturer claims that this objective yields an enhancement of the image recognition accuracy by means of a reduced distortion and an improved uniformity of the sensor illumination.

By using this objective it was possible to image an interface patch of approx. 8 cm×8 cm by mounting the camera at distance of 30 cm above the air-water interface.

4.3.3 Plenoptic Camera

The *focused plenoptic camera* (Model: R11, Raytrix GmbH, Kiel, Germany) used in the pPSV experiments was provided by the manufacturer. The imaging principle that enables the recording of four-dimensional light fields by means of this camera, is explained in detail in Section 2.3. The camera was delivered in combination with a special macro-objective that had similar characteristics as the objective used in combination with the gray-value camera.

The main features of the *focused plenoptic camera* are summarizes in Table 4.3 on page 68. A more detailed description can be found in the data sheet of the camera (Raytrix GmbH, 2012) that is partially shown in Figure A.5 on page 165.

4.4 Synchronization

Since the synchronization of the light sources with the acquisition times and the exposure times of the imaging devices is of major importance for a proper velocity estimation, large effort was invested in the implementation of a synchronized measurement setup.

The basic components of the presented setup are the previously described illumination and image acquisition devices. For the interconnection and synchronization of these devices a trigger board, an *Arbitrary Waveform Generator* (AFG) and an *Operational-Transconductance-Amplifier* (OTA) were used.

A measurement-control-software was implemented using `Heurisko`® to control the setting and synchronization of frame-grabber and AFG as well as to store the recorded images in 16 bit *Tagged Image File Format* (TIFF) files. `Heurisko`® is a development environment for image processing and the automatization of measurement devices and cameras (AEON Verlag & Studio Walter H. Dorn e.K., 2012).

4.4.1 Trigger Board

A GPIO/Trigger Board (SILICONSOFTWARE GmbH, Mannheim, Germany) was used to provide a trigger signal to the AFG and to the *microEnable IV VD4-CL* frame-grabber (SILICONSOFTWARE GmbH, Mannheim, Germany). A data sheet containing the main characteristics of the frame-grabber card is shown in Figure A.7 on page 167 in the appendix chapter of this thesis.
This external triggering of the frame-grabber and the AFG by means of an extra trigger board ensures that the image acquisition and the modulation of the light sources are perfectly synchronized. To reduce the response time, the trigger-board is directly connected to the frame-grabber card. The signal to the OTA is conducted by a short copper co-axial cable.

4.4.2 *Arbitrary Waveform Generator* (AFG)

A two-channel AFG (*AFG3102, Tektronix Inc., Beaverton, United States*) was used for the generation of two periodical signals. This device allows the definition of two independent arbitrary voltage signals generated at the two output channels. It also provides a trigger input that enables a synchronization of the output signals with the camera.
For all experiments that were implemented in this study, the AFG was set to the "external trigger mode". This means that for an incoming trigger signal at the trigger-input connector, the AFG starts sending two previously defined voltage signals to the outputs *CH1* and *CH2*.
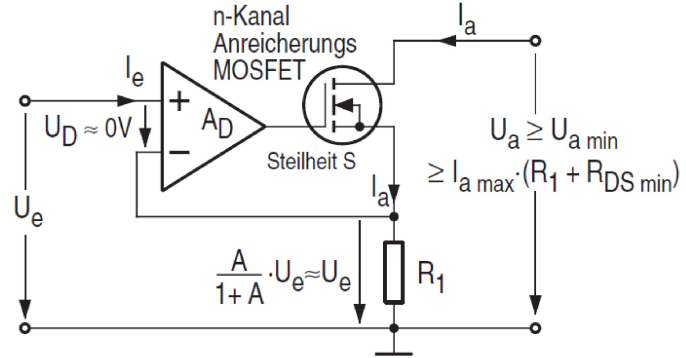
Figure 4.4: Simplified scheme of the *Operational-Transconductance-Amplifier* (OTA). A complete scheme of the circuit board is shown in Figure A.6 on page 166. This image was taken from (Lauffs et al., 2011).

The diagram contains the following labels and equations:

n-Kanal Anreicherungs MOSFET

I_e, I_a

$U_D \approx 0V$, A_D

Steilheit S

U_e

$U_a \geq U_{a\,min}$

$\geq I_{a\,max} \cdot (R_1 + R_{DS\,min})$

$\frac{A}{1+A} \cdot U_e \approx U_e$, R_1

$$E = \frac{I_a}{U_e}\bigg|_{U_e \geq 0V} = \frac{A}{1+A} \cdot \frac{1}{R_1} \approx \frac{1}{R_1}$$

$$R_e \approx r_e = \frac{\Delta U_e}{\Delta I_e} = (1+A) \cdot r_D \parallel r_{Gl}$$

$$R_a \approx r_a = \frac{\Delta U_a}{\Delta I_a}\bigg|_{\Delta U_e = 0V} \approx S \cdot r_{DS} \cdot A_D \cdot R_1$$

The amplitudes of these voltage signals control the brightness of the LED-light sources. The duration of the sent voltage signal is exactly as long as the exposure time of the camera.

During the bPSV measurements voltage signals were used that generated the two illumination patterns shown in Figure 3.5 on page 50. Here each light source was controlled by one channel of the AFG. Since for the pPSV-measurements only one light source was sufficient, in these experiments only the blue LED array was controlled by the AFG that sent a simple sine function.

4.4.3 *Operational-Transconductance-Amplifier* (OTA)

For the amplification of the voltage signals that were generated by means of the AFG into voltages sufficient to drive the LED arrays, a two-channel amplifier was built. As shown in Figure A.6 on page 166 in the appendix chapter of this thesis, each channel in the amplifier uses an OPA2350 (*High-Speed, Single-Supply, Rail-to-Rail Operational Amplifiers MicroAmplifier®*), an IRF520 (*IRF520 MOSFET N Channel Transistor*) and a power supply unit (*TRACOPOWER - TXL 120-24S - PSU, METAL, 120W, 24V/5A*) to generate a current signal that is proportional to the input-voltage of the channel. The Amplifier was dimensioned for input signals $U_e \in (0\,\mathrm{V} \ldots 5\,\mathrm{V})$.

Since both channels of the implemented OTA are identical, we focus on a single channel in the following description.

As shown in the simplified sketch in Figure 4.4, the built amplifier uses a transistor and a resistor to realize a voltage controlled current source. In this electric circuit the potential at R_1 is nearly as large as the input voltage U_e. The current that flows through R_1 is therefore given by U_e/R_1. The output current I_a controlled by the IRF520 transistor is as large as the current through R_1. On the basis of this wiring the amplifier only works properly if the applied voltage at the output U_a is larger than the potential that arises at R_1.
Due to losses in the *Operational Amplifier* (OA) the amplification A of this circuit is alway a little bit smaller than A_D.

The output of each channel of the OTA-amplifier was connected to the corresponding LED array. To avoid a damage of the light sources, the voltage of the power supply unit that provides the support-current for the amplifier was set to $U_{\max} = 21\,\text{V}$. This is the upper limit of the voltage range defined in the data sheets of the LED arrays (cf. Figure A.1 on page 161 and Figure A.2 on page 162)

Varying the input voltage provided by the AFG therefore directly results in a variation of the output current. Within the limits this output current causes a linear response of the light sources.

4.5 Convection Experiment

For the generation of a well defined turbulent RB-convection a rectangular vessel with the dimensions ($H = 147\,\text{mm}$, $L = 405\,\text{mm}$, $W = 415\,\text{mm}$) was built from $3.3\,\text{mm}$ thick BOROFLOAT® glass. This vessel was dimensioned and constructed within the scope of a bachelor thesis by Niegel (2010). In a later bachelor thesis by Kunz (2011), the vessel was characterized by means of a set of thermographic measurements, and the gas-exchange through the air-water interface was measured quantitatively.

For the heating a mirrored box with two infrared heating tubes (Heraeus Noblelight, Art.Nr.: 45132877), with $P_{max} = 1\,\text{kW}$ and $T_{max} = 1.2 \cdot 10^3\,°\text{C}$ each, was mounted under the vessel as shown in Figure 4.5 on page 72. Due to the high transmission of 93% at wavelengths between $2.0\,\text{nm}$ and $2.7\,\text{nm}$, most of the infrared light penetrates the bottom plate of the vessel and is absorbed within the first mm of the water body. The cooling at the water surface is mostly due to evaporation and radiation.

In all experiments the vessel was filled up to a height of $\tilde{H} = 50\,\text{mm}$ and the heating power was set to 945W. Measurements were conducted once the system reached its state of equilibrium at a water temperature of $T \approx 51°\text{C}$. The temperature difference $\Delta T = 23.6°\text{C} \pm 0.3°\text{C}$ between the bottom plate and the air directly above the water surface was measured by a *Pt100 thermo sensor* using a *GMH 3710 thermometer*

Figure 4.5: Sketch of the convection vessel used to generate the turbulent RB-convection. The side walls and the bottom plate a) consist of 3.3 mm thick BOROFLOAT® glass, which is nearly transparent for the infrared light, radiated from the heating tubes d). All sidewalls of the box containing the heating elements are mirrored to reflect the infrared light to the bottom plate of the vessel where it is absorbed in the first few mm of the water-body b), since water behaves like a black-body for infrared light.
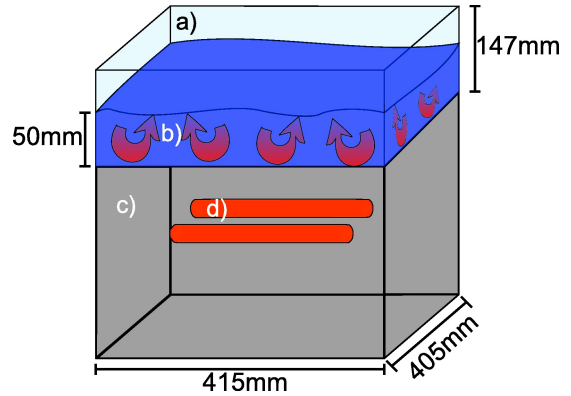
(GREISINGER electronic GmbH). All temperature measurements were averaged over several minutes. The absorbing dye Tartrazine was added to the liquid from a stock solution with 1g Tartrazine per liter, to obtain a concentration of $12 \, \mathrm{mg/l}$ Tartrazine in the water. This concentration enables a particle extraction down to the depth of 10 mm below the interface.

For the seeding we used neutrally buoyant silver-coated hollow ceramic spheres with a mean diameter of $100 \, \mu m$ and a mean density of $0.9 \pm 0.3 \, \mathrm{g/cm^3}$ (Potters Industries Inc. Conduct-O-Fil® AGSL150-16TRD). These tracer particles were sorted in advance based on their sedimentation behavior in water to obtain a narrower density distribution. During the experiment the measurement setup was covered with light absorbing material to ensure that the light that is reflected by the particles only originates from the LED arrays.

5 Data Processing

This chapter comprises a detailed description of all computational operations that were applied to extract Lagrangian flow information from both *Particle Streak Velocimetry* (PSV) techniques presented in this thesis. To illustrate the interaction between the different algorithms, Figure 5.1 on page 74 shows a schematic workflow of the implemented routine. The 12bit image sequences that were recorded using the *bichromatic Particle Streak Velocimetry* (bPSV)-setup and the plenoptic PSV sequences are processed sequentially for the extraction of all streak features, i.e. the *three-dimensional* (3d) position of the center-line, the intensity course along this line and the streak velocity.

In a first preprocessing step (Step I) that is only needed for the bPSV measurements, a radiometric characterization of the gray-value camera was carried out in accordance to the *European Machine Vision Association* (EMVA) standard *EMVA1288* (EMVA, 2010). On the basis of the extracted camera characteristics, a radiometric calibration of the raw-data was developed. Furthermore, the characteristics provide a detailed insight in the expected measurement uncertainty that is introduced by the camera-artifacts such as *array non-uniformities*, variations in the *spectral sensitivity* and the *linearity* of the *charge-coupled device* (CCD)-sensor.

The following operations belong to the feature extraction (Step II). Here the first image processing step in the feature extraction routine is a background subtraction on the basis of a temporal median filter. The basic assumption of this background removal strategy is that each pixel position contains a background signal in at least 50 % of the recorded images in a bPSV-sequence. Thus, a temporal median of each pixel is a local and robust estimation of a background signal that can be subtracted from all images in the sequence. The following extraction of the center-lines and the intensity courses along these lines was implemented by means of an iterative routine based on the gray-value information itself and a number of low-level image features computed using a rotation-invariant second order tensor approach. The last operation that is performed on each image individually is the computation of particle depth and its velocity from the gray-value information for all positions along the center-lines. All image processing operations and feature extraction routines are explained in Section 5.2.

(Step III) comprises the following operations that process the whole set of particle streaks that were extracted from a complete bPSV image-sequence. Here streaks from subsequent images that belong to the same particle are grouped to obtain long trajectories. Each trajectory describes the movement of a single tracer particle over a long

Figure 5.1: Schematic overview of the algorithmic components used in the analysis framework. In the feature extraction part (dashed rectangle) all images are processed individually to extract single streak-patters. In the analysis of the Lagrangian flow features, information of all extracted streak-patterns is merged to obtain long trajectories that are represented by a set of streaks from subsequent images that belong to the same tracer-particle.
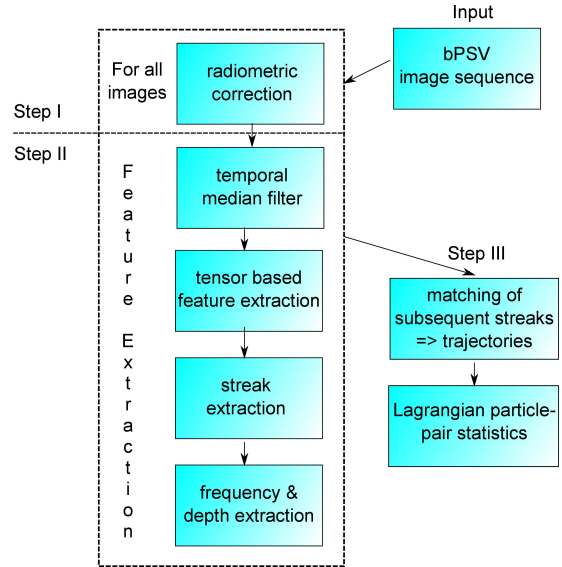
period in time.

Afterwards these long trajectories are used to extract Lagrangian flow features that are based on single particles and particle pairs as described in Section 5.3. Finally, to prove the applicability and to show the performance of the velocity estimation, we generated a set of semi-artificial data generated by a temporal integration (cf. Section 5.4) of a *Particle Image Velocimetry* (PIV)-benchmark data set proposed by Berthe et al. (2010).

5.1 Step I: Radiometric Camera Calibration

A radiometric correction of the measured particle streak images recorded in the bPSV measurements is of major importance since artifacts caused by non-uniformities of the CCD array or non-linearities have a direct influence on the extracted particle depth. Additionally, these artifacts may also corrupt the results of the center-line extraction and therefore the quality of extracted center-line data. This may even cause larger uncertainties in the result of the frequency analysis.

To allow a proper correction, an accurate measurement of the camera characteristics is necessary. The camera characterization-setup used in this study was purpose-built to fulfill the EMVA1288 standard that defines a characterization for monochrome and color digital cameras with linear photo-response characteristics (EMVA, 2010).

a)

A number of photons ...

... hitting the pixel area during exposure time ...

... creating a number of electrons ...

... forming a charge which is converted
by a capacitor to a voltage ...

... being amplified ...

... and digitized ...

42 ... resulting in the digital gray-value.

b)
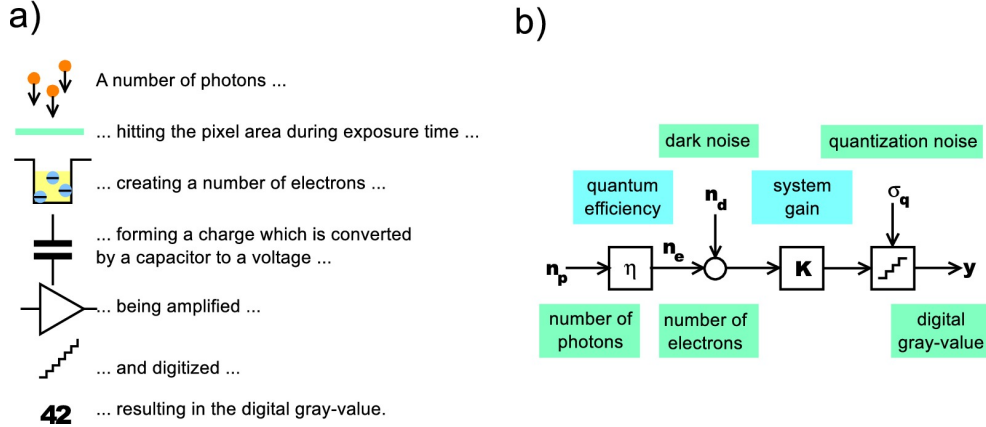
Figure 5.2: EMVA1288 model of a camera with linear photo-response characteristic. a) illustrates the processes that convert an incident photon into a digital gray value. b) shows the linear signal model for the mapping of a photon-count n_p to a digital gray-value y (EMVA, 2010).

5.1.1 Linear Signal Model

The basic assumption of the linear model that was used to describe the imaging process is that the number of photons that are measured by a single pixel of the sensor array depends only on the irradiance E [W/m²] and the exposure time t_{exp}[s]. As a result the radiative energy-density Et_{exp}[J/m²] only depends on these two variables. The second assumption made in the linear signal model is that the digital signal at the output is directly proportional to the number of collected photons.

To motivate the linear model for digital imaging sensors visualized in Figure 5.2, we focus on the processes that participate in the conversion of photons that hit a pixel of the CCD-array into a discrete gray-value given by a *digital number* (DN). Considering an absolute number of μ_p photons that hit the surface of a single detector pixel during the exposure time t_{exp}, the number of electrons μ_e that are released as a result of the photon impact depends on the *total quantum efficiency $\eta(\lambda)$*

$$\eta(\lambda) = \frac{\mu_e}{\mu_p}. \tag{5.1}$$

It has to be pointed out that the correlation between the radiative energy density and μ_p as well as the total quantum efficiency depend on the wavelength λ of the irradiating light. As described in detail in (EMVA, 2010), the number of photons can be computed using

$$\mu_p(\lambda) = \frac{AEt_{exp}\lambda}{hc}. \tag{5.2}$$

In this equation $A[\mathrm{m}^2]$ is the surface of a single pixel, $c \approx 2.9979 \cdot 10^8$ m/s is the speed of light, and $h \approx 6.6260 \cdot 10^{34}$ Js is Planck's constant. Additional to the electrons that

were released by the impact of photons on the sensor surface, thermal effects inside the pixels release a number of electrons μ_d. All electrons that were accumulated during the exposure time are converted into a voltage that can be amplified and converted to a digital number by an *analog digital converter* (ADC). The factor of proportionality between the total number of electrons released in the sensor $(\mu_e + \mu_d)$ and the digital signal μ_y [DN] is the *overall system gain* $K[\text{DN}/\text{e}^-]$

$$\mu_y = K \left(\mu_e + \mu_d \right). \tag{5.3}$$

In accordance to (EMVA, 2010), it is possible to summarize the foregoing into a single linear model by substituting the dark signal $\mu_{y.\text{dar}} = K\mu_d$ using (5.1), (5.2) and (5.3):

$$\mu_y = \mu_{y.\text{dark}} + K\eta\left(\lambda\right)\mu_p\left(\lambda\right) = \mu_{y.\text{dark}} + K\eta\frac{\lambda A}{hc}Et_{exp} \tag{5.4}$$

One of the main ideas of the this standard is to determine the *photo responsivity* $R = K\eta[\text{DN}/\text{photon}]$ by measuring the gray-value change corresponding to defined intensity-changes of the irradiant light field.

For all calibration measurements, a so-called Ulbricht sphere, i.e. a spherical hollow cavity that is coated with a highly diffusive reflecting interior, was used that complies the standard. This allows a homogeneous illumination of the camera sensor that was mounted directly, i.e. without any optics, on the Ulbricht sphere.

For the illumination three *light-emitting diode* (LED)-light sources were used (*Red Green Blue* (RGB)). The irradiance at the orifice of the sphere was characterized in advance using a calibrated photo diode. The mean gray-values μ_y as well as the mean gray-values of the recorded dark-image $\mu_{y.\text{dark}}$ were computed from two $M \times N$ images y^A and y^B that were captured at each irradiation intensity using

$$\mu_y = \frac{1}{2NM} \sum_{m=0}^{M-1} \sum_{n=0}^{N-1} \left(y^A\left(m,n\right) + y^B\left(m,n\right) \right). \tag{5.5}$$

On the basis of (5.5), we can plot the responsivity curve (shown in Figure 5.3 on page 78 *left hand side*) that visualizes the correlation between the photon-induced gray-values and the number of photons that hit a single sensor element. The previously mentioned responsivity R of the imaging system is a wavelength depended characteristic that can be estimated separately from the slope of the responsivity curve for each light source (RGB).

5.1.2 Noise Model

Next to the linear signal model, the universal noise model introduced in (EMVA, 2010) is an important assumption on the way to a general CCD-camera calibration standard.

The main noise-sources assumed in the standard are the so-called *shot noise* σ_e^2, the noise caused by internal readout and amplification operations σ_d^2, and the discretization noise caused by the ADC σ_q^2. The first mentioned noise-source is caused by statistical fluctuations of the number of electrons μ_e. The reason for this noise are quantum mechanical processes that yield a Poisson distribution of the number of charge units around its mean. Therefore, the variance σ_e^2 can be computed from the mean electron count

$$\sigma_e^2 = \mu_e. \tag{5.6}$$

The noise caused by the quantization in the ADC was derived theoretically in (Jähne, 2005) to be $\sigma_q^2 = \frac{1}{12}$ DN. Afterwards the noise model proposed in (EMVA, 2010) makes the reasonable assumption that the variances of all noise-sources add up linearly. This assumption yields a functional description of the total temporal signal variance σ_y^2 of the resulting signal y that is given by:

$$\sigma_y^2 = K^2 \left(\sigma_d^2 + \sigma_e^2 \right) + \sigma_q^2. \tag{5.7}$$

By inserting (5.3) and (5.6) in (5.7), it is possible to express the total noise that is described by the model in relation to the mean of the measured digital signal:

$$\sigma_y^2 = \underbrace{K^2 \left(\sigma_d^2 + \sigma_e^2 \right)}_{\text{offset}} + \underbrace{K}_{\text{slope}} \left(\mu_y - \mu_{y.\text{dark}} \right). \tag{5.8}$$

This dependency is one of the basic assumptions of the *photon transfer method* described by Janesick (1985) and Jähne (2005). Therefore, it is also of crucial importance for the characterization of digital imaging sensors that have a linear photo response behavior according to the EMVA1288 standard. The proportionality between the variance of the signal σ_y and the mean (photon induced) gray-value $\mu_y - \mu_{y.\text{dark}}$ is shown in Figure 5.3 on page 78 *(on the right hand side)*.

The proportionality factor of this linear dependency is the overall system gain K, and the offset can be used to compute the dark noise variance σ_d^2. Furthermore, the saturation gray-value of the imaging system $\sigma_{y.\text{sat}}$ was obtained from the maximum of the photon-induced variance illustrated by the cyan colored line in the photon transfer curve (cf. Figure 5.3 on page 78). Additionally, the average of the wavelength dependent *quantum efficiency* can be computed from the ratio of responsivity R and the overall system gain K as follows:

$$\eta = \frac{R}{K}. \tag{5.9}$$

The error of η can be propagated to be

$$\Delta\eta = \sqrt{\left(\frac{\partial z}{\partial R} \Delta R \right)^2 + \left(\frac{\partial z}{\partial K} \Delta K \right)^2}. \tag{5.10}$$

All sensor characteristics that were obtained using the *photon transfer method* are summed up in Table 5.1 on page 78.
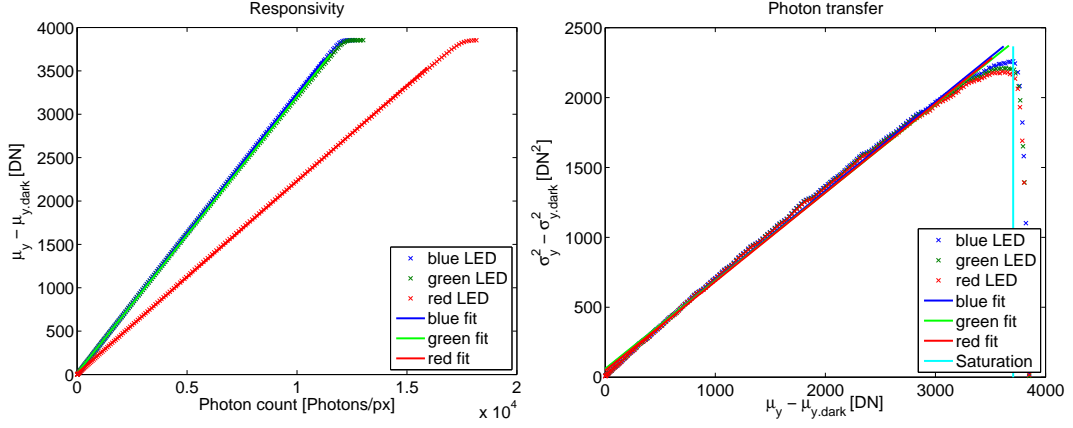
Figure 5.3: *Left:* Photo Responsivity curve of the sensor showing the photon induced gray-values as a function of the number of irradiated photons. The slope of this curve is the responsivity $K\eta$. *Right:* Photon Transfer curve visualizing the connection between the photon induced signal variance and the photon induced gray-value. The slope can be used to compute the overall system gain K.

Color	$\mu_{y.\mathrm{dark}}[\mathrm{DN}]$	$\mu_{y.\mathrm{sat}}[\mathrm{DN}]$	$K[\mathrm{DN/e^-}]$	$\eta[\mathrm{e^-/Photon}]$
red			$(636.3 \pm 2.3) \cdot 10^{-3}$	$(347.9 \pm 1.3) \cdot 10^{-3}$
green	241 ± 38	$3.7060 \cdot 10^3$	$(630.6 \pm 2.7) \cdot 10^{-3}$	$(505.2 \pm 2.2) \cdot 10^{-3}$
blue			$(638.6 \pm 2.3) \cdot 10^{-3}$	$(505.5 \pm 1.8) \cdot 10^{-3}$

Table 5.1: Summarized results from the EMVA1288 characterization of the used imaging sensor.

5.1.3 *Signal-to-Noise Ratio* (SNR) & Dynamic Range

The most common parameter for the characterization of the quality of an image is the *Signal-to-Noise Ratio* (SNR). It is defined by the ratio of the photon-induced gray-value and its variance

$$\text{SNR} = \frac{\mu_y - \mu_{y.\text{dark}}}{\sigma_y}. \tag{5.11}$$

As described in detail in EMVA (2010), we can make use of the information obtained from the linear signal model (5.4) and the noise model (5.7), and define the SNR as follows:

$$\text{SNR} = \frac{\eta\mu_p}{\sqrt{\sigma_d^2 + \sigma_q^2 K^{-2} + \eta\mu_p}}. \tag{5.12}$$

By analyzing the SNR-characteristic separately for the cases of high irradiation and low irradiation, one obtains a linear correlation when the number of photon-induced electrons is small compared with the sum of thermal variance and quantization noise. If, on the contrary, the number of photon induced electrons is much higher, the SNR shows a slower square root increase. These cases are described by the following approximation

$$\text{SNR} \approx \begin{cases} \sqrt{\eta\mu_p} & \text{if } \eta\mu_p \gg \sigma_d^2 + \sigma_q^2 K^{-2} \\[2ex] \frac{\eta\mu_p}{\sqrt{\sigma_d^2 + \sigma_q^2 K^{-2}}} & \text{if } \eta\mu_p \ll \sigma_d^2 + \sigma_q^2 K^{-2} \end{cases} \tag{5.13}$$

This transition from a linear behavior to a square root increase can also be seen in the SNR graph in Figure 5.4 on page 80. The SNR graph also shows the lower signal threshold at SNR = 1 and the previously estimated pixel saturation threshold $\mu_{y.\text{sat}}$ of the photon transfer curve.

For a computation of the *minimum detectable irradiation*, i.e. the number of photons that is required to measure data with a SNR that is equal to one, an inverse formulation of (5.12) is needed. Using this inverse formulation

$$\mu_p(\text{SNR}) = \frac{\text{SNR}^2}{2\eta}\left(1 + \sqrt{1 + \frac{4\left(\sigma_d^2 + \sigma_q^2/K^2\right)}{\text{SNR}^2}}\right), \tag{5.14}$$

it is possible to compute the gray-value that is necessary to reach a certain SNR.

Figure 5.4: The *Signal-to-Noise Ratio* (SNR)-plot shows the SNR characteristic of the gray-value imaging sensor for the illumination with three different colors. In comparison, the green line shows the characteristic line of an ideal sensor in which only the *shot noise* with $\sigma_p = \sqrt{\mu_e}$ corrupts the imaging process. The pixel saturation threshold $\mu_{y.\mathrm{sat}}$ is indicated by the blue vertical line, and the noise threshold (SNR = 1) is shown as a cyan colored horizontal line.
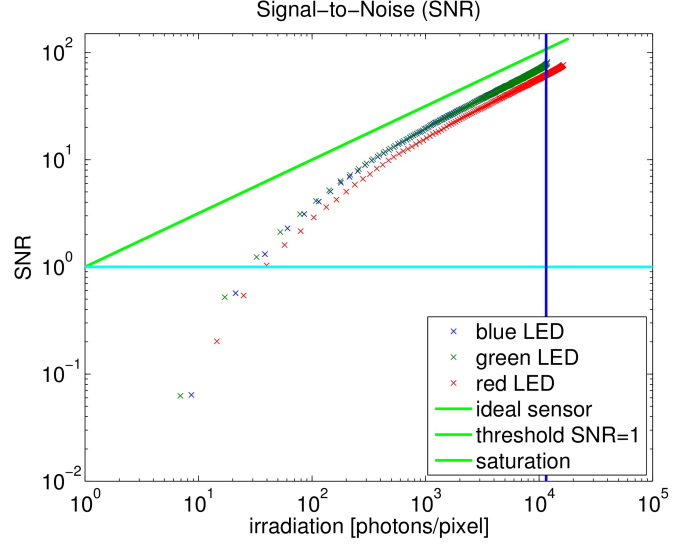
In the description of the EMVA standard, two approximations of (5.14) were made. One approximation describes the limit for large SNR values, and the other gives approximates $\mu_p(\mathrm{SNR})$ for small SNR values.

$$
\mu_p(\mathrm{SNR}) \approx
\begin{cases}
\frac{\mathrm{SNR}^2}{\eta} \left(1 + \frac{\sigma_d^2 + \sigma_q^2/K^2}{\mathrm{SNR}^2} \right), & \mathrm{SNR}^2 \gg \sigma_d^2 + \sigma_q^2/K^2 \\[2ex]
\frac{\mathrm{SNR}}{\eta} \left(\sqrt{\sigma_d^2 + \sigma_q^2/K^2} + \frac{\mathrm{SNR}}{2} \right), & \mathrm{SNR}^2 \ll \sigma_d^2 + \sigma_q^2/K^2
\end{cases}
\tag{5.15}
$$

The camera that was used in the bPSV-measurements in this study is well described by the second case since $\sigma_d^2 + \sigma_q^2/K^2$ is much larger than one.

Therefore, an absolute sensitivity threshold of the imaging device can be approximated using:

$$
\mu_p(\mathrm{SNR} = 1) = \mu_{p.\mathrm{min}} \approx \frac{1}{\eta} \left(\sqrt{\sigma_d^2 + \sigma_q^2/K^2} + \frac{1}{2} \right) = \frac{1}{\eta} \left(\frac{\sigma_{y.\mathrm{dark}}}{K} + \frac{1}{2} \right).
\tag{5.16}
$$

By inserting the camera characteristics measured in the blue wavelengths area and the variance of the measured dark-signal $\sigma_{y.\mathrm{dark}} = 241\,[\mathrm{DN}]$, this threshold is given by $\mu_{p.\mathrm{min}} = 20\,[\mathrm{photons}]$.

By using these thresholds, the dynamic range of the sensor array can be computed as follows:

$$
\mathrm{DR} = \frac{\mu_{p.\mathrm{sat}}}{\mu_{p.\mathrm{min}}} = 574.
\tag{5.17}
$$

The consequences that arise from these values for the precision of the bPSV technique are described in Chapter 6.

5.1.4 Linearity Analysis

Since the bPSV technique presented in this work crucially depends on a precise measurement of absolute gray-values and of their ratios, non-linearities in the response of the imaging-sensor present one of the main sources of error.

The following analysis was made for the blue LED-illumination because the signals recorded in the course of this study are all from the blue and violet range of the spectrum. The range in between which a linear response of the imaging-device is expected, lies between the absolute sensitivity threshold (cyan colored line in the SNR-plot)

$$\mu_p(\text{SNR} = 1) = \mu_{p.\text{min}} \approx \frac{1}{\eta}\left(\sqrt{\sigma_d^2 + \sigma_q^2 K^{-2}} + \frac{1}{2}\right) = \frac{1}{\eta}\left(\frac{\sigma_{y.\text{dark}}}{K} + \frac{1}{2}\right) \tag{5.18}$$

and the saturation capacity of a single pixel

$$\mu_{e.\text{sat}} = \eta\mu_{p.\text{sat}}. \tag{5.19}$$

To analyze the degree of linearity, a linear function was fitted to the curve of the photon induced gray-values. For the computation of the fit-parameter, we restricted the fit to a range between 5 % and 95 % of the saturation capacity value. As shown in Figure 5.5 on page 82 the assumption is valid that the sensor shows a linear response between the SNR-threshold and the saturation range. The error that is introduced by this assumption can be estimated to be less than 1 % (cf. Figure 5.5 on page 82).

5.1.5 Spatial Non-Uniformities

During the calibration spatial non-uniformities of the sensor response were measured in three wavelength areas {red, green ,blue}. In these measurements the sensor array was illuminated directly (i.e. without any optics in front of it) with different wavelengths and various intensities. Due to the Ulbricht sphere, the light field that irradiates the sensor can be assumed to be highly homogeneous over the whole sensor surface.

In literature spatial artifacts that can be observed in the sensor signal are often referred to as *Fixed Pattern Noise* (FPS). This expression is not perfectly correct since the observed imperfection is not a noise that varies the signal in time. Therefore, the authors of the EMVA1288 standard introduced a novel nomenclature. It distinguishes two spatial imperfections in the signal of a sensor array, i.e. *Dark Signal Non-Uniformities* (DNSU) and *Photo Response Non-Uniformities* (PRNU).
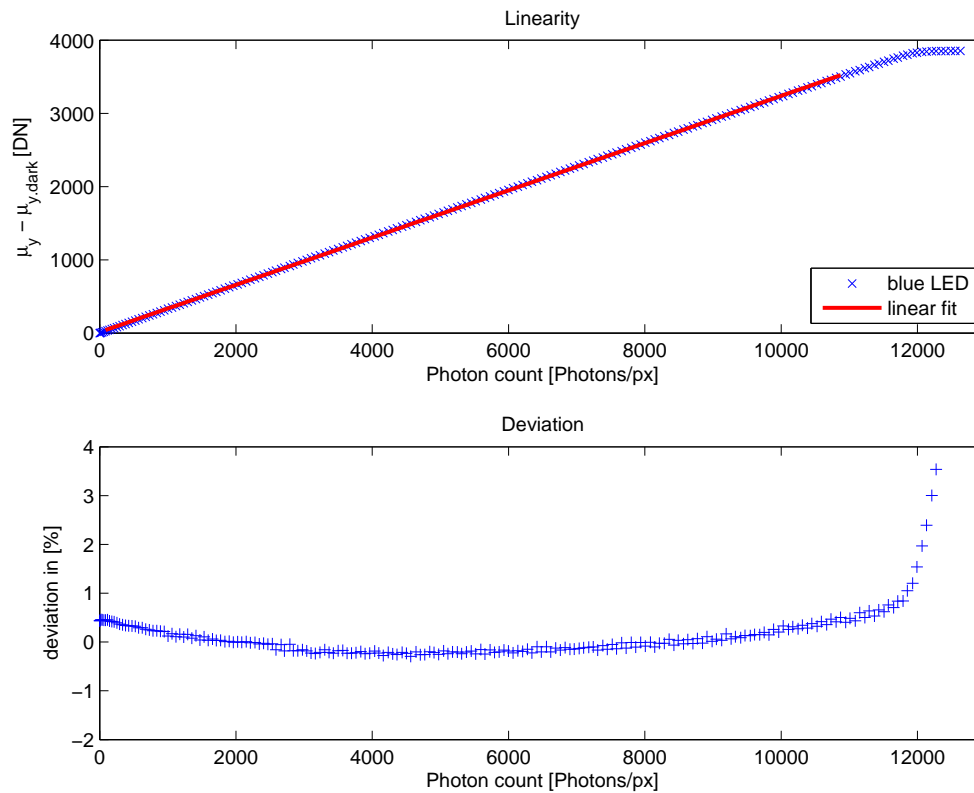
Figure 5.5: Linearity analysis of the sensor array. The upper plot shows the gray-value signal as a function of the irradiance. A linear fit was applied to a range between 5 % and 95 % of the saturation capacity (red line). The lower plot shows the deviation of the measured gray-values from the linear model. Within the range of the fit, the error is below 1 %.

Dark Signal Non-Uniformity (DSNU): This spatial non-uniformity of the pixel-response occurs in the dark-signal. It is independent of the incident light that hits the sensor array. In the calibration this characteristic is extracted from dark-measurements.

Photo Response Non-Uniformity (PRNU) This characteristic describes a spatial non-uniformity of the pixel response. It is estimated from an image taken at a medium intensity of the incident light field.

The image in Figure 5.6 on page 84 shows the PRNU-characteristic of the sensor array measured with blue light of medium intensity. It has to be pointed out that the contrast in this image is increased by several orders of magnitude.
The PRNU measurements show a set of disk-patterns that remind of refraction artifacts caused by dirt on a lens.
We assume that these PRNUs originate from imperfections in the manufacturing process of the array. Here two scenarios are likely:

- Imperfections during the application of a coating on the sensor array might have caused an inhomogeneous distributed sensor behavior.

- Dirt on the optics that were used in the lithographic manufacturing of the array can result in a spatial non-uniformity of the sensor characteristics.

Additionally to this disk-pattern, the measurements of the DSNU show a different variance behavior of the upper and the lower half of the sensor. In contrast to the disk-pattern, this non-uniformity is also present in variance of the PRNU-signal. An image of this DSNU-characteristic is shown in the appendix of this thesis (cf. Figure A.3 on page 163). The most likely reasons for this different behavior of the upper and the lower half of the sensor array are the different readout and amplification pathways within the sensor electronic.

For a quantitative characterization, the EMVA1288 standard defines two measures that are computed by equations which are equivalent to the equations used for the computation of the temporal noise.
For a dark-signal y_{dark} and a signal that was recorded at an approx. $50\,\%$ saturation of the image signal y_{50}, both given by $M \times N$ images, the mean signal can be computed as follows:

$$\mu_{y.\mathrm{dark}} \quad = \quad \frac{1}{MN} \sum_{m=0}^{M-1} \sum_{n=0}^{N-1} y_{\mathrm{dark}}[m][n] \tag{5.20}$$

$$\mu_{y.50} \quad = \quad \frac{1}{MN} \sum_{m=0}^{M-1} \sum_{n=0}^{N-1} y_{50}[m][n] \tag{5.21}$$

NonUniformities – Mean (blue LED=100)

Figure 5.6: Spatial non-uniformity of the linear response of the sensor array. In this measurement the naked sensor array was illuminated with a highly homogeneous light field. The contrast of this image was increased by several orders of magnitude for a proper visualization of these effects.
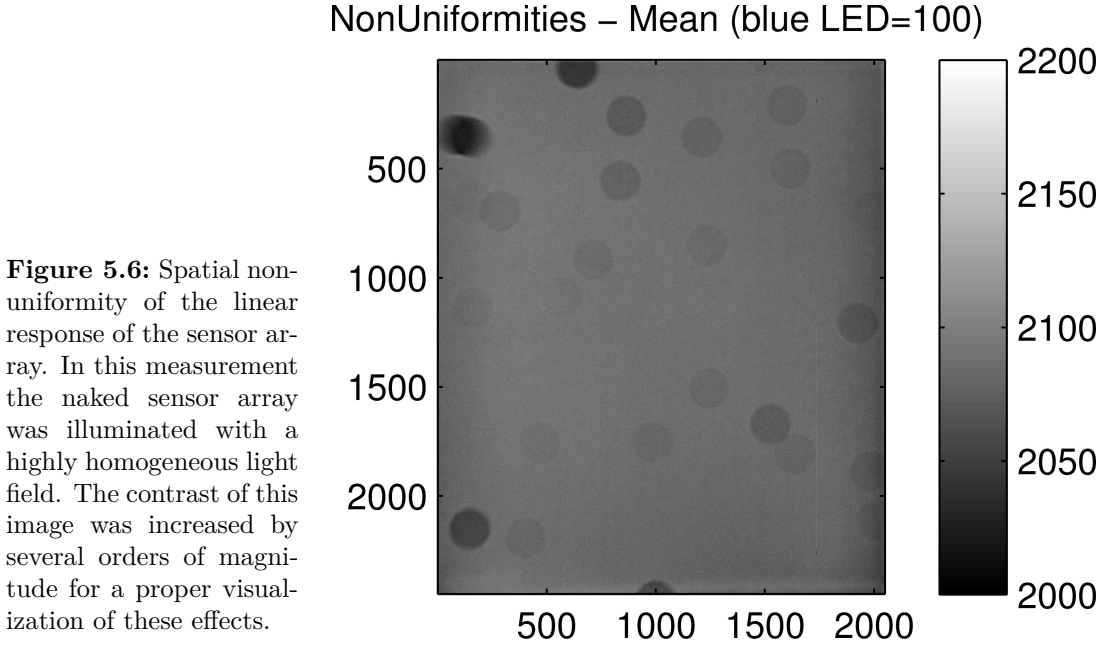
Using these mean values, the spatial variances s^2 of both images can be computed straightforward.

$$s_{y.\mathrm{dark}}^2 \quad = \quad \frac{1}{MN-1} \sum_{m=0}^{M-1} \sum_{n=0}^{N-1} \left(y_{\mathrm{dark}}[m][n] - \mu_{y.\mathrm{dark}}\right)^2 \tag{5.22}$$

$$s_{y.50}^2 \quad = \quad \frac{1}{MN-1} \sum_{m=0}^{M-1} \sum_{n=0}^{N-1} \left(y_{50}[m][n] - \mu_{y.50}\right)^2 \tag{5.23}$$

On the basis of the mean pixel value and the spatial variance s^2 of the dark image and the 50 % saturation image, the EMVA1288 standard defines two characteristic parameters DSNU_{1288} and PRNU_{1288} of an imaging sensor array as follows:

$$\mathrm{DSNU}_{1288} \quad = \quad \frac{s_{y.\mathrm{dark}}}{K} \; [\mathrm{e}^-] \tag{5.24}$$

$$\mathrm{PRNU}_{1288} \quad = \quad \frac{\sqrt{s_{y.50}^2 - s_{y.\mathrm{dark}}^2}}{\mu_{y.50} - \mu_{y.\mathrm{dark}}} \cdot 100\,\% \tag{5.25}$$

The resulting characterization parameter for the spatial non-uniformities of the dark-signal and the image that was acquired with approx. 50 % pixel-saturation, are summarized in Table 5.2.

Color	$\mu_{y.\mathrm{dark}}[\mathrm{DN}]$	$\mu_{y.50}[\mathrm{DN}]$	$s^2_{y.\mathrm{dark}}[\mathrm{DN}^2]$	$s^2_{y.50}[\mathrm{DN}^2]$	$\mathrm{DSNU}[\mathrm{e}^-]$	$\mathrm{PRNU}[\%]$
red	246.3	1116.4	38.7	596.5	61	2.71
green	244.8	1356.5	38.7	724.2	61	2.36
blue	246.2	2062.5	38.4	1154.1	60	1.84

Table 5.2: Summary of the non-uniformity characterization according to the *European Machine Vision Association* (EMVA)1288 standard

Correction of the PRNU-effect For the correction of the PRNU-effect in the sensor arrays response, an $M \times N$ correction image C was computed to correct this error source in a simple pixel-wise multiplication with the raw-image.

Therefore, the relative deviation from the mean gray-value in the non-uniformity image for the blue wavelength area was computed.

The elements of the correction image are therefore given by:

$$C[m][n] = \frac{\mu_{y.50} - \mu_{y.\mathrm{dark}}}{y_{50}[m][n] - y_{\mathrm{dark}}[m][n]} \tag{5.26}$$

All data that were recorded to characterize the non-uniform linearity of the sensor array are shown in the appendix chapter of this thesis (Figure A.3 on page 163).

5.2 Step II: Feature Extraction

The image processing operations that were used to extract the particle streaks in all PSV measurements and to compute the course of depth and velocity along the center-line of each streak can be divided, as shown in Figure 5.1 on page 74, into 5 steps. These steps also determine the outline of this section.

5.2.1 Removal of Lens Flare Effects and Background Subtraction

Unfortunately, in all measurements that were done during this study we observed some lens flare effects and slight reflections from the water surface. These artifacts are caused by the extreme bright LED-illumination and need to be corrected to enable the extraction of the pure particle signal by means of an extraction algorithm that is described in the following sections. For the removal of these artifacts a local adaptive background removal strategy based on a temporal median filter was implemented.

The first assumption that is made in this context is that all pixel which do not contain the signal of a passing particle contain only a superposition of sensor noise from the

camera and the above mentioned illumination artifacts.

For all pixel that contain a signal from a passing particle, we assume that sensor noise, illumination artifacts and particle signal add up and result in the gray-value measured by the pixel. Therefore, a correction routine only needs to compute the pure superimposed illumination-artifact image and subtract it from each measured streak image. In addition, we assume that the probability of a pixel to contain the signal of a passing particle is lower than 49 %.

In general, background estimation routines are used in many applications in the field of image processing. The most prominent examples are algorithms for detecting moving objects that were imaged by static cameras (Piccardi, 2004). The general understanding of a perfect background image is that it shows the static scene behind (probably moving) objects. Piccardi (2004) points out that this background image has to be updated when it comes to changes of the static scene or changes in the illumination. Since in all measurements that were done in this study, an absorbing dye was mixed into the liquid, we do not expect to observe any background signal at all.

Nonetheless, we can make use of a background estimation routine to compute the illumination-artifact signal. The temporal median filter used in this study can be described as follows.

Given an image-stack with N measured images $\tilde{\mathbf{I}}_k$, $\{k \in \mathbb{N}|0 \le k < N\}$ containing $X \times Y$ pixels, for each pixel $\tilde{\mathbf{I}}_k(i,j)$, $\{i, j \in \mathbb{N}|0 \le i < X - 1 \text{ and } 0 \le j < Y\}$ a ring buffer of size $c \in \mathbb{N}$ with $c \le N$ is initialized. For an arbitrary image $\tilde{\mathbf{I}}_k(i,j)$ with $k \ge c$, the superimposed lens-artifact signal $\mathbf{B}_k(i,j)$ is given by the temporal median that is computed pixel-wise from the c precedent images.

$$\mathbf{B}_k(i,j) = \text{median}\{\tilde{\mathbf{I}}_l(i,j)|\,(k-c) < l \le k\} \tag{5.27}$$

Since the lens-artifact signal superimposes the complete image, a correction can be achieved by subtracting the signal from the original image.

$$\mathbf{I}_k(i,j) = \tilde{\mathbf{I}}_k(i,j) - \mathbf{B}_k(i,j) \tag{5.28}$$

The number of images that contribute to the median is controlled by the parameter c in (5.27). For a background signal that changes rapidly in time, this parameter can be decreased to adapt the background estimation. Increasing the size of the temporal median filter c means to increment the number of images that contribute to the background estimation, and therefore increases the robustness of the estimate (Piccardi, 2004; Vikas et al., 2010).

For the measurements that were recorded within the scope of this thesis, the conditions were rather static, i.e. a flat water surface and a constant optical axis.

As a result, the illumination-artifacts can be treated like a static signal that superimposes all measurements in a bPSV image-sequence.
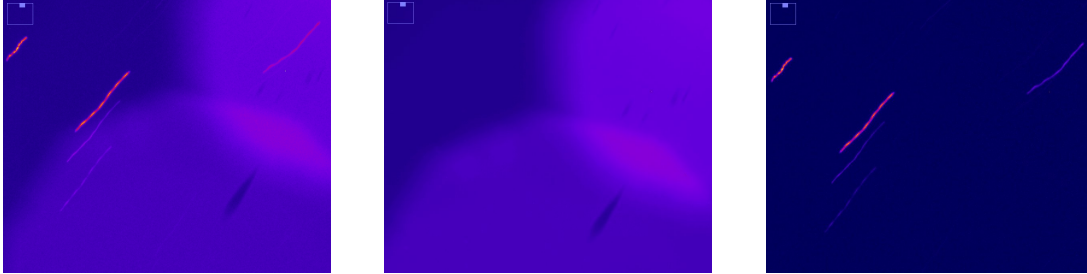
Figure 5.7: Illustration of the lens flare removal using a temporal median filter. The *left* image shows a section of an original bPSV-measurement $\mathbf{I}_k$. The image can be seen as a superposition of the lens effect and the particle streak signals. The image in the *middle* shows the result of the temporal median computation according to (5.27) over the whole image stack. The *right* image is the result of the lens flare effect correction $\mathbf{I}$ using the median based background subtraction.

To speed up computation, we modified the background estimation for the static case by computing the temporal median for each pixel considering all images from a sequence. The result is a single background image that can be subtracted from all images in the sequence.

The process is also illustrated in Figure 5.7 for a small image section of a bPSV-measurement. The image on the left shows a section of a single image from a bPSV-measurement series $\tilde{\mathbf{I}}_k$. It contains a superposition of the measured streak structures and the previously described lens-artifact signal. The image in the middle of Figure 5.7 shows the extracted interfering signal $\mathbf{B}_k$ that was extracted from the complete image stack using the temporal median filter described in (5.27). The right image shows the corrected signal $\mathbf{I}_k$ computed using (5.28).

For the computation of the medians we made use of the `partial_sort` function to sort `vector<double>` vectors containing the gray-values of the pixel position from all images of a sequence. The pixel-wise median computation and the subtraction of the illumination-artifact image was parallelized using the *portable shared memory parallel programming* library `openMP` (Chapman et al., 2007).

5.2.2 Tensor Based Feature Extraction

The next step in the feature extraction workflow is the computation of a set of tensor-based low-level features (e.g. edges, gradients or junctions) that are computed from the corrected images. These image features enable a robust extraction of the streak-structures, of their center-lines and of the intensity course along these lines.
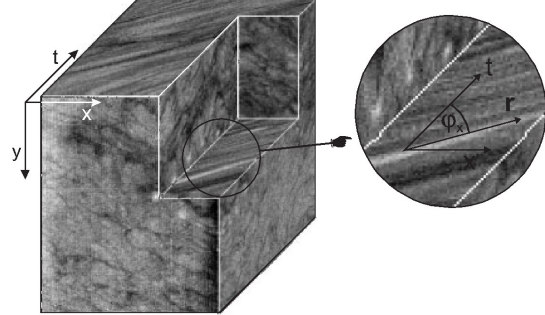
Figure 5.8: Graphical illustration of the functional principle of the *three-dimensional* (3d) *structure tensor* by Haußecker et al. (1998).

In the field of image processing many tensor-based approaches were developed to extract structures and their orientation from image data. The main idea of most tensor-based methods is to formulate a rotational invariant operator that allows the extraction of specific local features from an image.

Originally the application of tensor-based methods on simple gray-value image-sequences was developed for the optical-flow estimation. Later applications mainly use tensor-based approaches for the computation of local image features which are invariant under Eulerian transformations.

Structure Tensor

A given gray-value image sequence $\mathbf{I}(x, y, t)$ can be seen as a 3d data cube. As visualized in Figure 5.8, the computation of an optical-flow field from this sequence is equivalent to the estimation of *iso-gray-value lines* within small spatiotemporal neighborhoods in the volume. Therefore, one has to search for the local direction $\vec{r} = (r_1, r_2, r_3)$ with the best accordance to all gradients $\nabla \mathbf{I}$ in the local neighborhood. Haußecker et al. (1998) proposed the use of a first order gradient tensor for the solution of the optical-flow problem. He claimed that the problem of estimating iso-gray-value lines can be solved by minimizing the following matrix equation.

$$\operatorname*{argmin}_{\vec{r}} \left(\vec{r}^T \mathcal{J} \vec{r} \right) \parallel \vec{r} \parallel_2 = 1 \tag{5.29}$$

Here the 3d *structure tensor* is defined to be

$$\mathcal{J} = \begin{pmatrix} \langle \frac{\partial \mathbf{I}}{\partial x} \frac{\partial \mathbf{I}}{\partial x} \rangle & \langle \frac{\partial \mathbf{I}}{\partial x} \frac{\partial \mathbf{I}}{\partial y} \rangle & \langle \frac{\partial \mathbf{I}}{\partial x} \frac{\partial \mathbf{I}}{\partial t} \rangle \\ \langle \frac{\partial \mathbf{I}}{\partial y} \frac{\partial \mathbf{I}}{\partial x} \rangle & \langle \frac{\partial \mathbf{I}}{\partial y} \frac{\partial \mathbf{I}}{\partial y} \rangle & \langle \frac{\partial \mathbf{I}}{\partial y} \frac{\partial \mathbf{I}}{\partial t} \rangle \\ \langle \frac{\partial \mathbf{I}}{\partial t} \frac{\partial \mathbf{I}}{\partial x} \rangle & \langle \frac{\partial \mathbf{I}}{\partial t} \frac{\partial \mathbf{I}}{\partial y} \rangle & \langle \frac{\partial \mathbf{I}}{\partial t} \frac{\partial \mathbf{I}}{\partial t} \rangle \end{pmatrix} \tag{5.30}$$

where each component can be written in its integral form

$$\mathcal{J}_{pq} = \langle \frac{\partial \mathbf{I}}{\partial p} \frac{\partial \mathbf{I}}{\partial q} \rangle = \int_{-\infty}^{\infty} h \left(\vec{x} - \vec{x}' \right) \frac{\partial \mathbf{I}}{\partial p} \frac{\partial \mathbf{I}}{\partial q} \, \mathrm{d}x'. \tag{5.31}$$

In this equation, $h(\vec{x} - \vec{x}')$ is a function that defines the local neighborhood around $\vec{x}$. Usually a Gaussian window function is used for this purpose. By adjusting the area of influence defined by this function, it is possible to define a scale for the structures that can be analyzed by the *structure tensor*.

It can be proved by using Lagrangian multiplicators that the minimum of (5.29) is given by the eigenvector of $\mathcal{J}$ that corresponds to the smallest eigenvalue (Haußecker et al., 1998).

In the field of image processing the pure spatial version of the *structure tensor*

$$\mathcal{S} = \begin{pmatrix} \langle \frac{\partial \mathbf{I}(x,y)}{\partial x} \frac{\partial \mathbf{I}(x,y)}{\partial x} \rangle & \langle \frac{\partial \mathbf{I}(x,y)}{\partial x} \frac{\partial \mathbf{I}(x,y)}{\partial y} \rangle \\ \langle \frac{\partial \mathbf{I}(x,y)}{\partial y} \frac{\partial \mathbf{I}(x,y)}{\partial x} \rangle & \langle \frac{\partial \mathbf{I}(x,y)}{\partial y} \frac{\partial \mathbf{I}(x,y)}{\partial y} \rangle \end{pmatrix} \tag{5.32}$$

is often used to compute local structure-based image features that are invariant against all kinds of Eulerian transformations. The most common image features that can be exploited from the two-dimensional *structure tensor* are the local orientation that can be obtained from the orientation of the eigenvector corresponding to the smallest eigenvalue and a measure of the strength of the local structure based on the relation between both eigenvalues.

One of the major drawbacks of the *structure tensor* is that the nearby image features (e.g. edges and corners of small objects) are blended into a single response and can not be resolved separately. Another shortcoming is its different response to lines and edges. This is because the structure tensor is not phase-invariant because of its gradient based definition (cf. (5.32)). As a result of these restrictions, the performance of the structure tensor at the end of the recorded streak structures is worse compared to the response of the *boundary tensor* that will be introduced in the following section.

Boundary Tensor

The second order *boundary tensor* turned out to be a superior method for the low-level feature extraction in our case. As described by Köthe (2006), it overcomes all previously mentioned shortcomings of the *structure tensor*. This tensor is defined in (Köthe and Felsberg, 2005) by means of the sum of a first and a second order band-pass Riesz transform (Felsberg and Sommer, 2001) $\mathbf{b}$ and $\mathbf{A}$ of an image.

$$\mathcal{B} = \begin{pmatrix} b_{11} & b_{12} \\ b_{21} & b_{22} \end{pmatrix} = \mathbf{b}\mathbf{b}^T + \mathbf{A}\mathbf{A}^T \tag{5.33}$$

In the implementation, the tensor-scale $\sigma_{\mathcal{B}}$ is the only parameter that controls the *boundary tensor*. More precisely spoken, $\sigma_{\mathcal{B}}$ controls the size of the band-pass filter that is part of the tensor. By adjusting the tensor-scale, the size of structures that

cause a response of the tensor can be controlled. For all data recorded in the course of this thesis, a tensor scale between $\sigma_{\mathcal{B}} = 5$ and $\sigma_{\mathcal{B}} = 8$ yielded the strongest tensor response for the recorded streak structures.

From this tensor one can easily extract several energies that will be used as feature-images in the next steps of the workflow. The definition of the first energy is based on the observation that both second order band-pass Riesz transforms (**b** and **A**) are real. Therefore, $\mathcal{B}$ has to be always positive semi-definite. For this reason the trace of this tensor represents a local energy measure called *boundary energy*.

This energy can be divided into a fraction caused by junctions in the data $E_{junction}$ and a part that represents the tensor response to edges E_{edge}.

$$E_{boundary} = E_{junction} + E_{edge} = \operatorname{tr}(\mathcal{B}) = b_{11} + b_{22}. \tag{5.34}$$

Using the expression for the *edge energy*

$$E_{edge} = \sqrt{(2b_{12})^2 + (b_{11} - b_{22})^2}, \tag{5.35}$$

the *junction energy* can be computed by subtracting the edge energy from the boundary energy. Additionally, a fourth low-level image-feature called *local orientation θ* can be derived from the boundary tensor using:

$$\theta = \frac{1}{2}\arctan\left(\frac{2b_{12}}{b_{11} - b_{22}}\right) \tag{5.36}$$

This feature is visualized with black arrows in Figure 5.10 on page 94 for an image section that shows the measured gray-value distribution of a particle streak.

On the basis of these low-level image features, the boundary tensor can be used to detect edges, lines and corners from the local distribution of the energies in the feature images.

The particle streak extraction framework that is presented in this thesis makes use of the local *boundary energy $E_{boundary}$* computed by means of a *boundary tensor* with $\sigma_{\mathcal{B}} = 7$. Since the sum of *edge energy* and *junction energy* is a decent indicator for the presence of particle streak structures, the *boundary energy* is used to identify particle streak structures in the corrected bPSV-measurements. In an iterative center-line extraction routine that is described in detail in the following section, the *local orientation θ* is used for a stepwise iteration along the structures.

For the computation of the *boundary tensor* and the low-level feature-images that are based on its components, the `c++` open-source image processing library `vigra` (Köthe, 2000) was used.

For a more detailed description of the *boundary tensor* and a characterization of its edge and boundary detection abilities, we refer to (Köthe and Felsberg, 2005; Köthe, 2006).

Based on the previously described features an extraction routine was developed to detect particle streak structures in single images of the PSV image sequences.
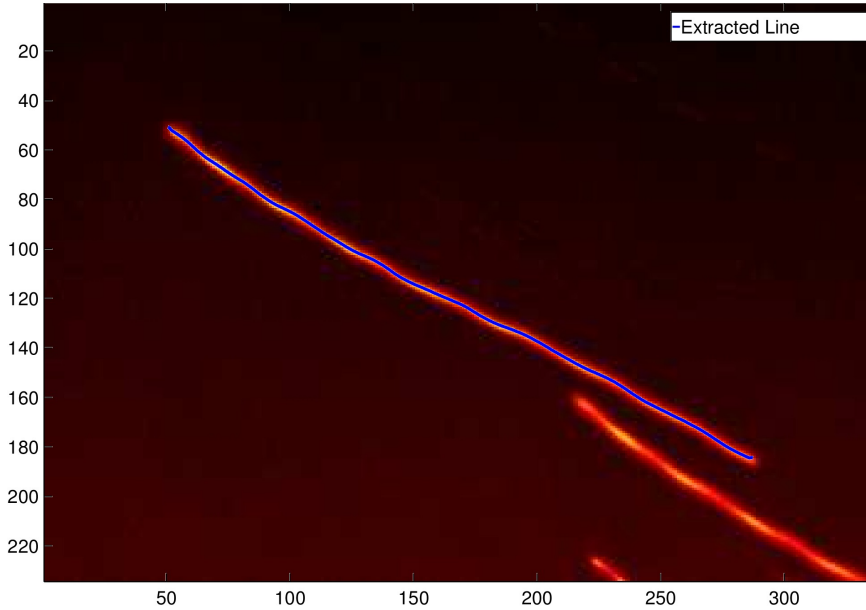
Figure 5.9: Zoomed pseudo-color image of a single streak measured with an exposure time of $t_{exp} = 1\,\text{s}$ and an illumination frequency $F = 8\,\text{Hz}$. The blue line shows the course of the center-line that was extracted by the previously described algorithm.

5.2.3 Streak Detection

All quantitative PSV and *Particle Tracking Velocimetry* (PTV) approaches that were published in the past use threshold-based image segmentation techniques to estimate the positions of particle streaks in the PSV-images.

All extracted information about the particle movement, i.e. the direction and the velocity, are based on this segmentation result (cf. Section 2.2.2). Most approaches make no use of the information that is contained in the gray-value distribution within the segmented area and all state-of-the-art approaches ignore the information of neighboring pixels that are below the threshold.

One of the aims focused during the development phase of this method was to make use of the complete gray-value signal caused by a passing particle on the bPSV-image. Therefore, the detection algorithm developed in the course of this thesis uses a completely different strategy. Based on the particle streak model that is proposed in Section 3.1, this method uses an iterative extraction approach that starts at several seeding-points. These seeding-points are given by a set of local maxima in the *boundary energy* feature image $E_{boundary}$. From each seeding point the extraction algorithm travels along the streak in both directions. Given the assumption that the intensity profile along a line that is perpendicular to the streak structure can be described by a Gaussian bell-curve, the extraction routine computes the exact center-line and

the intensity course using a non-linear *Levenberg-Marquardt* (LM) fit. This strategy was inspired by the strategy used in all sub-pixel precise PTV-methods where a *two-dimensional* (2d) Gaussian bell-curve is fitted to the intensity distributions caused by single particles in the measurements (Nobach et al., 2005).

Center-line Extraction

As described in detail in the particle streak model introduced in Section 3.1, the gray-value distribution of a streak structure caused by a passing particle in a bPSV-measurement can be described by a temporal integral over a two-dimensional Gaussian bell-curve that is moved along a trajectory in the image space. As a consequence, we expect the intensity distribution on a line that is perpendicular to the streak structure (i.e. perpendicular to the *local orientation θ*) to be a one-dimensional Gaussian bell-curve.

Figure 5.10 on page 94 shows an image section that contains the gray-value distribution of particle streak; the local orientation is displayed in form of arrows within the pixels, and the Gaussian bell-curves that were fitted perpendicular to the *local orientation* by means of a LM-fit are plotted in green.

The center-line extraction routine consists of two loops that are explained in detail in the pseudo-code on page 93. The outer loop starts at the local maximum of the *boundary energy*. In each iteration the inner loop is initialized to compute the middle-line of the streak pattern that belongs to this maximum. Afterwards the next lower local maximum is chosen.

The inner loop uses the local orientation and the gray-value information from the measurement. It starts at the local maximum that was given by the outer loop. At this position, which is only pixel-precise, the inner loop corrects the center-line positions to sub-pixel precision by means of a LM-fit of a Gaussian bell-curve on the gray-values that lie on a line which is perpendicular to the *local orientation θ*. These perpendicular LM-fits are visualized by green areas in Figure 5.10 on page 94.
Afterwards, the algorithm updates the current position by traveling one step (the step size can be set in the parametrization file) into the direction of θ. These steps are repeated until the result of the LM-fit describes a Gaussian bell-curve with a width σ that is above a certain threshold. Normally, this termination criterion is fulfilled when the loop arrives at the end of the structure.

In order to extract the complete streak, the algorithm resets the current positions to the point where the inner loop was initialized and starts traveling against the *local orientation*, i.e. along the streak in reverse direction, until it reaches the second end.

The sub-pixel precise position of the center-line and the result of the LM-fit are stored in a feature vector for each streak. The extracted center-line positions are shown as a blue line in Figure 5.10 on page 94.

Pseudo-code of the line extraction algorithm

1. Compute all local maxima in the *boundary energy* feature-image and sort them in a descending order

2. **For all** local maxima *boundary energy*

   a) Extract the gray-value information from the bPSV-image on a line perpendicular to the *local orientation* (red line in Figure 5.10)

   b) Use a non-linear LM-fit to extract the parameter of a Gaussian bell-curve that describes extracted gray-value distribution

   c) Sub-pixel precise correction of the center-line position

   d) Store all parameters in the feature-vector corresponding to this streak

   e) Move the current position one step size into the direction of the *local orientation*

   f) **If** the width σ of the Gaussian bell-curve is larger than a predefined threshold,
   then: go back to the initial position, reverse the *local orientation* and got to 2.g)
   else: move the current position one step size into the direction of the local orientation and **go to** 2.a)

   g) Use a non-linear LM fit to extract the parameter of a Gaussian bell-curve that describes extracted gray value distribution

   h) Sub-pixel precise correction of the center-line position

   i) Store all parameters in the feature-vector corresponding to this streak

   j) **If** the width σ of the Gaussian bell-curve is larger than a predefined threshold,
   then: disable all local maxima that lie in the direct neighborhood of the extracted center-line, go to the next lower enabled local maximum of the *boundary energy* and start again from 2.a)
   else: go to 2.g)

The result of this center-line extraction algorithm is a set of streak feature-vectors that contain spatial information about the particle positions during the exposure time by means of their center-lines. In addition, the feature-vectors comprise information about the gray-value course along the center-line on the basis of the maxima of the fitted Gaussian bell-curves. It has to be pointed out that this information is more precise and robust with respect to image noise than taking the maximum-pixel gray-value since the whole information on all intensities of the perpendicular lines is taken into account.
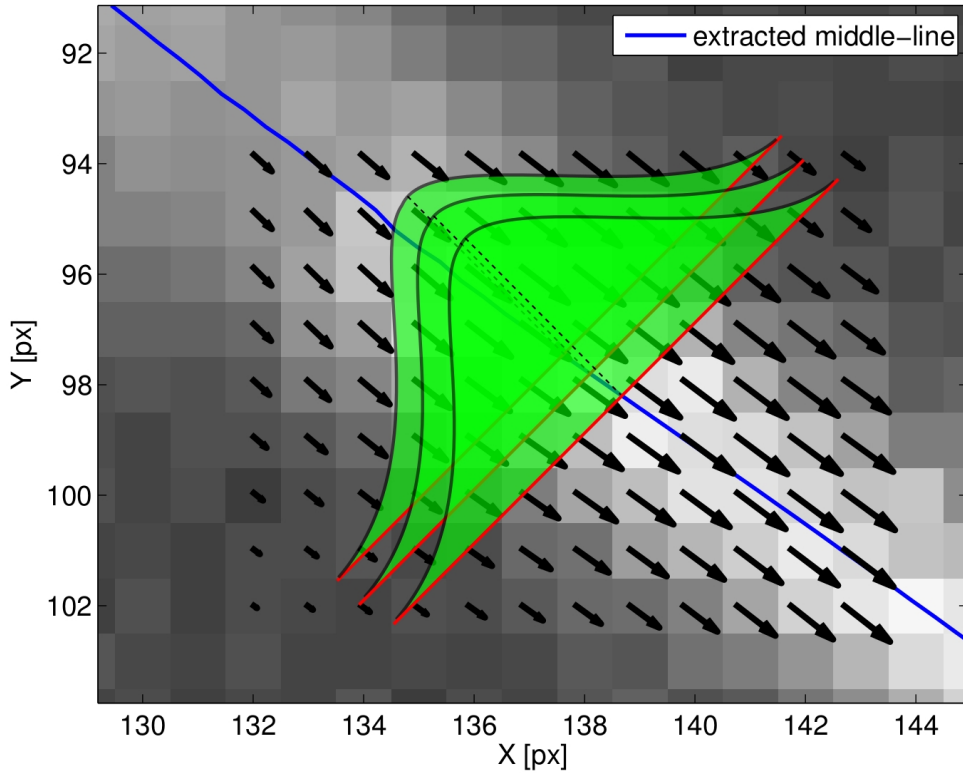
Figure 5.10: Graphic to illustrate the steps of the center-line extraction algorithm. In the background the measured gray-values are shown; the arrows on top show the direction of the extracted local orientation ϕ. Gaussian bell-curves (green) are fitted perpendicular to ϕ for the extraction of the particle streak width and intensity (Voss et al., 2012).

Additionally to these streak properties the *local orientation* and the streak-width are also stored in the streak feature-vectors for all positions on the center-line.

5.2.4 Velocity Estimation

The main objective of the velocity estimation routine described in this subsection is the reconstruction of the particle velocity-information that was lost in the temporal integration over the exposure time t_{exp} (cf.: Section 3.1). As described in detail in Chapter 3, the instantaneous spatial frequency of the gray-value signal along the center-line of a streak-structure can be used to compute the horizontal velocity course $v_h(c)$ of the particle that caused the streak on the basis of the following relation.

$$v(c) = \alpha \frac{F}{f(c)} \tag{5.37}$$

Where c [px] is given by the position on the center-line, α [cm/px] is the pixel-size, F [Hz] is the illumination modulation frequency and $f(c)$ [1/px] stands for the instantaneous spatial frequency of the gray-value signal.

In order to compute the frequency of the gray-value signal $G(c)$ that was extracted along the center-line of each streak, a *Hilbert Huang Transform* (HHT) was implemented. This transformation is a combination of an *Empirical-Mode-Decomposition* (EMD) and a *Hilbert Transform* (HT). The result of the HHT is a spatial *analytical signal* as defined in (3.23). This signal enables the computation of the *instantaneous frequency $f(c)$* of a given signal and its *instantaneous amplitude $a(c)$* by means of the equations (3.25) and (3.26). A more theoretical description and a literature review of these methods is given in Chapter 3 of this thesis.

Empirical-Mode-Decomposition (EMD)

In the *Hilbert Huang Transform* (HHT) the EMD is used as a signal preprocessing step that decomposes the signal into a set of independent intrinsic mode functions (IMF)s, which can be analyzed separately in the following HT. By definition, valid *intrinsic mode function* (IMF) fulfills the following two requirements:

1. The difference between the number of extrema and the number of zero-crossings that are contained in a valid IMF must be less than or equal to one.

2. At any point on a valid IMF, the local mean value defined by the mean of two envelope functions has to be equal to zero.

The implemented EMD algorithm uses an iterative sifting scheme for the extraction of the IMFs from a signal $G(x)$. To illustrate the general idea of this decomposition, a pseudo-code of the implementation is given on page 96.
In the first step the counter variables are set to zero, and the rest r_0 is initialized by means of the signal $G(x)$ itself. In the next step the current mode h_{ij} is set to be the remaining rest r_i from the previous iteration. The following loop is repeated until the rest signal is monotone, i.e. does not contain any periodical information.
The inner loop updates the current mode as long as it fulfills all requirements of an IMF. For each update two spline-functions are fitted through the maxima and minima of the current mode. The point-wise mean of these splines, i.e. the local mean, is afterwards subtracted from the current mode.
When the end of the inner loop is reached, i.e. h_{ij} fulfills the requirements of an IMF, it is stored in c_i. Afterwards the rest r_i is updated by $r_{i+1} = r_i - c_i$. After termination the list c_i stores the IMFs and the non-periodical rest is given by r_n.

Pseudo-code of the *Empirical-Mode-Decomposition* (EMD)

1. initialize $r_0 = G(c)$, $i = 0$ and $j = 0$
2. set $h_{ij} = r_i$
3. **While:** r_i is not monotone
   a) **While:** h_{ij} is no IMF
      i. identify all local minima and local maxima
      ii. fit two cubic splines; One through all minima and one through all maxima
      iii. compute the mean of these two splines to be the local mean signal m_{ij}
      iv. $h_{i(j+1)} = h_{ij} - m_{ij}$
      v. $j = j + 1$
   b) $c_i = h_{ij}$
   c) $r_{i+1} = r - h_{ij}$
   d) $i = i + 1$
4. return the computed IMFs in c and the residual r_n

Since we expect the signal measured in the PSV measurements to contain a non-periodical offset, a periodical mode and some noise, the gray-value signal $G(c)$ is decomposed in three modes. The first mode is the dominant *intrinsic mode function* (IMF) that corresponds to the reflected intensity modulated illumination. The second mode is a high frequent IMF that comprises image noise and variations caused by numerical artifacts in the LM fit of the center-line extraction algorithm. In the last mode the non-periodical offset signal is comprised.

For the following frequency analysis that was developed for an estimation of the instantaneous frequency and amplitude of the spatial gray-value modulation along the center-line of the particle streak structures, the non-periodic offset and the image noise are not taken into account. Therefore, the *Hilbert Transform* (HT) focuses on the analysis of the dominant IMF that is from now on labeled as $X(c)$

Hilbert Transform (HT)

For the computation of a HT from the periodical component that was extracted by means of the EMD, we defined a discrete HT filter on the basis of a Hamming window function (Harris, 1978).
For a given size N, this discrete window function $w(n) : \mathbb{N} \to \mathbb{R}$ is defined by

$$w(n) = \alpha_h + (1 - \alpha_h) \cos\left(\frac{2\pi}{N} n\right). \tag{5.38}$$
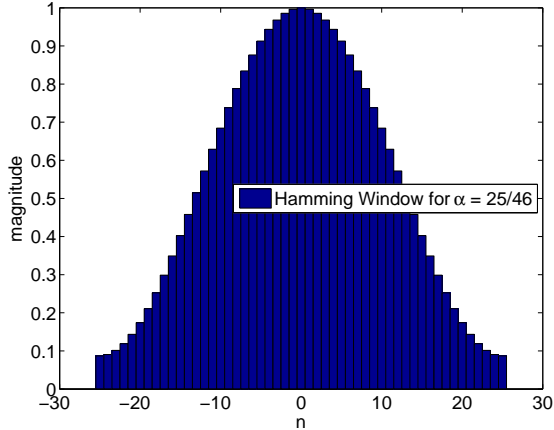
Figure 5.11: Output of the Hamming Window function of size $N = 50$ with an optimal $\alpha_h = 25/46$

The window function coefficient α_h of the filter used in this study was chosen to be the optimum $\alpha_h = \frac{25}{46}$ proposed by Harris (1978). A filter output for $N = 50$ is shown in Figure 5.11.

The complex signal $Y(c)$ defines the *analytic signal $Z(c)$* corresponding to the periodical input signal. This signal is computed in a one dimensional convolution of the signal vector $X(c)$ with the product of window function and the Hilbert kernel $H = \frac{1}{\pi c}$ as described in Chapter 3.

$$Y(x) = \mathcal{H}_t \left(X\left(c\right)\right) = X(c) \star \left(wH^T \right) \tag{5.39}$$

Here $\mathcal{H}_t$ symbolizes the application of the HT. For this computation the window function w and the Hilbert kernel H must have the same dimensionality. The '$\star$' symbolizes a line convolution. In the implementation, we made use of the `convolve_line` function implemented in the open-source image processing library `vigra` (Köthe, 2000).

For the computation of the signal amplitude $a(c)$ and its phasing $\phi(c)$, we made use of the polar representation of the analytical signal (3.23). This signal representation allows the derivation of an instantaneous frequency that is computed element-wise from the gray-value signal $X(c)$ itself and from its complex counterpart $Y(c)$, using (3.25).

The spatial frequency of the gray-value signal is given by the change of the phasing signal $\phi(c)$. Therefore, the frequency feature vector $f(c)$ was computed in a convolution of $\phi(c)$ with a simple one-dimensional derivative filter.

An overview of these extracted signals is given in Figure 3.3 on page 44. It shows the result of the frequency analysis applied on the gray-value signal of a single particle streak. This figure also shows that the frequency signal is corrupted by large errors at both signal endings. These errors are a result of boundary effects that occur during the convolution with the Hilbert kernel.

5.2.5 Depth Extraction

Within the scope of this thesis, two depth extraction techniques were applied in PSV-measurements. The main focus of this thesis is on the development of an absorption-based method that was purpose-built for the measurement of flow information in the boundary layer of a present interface. Additionally, a second depth estimation technique that uses a *focused plenoptic camera* to record a four-dimensional light field was tested in a set of measurements conducted in a turbulent *Rayleigh-Bénard* (RB) convection.

Bichromatic Depth Extraction (bPSV) As described in Section 3.2, the depth of a tracer particle can be reconstructed by means of a two-wavelength illumination and an absorbing dye.
The two light sources have to be modulated in an alternating fashion to enable a separation of both intensities. Therefore, two different illumination patterns (shown in Figure 3.5 on page 50) were tested. Both patterns ensure that the reflected intensity caused by both light sources can be properly separated. This separation is of major importance, since the depth is computed for the ratio of these intensities according to (3.28).

The depth vector that contains the depth of every point on the particle center-line is computed from two of the following previously computed streak features:

1. The non-periodical offset r_n that results from the EMD, and

2. the instantaneous amplitude $a(c)$ that was computed by means of the HT from the analytic signal.

The formula used to compute the depth depends on the illumination pattern. For the first pattern that modulates the two LED-arrays with two phase shifted sine functions, the depth is computed using (3.29).

For the second illumination pattern, where one light source is driven with a constant intensity while the second one is modulated with a sine function, the depth is given by (3.30).

The resulting depth vector has the same number of entries as the center-line. Together with the horizontal information this allows to describe the particles trajectory in the 3d space.
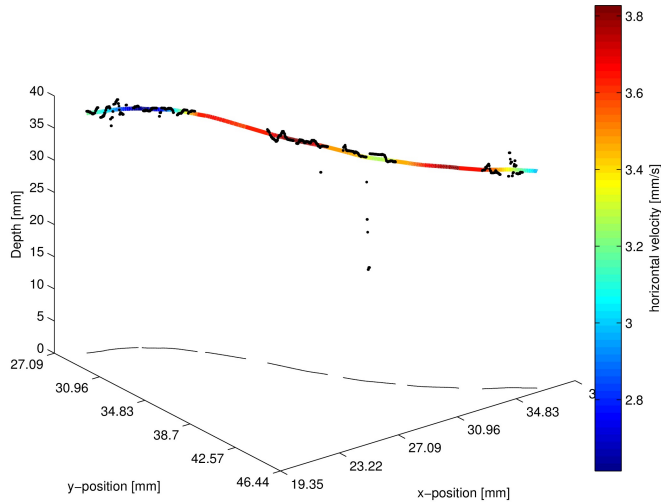
Figure 5.12: Single 3D trajectory that was measured in a *plenoptic Particle Streak Velocimetry* (pPSV) experiment; Black dots show available z-information, black lines show spatial information from the center-lines. The color-coded line is the result of a horizontal spline interpolation combined with a smoothing spline regression of the z data. The color of the line contains the information about the horizontal velocity $v_h(x)$ of the tracer-particle.

Plenoptic Depth Extraction (pPSV)   The plenoptic depth extraction is based on the depth-maps that were computed using the software *"RaytrixLive"* (Perwass, 2011), provided by the camera manufacturer.

By means of a simple lookup function, positions on the center-line are connected with height information in the depth-map. Unfortunately, the depth-maps only contain very sparse information. This is because the stereo-based approach that is used to render the depth-maps from the measured light fields depends on prominent image structures for a proper depth estimate.

As a result of this sparse depth information, the depth is only known for a small set of points on the center-line of single streaks. This circumstance is visualized in Figure 5.12 on page 99. The horizontal information given by the streak center-line (indicated by the black lines at $z = 0$) is rather dense, while the z-information that is visualized as black dots is very sparse and corrupted by large measurement errors and outliers.

The color of the line encodes the particles velocity that was computed using (3.18). As described later different spline-fits can be used in a least squares regression to compute a functional description of the 3d trajectory.

After having presented all applied processing operations and feature extraction routines necessary for the analysis of streak structures, we will turn to the actual computation of Lagrangian trajectories from the latter.

5.3 Step III: Computation of Lagrangian Trajectories

On the basis of the extracted particle streak data, long trajectories were computed. Each of these trajectories comprises a set of particle streaks that correspond to the same particle. As described in Chapter 3, this merging has a set of advantages such as

a much longer observation time and a higher robustness. Additionally, this merging of subsequent streaks allows to solve the directional ambiguity.

In accordance to the algorithmic tasks, this section is structured as follows. At the beginning the strategy used for streak matching is described. Afterwards the spline-fit that is performed on the matched streak groups is explained. Furthermore the extraction of a quality-measure that is based on the spline fit of the particles velocity is summarized. At the end of this section, the routine for the extraction of Lagrangian flow features is described.

From now on, $\hat{\mathcal{S}}$ stands for a set of N streak-lists $\mathcal{S}_i$, $i \in [0, \dots, N-1]$ that originate from N subsequent PSV-images. Each streak list $\mathcal{S}_i$ contains a set of M streaks $\mathbf{s}_j$, $j = [0, \dots, M-1]$. The contained streak-features, i.e. its center-line course $\vec{x}(c)$ as a function of the center-line position c, the width $\sigma(c)$ and the horizontal velocity $v_h(c)$ are known for every streak $\mathbf{s}_j$ in $\mathcal{S}_i$. Here the 3d center-line course $\vec{x}(c)$ combines the information obtained in the horizontal center-line extraction and the depth estimate.

5.3.1 Streak Matching

For the matching of multiple streaks that originate from subsequent images, a rather simple matching algorithm was implemented. The good performance of the matching strategy is due to an adaptive Mahalanobis distance metric that was used to define the distance between two streak-endings. As described in detail in Chapter 3, this adaptive distance definition incorporates the Euclidean distance as well as the streak direction and its length. A functional description of the adaptive Mahalanobis distance metric $d(\mathcal{E}_i, \mathcal{E}_j)$ for two arbitrary streak-endings $\mathcal{E}_i$ and $\mathcal{E}_j$ is given in (3.32).

The trajectory-lists $\hat{\mathcal{T}}$ that are computed in the assignment algorithm consist of a set of single trajectories $\mathcal{T}_k$ that store all streaks from a set of subsequent PSV-images that correspond to the same tracer-particle.

Assignment Algorithm   The assignment algorithm described in the following lines works only on the basis of the extracted streak-features and is therefore independent of the measured PSV-images. The trajectory computation is an iterative process where single streaks that can not be assigned to an existing trajectory are used to seed new trajectories. All streaks that were assigned to a trajectory because of a small adaptive Mahalanobis distance are simply added at the corresponding trajectory end.

Pseudo-code of the Streak Matching Algorithm:

1. Initialize an empty trajectory list $\hat{\mathcal{T}}$, and i=0

2. Start an active trajectory $\mathcal{T}_k$ for every streak $\mathbf{s_j}$ that is a member of the streak-list $\mathcal{S}_1$ which corresponds to the first image

3. Label all endings in $\hat{\mathcal{T}}$ as active

4. Compute the distance $d(\cdot, \cdot)$ between all endings in $\hat{\mathcal{T}}$ and the streak endings of all streaks from the next streak-list $\mathcal{S}_{i+1}$

5. All trajectories that have exactly one streak that has an end with an endpoint distance which is smaller than the threshold d_k are extended by adding this streak; all other trajectories are disabled

6. All streaks in $\mathcal{S}_{i+1}$ that were not added to a trajectory are used to start new trajectories in $\hat{\mathcal{T}}$

7. i = i+1

8. **if** i is smaller than the number of images in the measurement,
   then:
   go to 4.
   else:
   end the algorithm
   return $\hat{\mathcal{T}}$

The output of this assignment algorithm is a set of trajectories. The contained trajectories may start at different points in time and may have different lengths. All streaks features, i.e. the spatial position $x(c)$, the depth $z(c)$, the width $\sigma(c)$ and the velocity $v(c)$ of the member streaks of a trajectory are merged together. Additionally, the length of the streak as well as its start and end time are stored in each trajectory. This is achieved by means of a spline fit and a smoothing spline regression as described in the following sub-section.

Spline Fitting

In this work cubic spline fits were used for three purposes:

1. To give a functional description of the features that are stored in the non-equidistant sampled feature vectors of the trajectories.

2. To correct the noisy depth and velocity data and smoothen out the errors at the junctions between single streaks within a trajectory.

3. To enable a change of variables from the position on the center-line to a temporal dependency of the extracted trajectory features ($c[\text{px}] \rightarrow t[ms]$).

In the implementation of the presented framework, we used the spline-fit routines that were provided by the open-source `C++` library `ALGLIB` (Bochkanov, 2010).

Spline Interpolation   For the interpolation of the horizontal data, the assumption was made that all 2d data points $\vec{x}_h(c)$ on the center-line were extracted with a high precision. Therefore, the functional description of these data should be given by a smooth interpolation.

In the matching algorithm implemented within the scope of this thesis, a cubic spline-fit was used to interpolate the spatial information contained in $\vec{x}_h(c)$. A cubic spline is a piecewise cubic polynomial that is defined for the whole interval of c and that interpolates all data-points of $\vec{x}_h(c)$. The only restriction is that it interpolates all data-points and that its first and second derivative are continuous.

In the implementation all dimensions were fitted separately, i.e. a separate spline fit was applied for the x and the y-direction of $\vec{x}(c)$. For a detailed description of the mathematical background of the cubic spline-interpolation, we refer to the derivation in (De Boor, 2001).

Spline Regression   For the depth feature vector and the horizontal velocity it was not possible to interpolate the existing data in a spline interpolation satisfactorily. This is due to the fact that these signals contain errors that would falsify the results. The horizontal velocity $v_h(c)$ for example is very precise in the middle area of each streak. Due to the previously described error in the convolution with the Hilbert kernel in (3.24), boundary artifacts may occur at the endings of the signal. These artifacts are also shown in the extracted instantaneous frequency signal shown in Figure 3.3 on page 44.

The depth signal $z(c)$ of the measurements that were recorded by means of the *bichromatic Particle Streak Velocimetry* (bPSV)-approach is corrupted by the same kind of errors as the horizontal velocity. This is because it also results from the frequency analysis as described in Chapter 3 of this thesis.
The measurement errors in the depth signals that were measured using the *plenoptic Particle Streak Velocimetry* (pPSV)-approach are different. As shown in Figure 5.12 on page 99, these data were only defined on a small subset of the center-line positions and were corrupted by some large outliers caused by errors in the rendering process of the depth-map. An optimal merging function should therefore be a robust regression that allows a weighting of the influence of the input data.

In the feature extraction framework presented in this thesis, a *weighted cubic smoothing-spline* was used to merge the particle depth $z(c)$ and the horizontal velocity $v_h(c)$ of the member streaks of a trajectory. A derivation and a detailed mathematical characterization of this regression method is given in chapter five of (Hastie, 2003). It uses

a piecewise cubic polynomial fitted on an equidistant set of sampling points in a way that noisy data sets are fitted best.

Additionally, it provides the possibility to define a weight function that can be used to define the influence of single data points.

In this study we used a weight function that was built from a set of logistic functions, to increase the weight of data taken from the middle of individual streaks and to decrease the influence of the data that originate form streak endings.

After the spline interpolation of $\vec{x}_h(c)$ and the weighted regression of $z(c)$ and $v_h(c)$, these spline functions were used to define a spatial three-dimensional feature vector $\vec{x}(c)$ and a three-component velocity vector $\vec{v}(c)$

$$\vec{x}(c) \quad = (x_{h1}(c), x_{h2}(c), z(c))^t, \tag{5.40}$$

$$\vec{v}(c) \quad = \left(v_{h1}(c), v_{h2}(c), \tfrac{\mathrm{d}}{\mathrm{d}c}z(c)\right)^t. \tag{5.41}$$

In these equations $x_{hi}(c)$ and $v_{hi}(c)$ represent the ith dimension of the corresponding feature vector.

Change of Variables On the basis of the spline representation of the spatial three-dimensional position information and the spatial three-component velocity vectors, a time-dependent Lagrangian representation of these properties can be computed by changing the spatial dependency to a temporal dependency

$$\vec{x}(c) \quad \rightarrow \quad \vec{x}(t), \tag{5.42}$$

$$\vec{v}(c) \quad \rightarrow \quad \vec{v}(t). \tag{5.43}$$

This change of variables is achieved by adding a temporal dependency to the center-line position $c \rightarrow c(t)$. For this transformation we make use of the horizontal particle velocity vector v_h. Together with the start time t_0 given by the acquisition time of the image that corresponds to the first streak in the trajectory, we can use a recursive algorithm to compute $c(t)$ as follows:

$$c(t_0) \quad = \quad 0, \tag{5.44}$$

$$c(t + t_\epsilon) \quad = \quad c(t) + v_h(c(t)) * t_\epsilon. \tag{5.45}$$

In this equation t_ϵ is a small time interval. This variable has to be chosen much smaller than the smallest characteristic time scale in the observed flow field.

The result is a time-dependent center-line position defined between t_0 and the time t_{end}. The first time-point t_0 is given by the time when the first streak-image that corresponds to the trajectory was recorded, and the end time is given by the time when

the acquisition of the last image was finished. Using the same spline interpolation that was already used for the computation of a functional description of $x_h(c)$, a spline representation of the time-dependent center-line position was computed. This allows to assess all times in the interval (t_0, t_{end}).

The Lagrangian *three-dimensional three-component* (3D3C) trajectories can therefore be described by inserting the time-dependent center-line position $c(t)$ into the spatial vectors $\vec{x}(c)$ and $\vec{v}(c)$ that are defined by spline-functions of the center-line position c,

$$\vec{x}(t) = \vec{x}(c(t)), \tag{5.46}$$
$$\vec{v}(t) = \vec{v}(c(t)). \tag{5.47}$$

Quality Measure

On the basis of these time-dependent Lagrangian particle features ($\vec{x}(t)$ and $\vec{v}(t)$), a quality measure can be defined for the extracted trajectory. This measure can be used to exclude trajectories that have a bad quality due to errors in the velocity extraction or incomplete streaks.

The definition of this quality measure is motivated by the fact that the temporal integral over the horizontal velocity and the length of the trajectory should be the same

$$\underbrace{\int_{t_0}^{t_{\text{end}}} v(t)\,\mathrm{d}t}_{A} \approx \underbrace{c(0) - c(t_{\text{end}})}_{B}. \tag{5.48}$$

Large differences between the left and the right hand side of (5.48) may occur for two reasons. The first one is an error in the velocity vector that results in a too large or a too small left hand side of this equation. A second possible reason is an error in the streak extraction. If the trajectory consists of incomplete streaks, the right hand side deviates from the result of the integral. Based on these observations, the following parameter R was defined to describe the quality of each trajectory,

$$R = \frac{|A - B|}{0.5(A + B)}. \tag{5.49}$$

Here A is the integral over the time-depended velocity feature-vector and B is the length of the extracted center-line. Both are defined in (5.48). Large R values indicate a large difference between both sides of (5.48).

In the implemented framework a threshold can be defined that causes a rejection of trajectories with a quality measure that is larger than this value.

For all quantitative experiments that were done in the context of this study, this threshold was set to 10 %.

5.3.2 Lagrangian Features

For the computation of the Lagrangian features that were described in Chapter 3, the spline representation of the particle trajectories and the velocity course along these trajectories was used.
Since the Lagrangian information of a single particle that is moved within a turbulent flow field comprises nearly no information about the characteristics of a turbulent flow field, statistical measures were extracted on the basis of the Lagrangian information of a large ensemble of tracer particles.

Two-Particle Dispersion

For the computation of the Lagrangian average of the particle dispersion motivated in Chapter 3, a set of particle pairs $\mathbf{P}$ has to be extracted. As described in detail in the methodology chapter of this work, each particle pair in this set must possess a Euclidean distance that is lower than a predefined initial distance r_0 at some time point t_p.

The extraction of a set of feasible particle pairs is performed on the basis of the data that are contained in a set of trajectories $\hat{\mathcal{T}}$. The extraction of these particle pairs P_i and the corresponding time points t_{pi} is solved in an exhaustive search that computes the Euclidean distance $d_e\left(\vec{x}_k\left(t\right), \vec{x}_j\left((t)\right)\right)$ for all possible trajectory-combinations $\left(\mathcal{T}_k, \mathcal{T}_j\right)$ and all time-points where both trajectories coexist.

Pseudo-code of the trajectory-pair computation algorithm

1. Initialize $\mathbf{P} = \emptyset$ and $i = 0$;

2. **For:** k = 0 **to** *size($\hat{\mathcal{T}}$)* **do:**

   a) **For:** j = k **to**
      size($\hat{\mathcal{T}}$) **do:**
      i. **If:** there is a point in time when $|d_e\left(\vec{x}_k\left(t_p\right), \vec{x}_j\left(t_p\right)\right) - r_0| = 0$
         - add $P_i = \left(\mathcal{T}_k, \mathcal{T}_j\right)$ to the set of particle pairs $\mathbf{P}$, set $i = i + 1$ and store the corresponding time t_{pi}

3. **return P**

The result is a set of trajectory-pairs and time-points which indicate when the particle distance was equal to the previously defined initial separation r_0.

For the computation of the Lagrangian two-particle dispersion statistic, the time coordinates of all trajectories were shifted by the corresponding time points t_{pi}. In the following step, the individual pair dispersion was computed as described in (3.36). Thereafter the Lagrangian average of all individual particle pair dispersion behaviors was computed according to (3.37).

For a turbulent RB convection, this Lagrangian measure was extracted in a series of experiments that were conducted in the scope of this study. The results of these experiments are presented in Section 6.

Lagrangian Acceleration Statistics

A second quantitative turbulence measure studied in the scope of this thesis is the Lagrangian particle acceleration.

The extraction routine for the computation of this Lagrangian single particle characteristic from the measured 3D3C trajectory is based on the spline representation of the 3C particle velocity. With a predefined temporal sampling rate, the algorithm extracts acceleration values from the instantaneous velocity information. These accelerations are simply stored in a histogram data structure that allows an easy evaluation of the underlying Lagrangian acceleration distribution in the observed turbulence.

5.4 Semi-artificial Benchmark Data-Sets

To validate the velocity estimation, a set of benchmark datasets proposed by Berthe et al. (2010) were used to compute a set of semi-artificial data sets that contain streaks from particles which move with a known velocity.
These datasets were measured using a particle mounted on the head of a high-precision milling cutter. The particle was moved in a dyed liquid on different trajectories and recorded by a single camera recording short-exposure (single shot) PIV-data. A more detailed description of the technique used for the measurement of these benchmark measurements is given in Section 2.2 and in the paper that originally published these data (Berthe et al., 2010).

From each PIV-image sequence containing N images I_t with $t = 0 \ldots N-1$ that comprise the gray-values $i_{x,y,t}$, a single PSV image was computed by integrating over time and modulating the image intensities with a time-dependent, sinusoidal function.

$$I_{sum} = \sum_{t=0}^{t=N-1} i_{x,y,t} \left(1 + 0.5 \sin \left(2\pi \frac{F}{\zeta} t \right) \right) \tag{5.50}$$

In this equation ζ[Hz] is the PIV camera frame-rate, F[Hz] is the simulated illumination frequency and t is the number of the current times step. As shown in Figure 5.13 on page 108, the integrated PSV data look similar to the data obtained in our long exposure PSV measurements (cf.: Figure 5.9 on page 91).

The illumination frequency F was varied in a range where the number of periods that were written along the streak was larger than two (to obtain a robust frequency signal). The wavelength of the spatial signal on the streak was at least 10 px long (to avoid errors due to the Nyquist-Shannon sampling theorem (Nyquist, 1924)). The intensity-modulation frequency F for the circular measurement #1, where the particle was moved with a constant velocity of $v = 25$ mm/s, was varied between 0.2 Hz and 2.0 Hz. For the slower linear measurements #2 to #5, where the particles were moved with $v = 9.1$ mm/s, F was varied between 0.2 Hz and 1.4 Hz.

(a) #1: Circular movement with 25mm/s modulated with 0.9Hz

(b) #2: Vertical movement with 9.1mm/s modulated with 0.7Hz

(c) #3: Diagonal movement with 9.1mm/s modulated with 0.7Hz

(d) #5: Diagonal movement with 9.1mm/s modulated with 0.7Hz

(e) #4: Horizontal movement with 9.1mm/s modulated with 0.7Hz
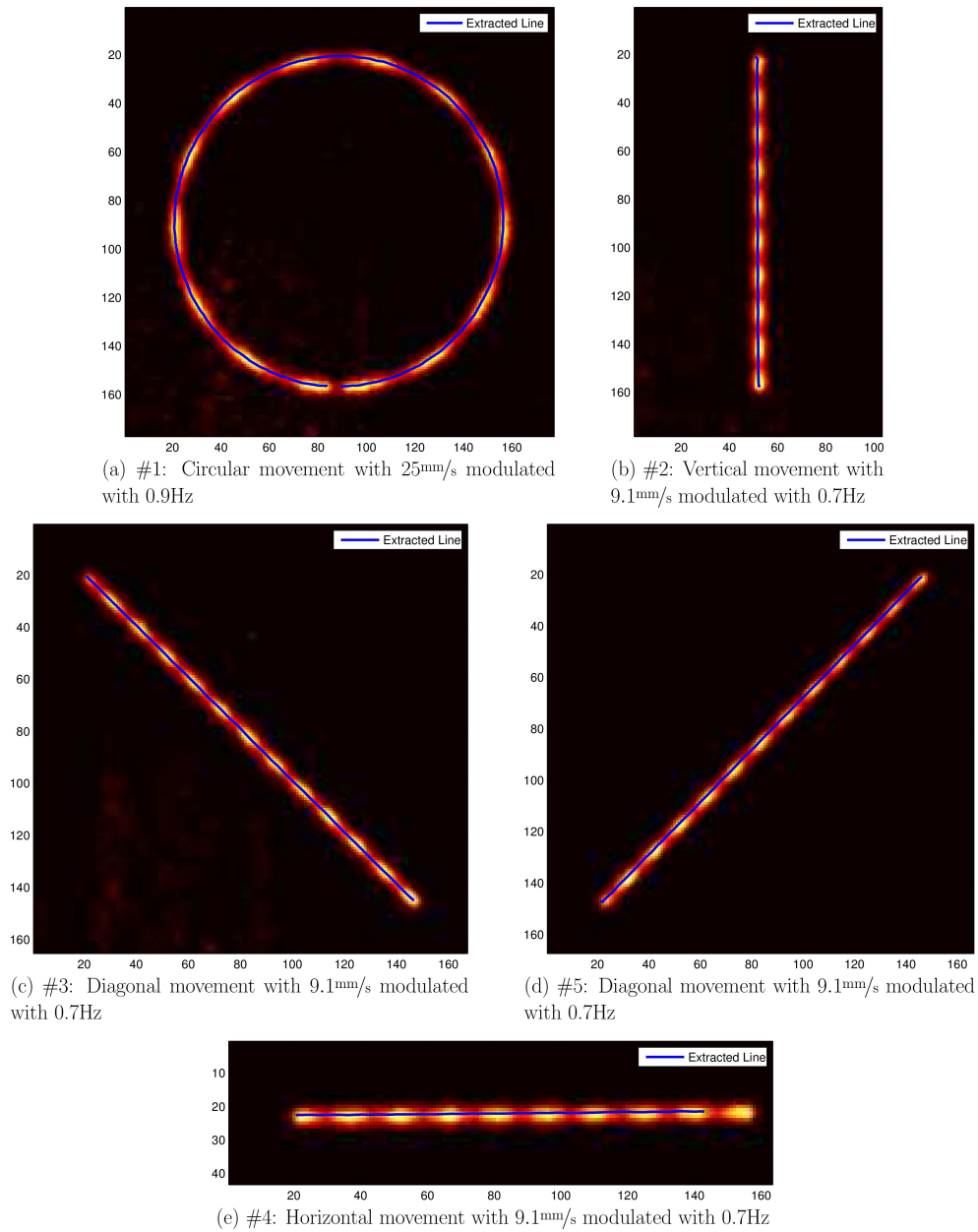
Figure 5.13: Data sets computed by integrating the PIV benchmark data sets measured by Berthe et al. (2010) over time. The sinusoidal intensity modulation of the signal is introduced by a sine function in the integration (cf. (5.50)). The extracted middle-lines are shown as blue lines in the middle of the streak structures. (Voss et al., 2012)

6 Results and Discussion

This chapter comprises the results of the different experiments that were conducted in the course of this thesis. It includes all validation experiments conducted to assess the performance and the precision of single parts of the particle streak extraction framework as well as quantitative measurements of a turbulent *Rayleigh-Bénard* (RB) convection. In this context several turbulence features and Lagrangian characteristics were derived from the Lagrangian trajectories measured in the interfacial region of the air-water boundary layer. These turbulence characteristics are compared to results that were obtained in other experimental and theoretical studies recently published in the field of fluid-dynamics.

The outline of this chapter follows the chronological order of the presented experiments. The first section ("Precision of the Proposed Techniques") summarizes the precision that can be expected in the *bichromatic Particle Streak Velocimetry* (bPSV) measurements and in the *plenoptic Particle Streak Velocimetry* (pPSV) measurements. After that the precision of the estimated velocities that are computed on the basis of the periodical gray-value signal is assessed in Section 6.2 ("Benchmark Experiments"). This is done by means of some semi-artificial benchmark data sets. The latter were computed on the basis of a set of real *Particle Image Velocimetry* (PIV) benchmark measurements (Berthe et al., 2010).

In the following Section 6.3, the Lagrangian trajectories are shown that were recorded to characterize the interfacial flow in the free air-water interface of a turbulent RB-convection. Since this turbulence measurements were recorded using the two different depth extraction techniques, i.e. the light-filed based approach and the bichromatic approach, two subsections summarize the resulting flow fields. Here, the first subsection shows the results obtained by means of the bPSV approach and the second section contains the results of the pPSV method.

The last part of this chapter (Section 6.4) focuses on the description of the measured turbulence and on the extracted Lagrangian turbulence characteristics. Therefore, different models and theoretic predictions developed to describe isotropic turbulences are used to characterize the obtained Lagrangian turbulence features of the interfacial flow field. Furthermore, these models are used in this section to compare the extracted turbulence characteristics (i.e. the Lagrangian acceleration distribution and the Lagrangian particle pair dispersion) with the results obtained by other state-of-the-art methods that were proposed in the field.

6.1 Precision of the Proposed Techniques

As pointed out by Haußecker et al. (1998), a quantitative image sequence analysis routine requires a geometric and radiometric calibration as well as a quantitative error analysis of the entire chain of operations used for the flow feature extraction.

Since the quality of the results can only be as good as the least precise part of the system, this section summarizes the precision of all components of the flow feature extraction framework to obtain a valid and reasonable error analysis of the full system.

A detailed estimation of the radiometric precision by means of a sensor characterization was only performed for the gray-value camera used in the bPSV-measurements since the depth estimate of this approach relies crucially on the precision of the measured absolute intensities as described in Section 3.2.
The precision of the absolute intensities measured by means of a *focused plenoptic camera* in the pPSV-experiments does not influence the depth estimate of this method since this technique relies on a stereo based depth extraction that uses the measured light fields (cf. Section 3.3). Therefore, this study refrains from a characterization of the radiometric precision that can be reached by the sensor array in the *focused plenoptic camera*.

6.1.1 Radiometric Precision of bPSV Experiments

As described earlier in Chapter 5, the *charge-coupled device* (CCD)-sensor of the used gray-value camera was characterized in a radiometric calibration that fulfills the requirements of the *European Machine Vision Association* (EMVA)1288 standard (EMVA, 2010). The following error analysis is based on the results of this characterization.

One very important sensor characteristic that directly influences the depth estimate is the *overall system gain K*. This parameter has to be characterized separately for the three wavelength areas (K_i, $i \in \{$red, green, blue$\}$). As described in detail in Section 5.1, it describes the digital output caused by a single electron in a pixel of the sensor. Table 5.1 on page 78 summarizes the results of the sensor calibration. Here it can be demonstrated that the *overall system gain* for the higher wavelength area, i.e. for blue and green light, agrees nicely within the 0.4 % measurement error. The deviation for longer wavelengths is much larger. The *overall system gains* K_{blue} and K_{red} differ more than 1 %.

The same tendency was observed for the wavelength-dependent *quantum efficiency* η_i, $i \in \{$red, green, blue$\}$ of the pixels in the CCD-sensor. By its definition in the EMVA1288 standard, this characteristic measure describes the average number of electrons induced in the semiconductor-junction in a single pixel of the imaging device. On the one hand the *quantum efficiency* depends on the materials and coatings that

were used to manufacture the sensor array. On the other hand it is dependent on the wavelength of the incident light. This is due to the fact that the photon energy scales linearly with their frequency.

For the present sensor array, the *quantum efficiencies* are nearly the same for the blue and the green light ($\eta_{blue} = (505.5 \pm 1.8) \cdot 10^{-3}\,\mathrm{e^-}/\mathrm{Photon}$ and $\eta_{green} = (505.2 \pm 2.2) \cdot 10^{-3}\,\mathrm{e^-}/\mathrm{Photon}$). In contrast, the photon responsivity for light with larger wavelengths is much smaller ($\eta_{red} = (347.9 \pm 1.3) \cdot 10^{-3}\,\mathrm{e^-}/\mathrm{Photon}$) because of the smaller energy contribution per photon.

For a more intuitive characterization of imaging sensors, the product of the *overall system gain* and the *photo response* can be computed for each wavelength range. This characteristic measure is called *photo responsivity R* [$^{\mathrm{DN}}/\mathrm{Photon}$].

$$R_i = K_i \eta_i, \text{ with } i \in \{\text{red, green, blue}\} \tag{6.1}$$

As indicated by the units of R, it describes the direct correlation between the number of photons that hit a pixel and its *digital number* (DN) output. Furthermore, it is much easier to assess this characteristic by means of a calibrated Ulbricht sphere as described earlier in Chapter 5 of this thesis. The diagram on the right hand side in Figure 5.3 on page 78 shows the characterization measurement that were performed to determine the *photo response* for the image sensor. The plot clearly visualizes the wavelength dependency of this measure. While the response on smaller wavelengths (blue and green) is very similar, it shows a drastic deviation for larger wavelengths.

The *photo response* curve can also be used to analyze the linearity of the response as a function of the signal intensity. In this context the course of the photo response curve shows a nice linear dependency between the intensity of the dark-signal and the saturation-intensity for all three wavelength regions. These intensities were computed in the noise model derived in Section 5.1.

The *Signal-to-Noise Ratio* (SNR) behavior of the camera was also determined in the radiometric camera characterization. Figure 5.4 on page 80 shows the course of the SNR values for the three wavelength regions ({red, green, blue}) as a function of the irradiation [$^{\mathrm{photons}}/\mathrm{pixel}$] on the sensor array. In the noise model of the EMVA1288 standard, the SNR is defined by the ratio of the photon-induced gray-value and its variance on the sensor array (cf. Section 5.1 in Chapter 5). Additionally, this figure shows the SNR-course of an ideal imaging sensor and the (SNR = 1)-threshold.

Summarizing the errors that occur because of wavelength-dependent differences in the linearity of the sensor pixels can be neglected. Both light sources used in the context of this study ($\lambda_1 = 405\,\mathrm{nm}$ and $\lambda_2 = 465\,\mathrm{nm}$) are in the high frequent regime that seems to have a constant linearity down to wavelengths of about $550\,\mathrm{nm}$ (green). The SNR-threshold corresponds to a sensor irradiation of about $40\,^{\mathrm{photons}}/\mathrm{px}$. Using the photo-response parameter $R = \eta K$, this minimal irradiation can be converted in

units of [DN]. Therefore, a threshold μ_Δ[DN] can be computed from the SNR-threshold defining a gray-value difference that can be resolved properly in the recorded images.

$$\mu_\Delta = R * 40 \, \text{photons}/\text{px} \approx 8 \, \text{DN} \tag{6.2}$$

As a conclusion of the camera calibration in Chapter 5, it can be said that reliable particle streak signals caused by reflections of the blue and the violet illumination can be measured between the intensity of the dark signal $\mu_{y.\text{dark}} = 241 \, \text{DN}$ and the saturation intensity $\mu_{y.\text{sat}} = 3706 \, \text{DN}$. Low intensity signals can reliably be distinguished from the background if they differ from $\mu_{y.\text{dark}}$ more than $\mu_\delta = 8 \, \text{DN}$.

6.1.2 Spatial Precision of bPSV and pPSV

In the characterization of the spatial precision that can be reached by the presented measurement methods, three sources of error have to be considered separately.

1. The conversion of positions and velocities is linearly dependent on the pixel-size. This magnification measure has to be determined determined previously to each experiment by a calibration measurement using a mm-grid. In a manual evaluation, the number of pixels that constitute a distance of 30 mm were measured at least five times. On the basis of these counts, the pixel-size α and its standard deviation σ_α can be estimated. Typical pixel sizes and standard deviations observed in the turbulent RB convection measurements amount to $\alpha = (3 \cdot 10^{-2} \pm 5 \cdot 10^{-5}) \, \text{mm}/\text{px}$. This means, the expected error can be approximated to be $0.2\,\%$ of the pixel size.

2. The second source for a spatial error in the measurement originates from the perspective distortion that causes a change of the pixel-size for different depths. To quantify this error, the mm-grid used as calibration target was imaged in different depths within the volume of interest. In all bPSV measurements, this volume was rather thin because the developed measurement method focuses on the measurement of flow fields in the thin boundary layer of interfaces. Deeper regions (below depths of 15 mm) were not imaged because all the light from these regions was absorbed due to the used dye. In all measurements the deviation of the pixel size in different depths was much smaller than the approximated pixel size error and could therefore not be extracted.

3. The third spatial uncertainty that arises is the error made in the *Levenberg-Marquardt* (LM)-fit in the streak-extraction routine described in Section 5.2. Since the sub-pixel precise position is computed from the maximum position of the fitted Gaussian bell-curve, the error of the Gauss-fit can be used to quantify the extraction error.
   From the output of the fit routine the expected uncertainty of the parameters

was computed by means of the covariance matrix. Typical observed fit-errors of the center-line position were in the order of magnitude of $0.1\,$px. Assuming a typical pixel size of $\alpha = 3 \cdot 10^{-2}\,$mm/px, the absolute expected error introduced by the uncertainty of the LM fit can be estimated to be $3 \cdot 10^{-3}\,$mm.

In conclusion, it can be said that the expected spatial error of all measurements that were done within the scope of this thesis is dominated by the error of the LM-fit.

6.1.3 Precision of the Velocity Estimate of bPSV and pPSV

The precision of the velocity estimate by means of a periodical modulated illumination and a frequency analysis of the reflected signal depends on various circumstances. The most important condition for a precise velocity estimate is that the modulation frequency of the light sources $F[\text{Hz}]$ and the exposure time $t_{exp}[\text{s}]$ should be properly adapted to the expected velocities in the flow field.
A too high frequency would cause a constant intensity signal from slow particles. Choosing a too short exposure time results in short streak-structures that don't comprise enough periods of the modulated illumination for a precise velocity estimate. A description of how to choose the correct modulation frequency and an appropriate exposure time is given in Section 3.1.

In a series of experiments using semi-artificial data sets computed on the basis of some previously published PIV-benchmark data sets (Berthe et al., 2010), the previously mentioned experimental conditions were varied in order to characterize their influence on the precision of the velocity estimate. A detailed description of the semi-artificial data sets is given in Section 5.4 of Chapter 5.

The results of the velocity validation are summarized in Table 6.1 on page 118. The standard deviation of the velocity estimate of all values along the extracted trajectories is used to estimate the expected error of the velocity estimate. It can be seen, that for all benchmark data sets it is below $0.5\,\%$ of the measured velocity. Additionally, it can be demonstrated that the ground truth velocity lies within a 1σ environment of the mean of the instantaneous velocities extracted along trajectories.

As described in Section 5.3, an additional quality measure can be used that compares the length of a trajectory with the temporal integral over the horizontal particle velocity along the trajectory. On the basis of this quality measure R that is defined in (5.49), all trajectories with a velocity deviation larger than a certain percentage can be rejected. For all quantitative experiments that were conducted within the scope of this thesis, this threshold was set to $R = 10\,\%$. According to the definition of R, small R values correspond to high qualities.

A quality measure distribution of the trajectories extracted from *Measurement#4* is shown in Figure 6.1 on page 114. This figure shows that the 10% threshold restricts
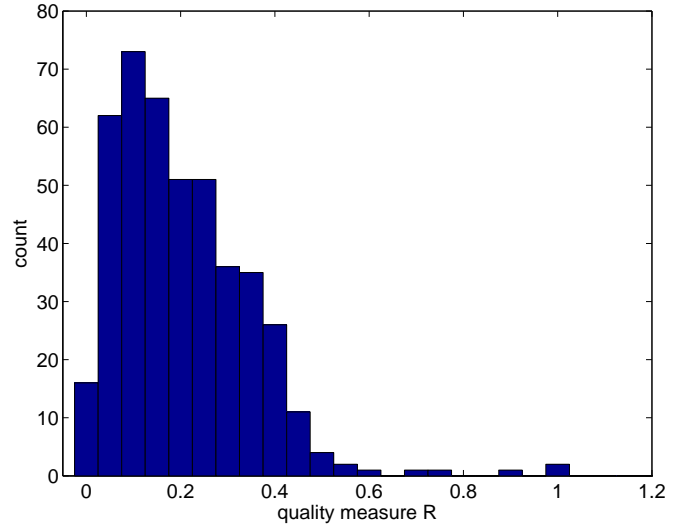
Figure 6.1: This figure shows the distribution of the trajectory quality measure obtained in *Measurement#4*. In the quantitative evaluations only trajectories with a quality measures smaller than 10%, i.e. high quality, were considered.

the evaluation to trajectories from the left (high quality) tail of the distribution. For future experiments, this threshold can be chosen depending on the required precision of the velocity estimate and the needed for large trajectory numbers in the statistical evaluation the threshold.

6.1.4 Precision of the Bichromatic Depth Estimate

In the following estimation of the precision that can be reached in the bichromatic approach, several error sources have to be taken into account. On the one hand the SNR of the imaging device restricts the precision of the intensity information that can be extracted from the measured images. This source of error was previously estimated in the EMVA camera calibration (cf. Section 5.1). On the other hand the streak extraction-routine itself presents a possible error source that can corrupt the extracted intensity values. This uncertainty originates from the intensity extraction by means of a LM-fit that computes the intensity from the parameter of a Gaussian bell-curve.

Taking into account all possible error sources that corrupt the intensity measurement, we assume the relative error of the measured absolute intensities to be about $\frac{\Delta I}{I} \approx 0.02$. This estimation agrees well with gray-value uncertainties that were observed in other particle based flow measurements. Typically these uncertainties vary between 1 % and 10 % (Tropea et al., 2007).

Using the depth equation of the bichromatic depth estimation (3.28) that defines $z(I_1, I_2)$, the measurement error $\Delta z(I_1, I_2)$ can be computed from the following equa-

tion:

$$
\begin{aligned}
\Delta z(I_1, I_2) &= \sqrt{\left(\frac{\partial z}{\partial I_1}\Delta I_1\right)^2 + \left(\frac{\partial z}{\partial I_2}\Delta I_2\right)^2} \\
&= \underbrace{\left|\frac{z_{*1}z_{*2}}{z_{*1} - z_{*2}}\right|}_{Z_*(z_{*1}, z_{*2})} \sqrt{\frac{\Delta I_1^2}{I_1^2} + \frac{\Delta I_2^2}{I_2}}
\end{aligned}
\tag{6.3}
$$

In this equation z_{*1} and z_{*2} are given by the penetration depths of the two light sources in the dyed liquid. Therefore, the uncertainty of the depth estimate depends linearly on the relative intensity error and scales with a factor $Z_*(z_{*1}, z_{*2})$, which is given by the ratio between the penetration depths of the dye for the two wavelengths.

To visualize the influence of this ratio on the uncertainty of the depth estimate, we replaced z_{*2} by $z_{*2} = Cz_{*1}$ and plotted the logarithm of Z_* for $z_{1*} = 1$ as a function of $C = \frac{z_{*2}}{z_{*1}}$ (cf. Figure 6.2).

The penetration depths of the dye at the given wavelengths are summarized in Chapter 4 of this thesis. As visualized in Figure 4.3 on page 66, the ratio between both penetration depths for the used wavelengths is

$$
\frac{z_{*2}}{z_{*1}} = \frac{2}{3}.
\tag{6.4}
$$

Therefore, the expected uncertainty of the depth estimate can be computed from Z_* using (6.3). The expected relative intensity error amounts to $\Delta z = 0.04z_{1*}$.

The precision of penetration depths of both wavelengths z_{*1} and z_{*2} at the used dye concentration also contributes to the error of the depth extraction. As proposed by Berthe et al. (2010), a calibration measurement is performed previously to each measurement to estimate these parameters with the highest possible precision. By using the absorption calibration measurement described in Chapter 3 of this thesis, the error of the penetration depths can be assumed to be smaller than $1\,\%$. Therefore, this source of error can be neglected because the overall error of the depth estimate is dominated by the precision of the measured absolute intensity.

This means that it is possible to obtain a precision of $4\,\%$ of the penetration depth by using *Tartrazine* (E112) and light sources at $\lambda_1 = 405\,\mathrm{nm}$ and at $\lambda_2 = 465\,\mathrm{nm}$.

6.1.5 Depth Range of the Bichromatic Technique

The assessable *depth range* can be derived on the basis of Lambert Beer's law for the absorption of a single wavelength. Here we have to use the absorption behavior of the

Figure 6.2: This figure shows the dependency of the error of the depth-estimate on the ratio of the wavelength-dependent extinction coefficients. It can be seen that a large difference between the extinction coefficients, i.e. a small $C = \frac{z_{*2}}{z_{*1}}$, yields a drastic reduction of the measurement error.
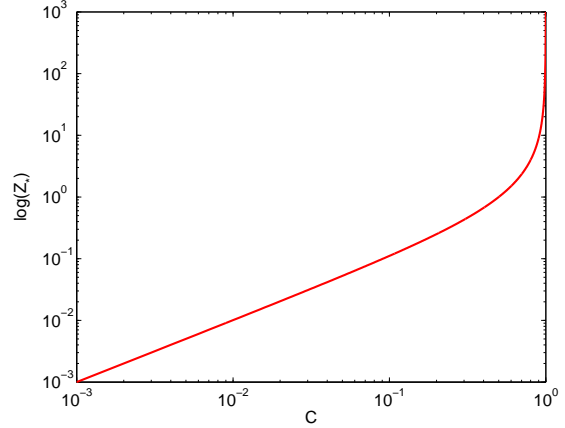
wavelength with the smaller penetration depth z_* because this property restricts the depth range of the method.

Since the exponent of the absorption law (3.27) is linearly dependent on the penetration depth that also restricts the depth-range, it is obvious that also the depth range can be estimated from this linearity.

The assessable depth range depends on the dynamic range of the camera. As shown in the radiometric calibration in Chapter 5, it is possible to measure reliable intensity signals between the dark signal intensity $\mu_{y.\text{dark}} = 241\,\text{DN}$ and the saturation intensity $\mu_{y.\text{sat}} = 3706\,\text{DN}$.

$$\frac{I_0 * \exp\left(-2z/z_*\right)}{I_0} > \frac{\mu_{y.\text{dark}}}{\mu_{y.\text{sat}}} = 0.067 \tag{6.5}$$

This condition is fulfilled if $z < 1.35 z_*$. Therefore, the fraction of the intensity that hits the sensor from depths below $z = 1.35 z_*$ causes a signal that is below the dark signal $\mu_{y.\text{dark}}$ and therefore can be neglected.
The depth assessable by the bichromatic technique ranges therefore in the interval $z \in [0; 1.35 z_*)$.

6.1.6 Precision of the Plenoptic Depth Estimate

The absolute precision of the depth estimate obtained in the measurements with the second developed technique using a *focused plenoptic camera* depends on the depth range achieved in the individual measurements.

In the calibration measurements described in Section 3.3 on page 50, a general correlation between the horizontal dimensions of the measurement volume and the depth

range was observed. For the used camera the depth range is always of the same order of magnitude as the horizontal dimensions.

In the data sheet of the *focused plenoptic camera* (*R11, Raytrix GmbH, Kiel, Germany*), the manufacturer claims that the supplied software *RXLive* resolves 100 depth layers within the measurement volume (cf. Figure A.5 on page 165). This would imply a theoretically reachable resolution of $\approx 1\,\%$ of the depth range.

Unfortunately performance of the depth extraction depends crucially on the depth extraction routine itself and on the performance of the algorithm on the measured data sets. To visualize the quality of the depth information that was extracted from the pPSV measurements in this study, we plotted a *three-dimensional* (3d) trajectory in Figure 6.6 on page 125. It can clearly be seen that the depth information in the pPSV measurements is corrupted by an error that is much larger than $1\,\%$.
Using a statistical analysis of the depth data that were observed on the trajectories in the pPSV measurements of this study, we observed a relative standard derivation $\sigma_{\text{depth}} = 6\,\%$ in the locale mean of the depth signal.

6.1.7 Depth Range of the Plenoptic Technique

The depth range can be resolved by means of the *focused plenoptic camera* and depends on the extended focal depth which can be achieved in the rendered "all-in-focus" images. This focal depth is defined by the camera geometry, the position of the used objective and the position of the micro-lens array. In a set of calibration measurements described in Chapter 3 it was found that the depth range of the *focused plenoptic camera* was always within the same order of magnitude as the horizontal dimensions of the recorded images. This limit is systematic and can also be explained by the camera geometry of the plenoptic camera model introduced in Chapter 2.

6.2 Benchmark Experiments

The following section presents the results of the validation experiments that were performed to estimate the precision of the instantaneous velocity computed by means of a frequency analysis. In these experiments a set of PIV benchmark measurements proposed by Berthe et al. (2010) were used to compute semi-artificial *Particle Streak Velocimetry* (PSV) trajectories as described in Section 5.4 of Chapter 5. For the computation of these semi-artificial data sets the simulated illumination frequency was varied systematically. After that the instantaneous velocity computed along the extracted trajectories was compared to the ground truth velocities used to generate the PIV benchmark measurements.

Figure 6.3: Velocity results for the semi-artificial data sets built on the basis of a PIV Benchmark data set previously published by Berthe et al. (2010). In this plot the average velocity is shown as a function of the illumination frequency F. The illumination frequency in the plotted range has no influence on the quality of the velocity estimation.
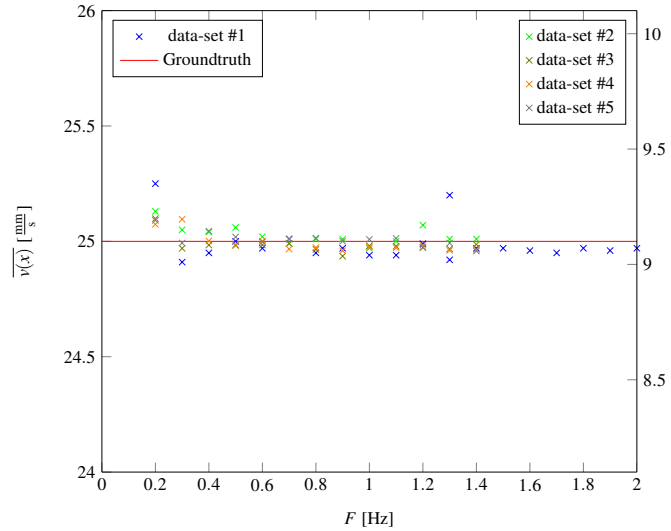
measurement	velocity $\left[\frac{mm}{s}\right]$	F [Hz]	$\overline{v(x)}[\frac{mm}{s}]$	$std\left(v(x)\right)$
#1	25.0	0.2 - 2.0	24.98	0.09
#2	9.1	0.2 - 1.4	9.12	0.04
#3	9.1	0.2 - 1.4	9.08	0.04
#4	9.1	0.2 - 1.4	9.09	0.04
#5	9.1	0.2 - 1.4	9.11	0.03

Table 6.1: Statistical evaluation of the benchmark results. The deviation of the mean velocity $\overline{v(x)}$ from the ground truth given by the speed of the micrometre traverse T is less than one sigma of the standard deviation.

The velocity results obtained from these semi-artificial data sets indicate that the proposed algorithm allows an extraction of horizontal particle trajectories as well as the computation of their instantaneous horizontal velocity based on a frequency analysis of the reflected light from the intensity modulated illumination. As summarized in Table 6.1 the extracted average velocity matches the ground truth velocity given by the speed of the traversal unit. It can be seen that the variations of the simulated illumination frequency have no influence on the precision of the velocity estimate (cf. Figure 6.3). The precision of the extracted instantaneous velocities as well as their standard deviations indicate that the relative uncertainty of the velocity estimate is smaller than $0.5\,\%$.

The boxplot in Figure 6.4 shows a statistical analysis of the velocity results of all frequencies for the linear data sets (i.e. data set #2 to data set #5). In this plot small deviations from the ground truth ($v = 9.1\,\mathrm{mm/s}$) can be observed. Since these deviations are scattered around the ground truth and because the ground truth is
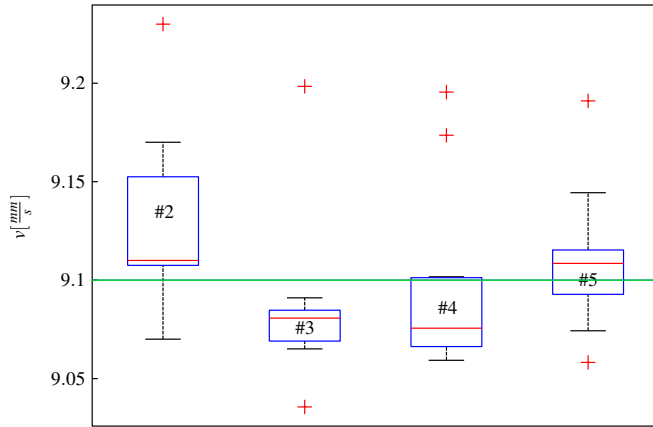
Figure 6.4: Boxplot of the velocities obtained from the analysis of the semi-artificial data sets #2 to #4. The average of all velocities (red lines) is near ground truth (green line), but for two measurements the ground truth is not in the area between the lower quantile (Q1) and the upper quantile (Q3), indicated by the squares. The black brackets show the maxima and minima of the velocity distribution and outlier are visualized as red crosses.

within a 1σ environment of the mean value, it is unlikely that the observed deviations are caused by a systematic error of the measurement.

6.3 Turbulent *Rayleigh-Bénard* (RB) convection

This section provides an overview of the results that were obtained from the Lagrangian measurements of turbulent RB flow fields. All turbulences were generated by means of the infrared heated vessel described in detail in Section 4.5 on page 71. For all measurements taken in this study the vessel was filled with deionized water. The total height was set to $\tilde{H} = (50 \pm 3)\,\text{mm}$.

The results that are shown in this section were measured in the air-water interface of a turbulent RB convection by means of the two developed PSV techniques. The first series of measurements was acquired using the bPSV technique based on a bichromatic depth extraction approach (cf. Section 3.1 on page 34). In the second series of measurements the pPSV approach was used. This technique relies on a depth extraction from light field measurements that were taken by means of a *focused plenoptic camera* (cf. Section 3.3 on page 50).

The heating power of the RB vessel was set to $945\,\text{W}$ in both measurement series. Previously to each measurement the setup was heated for several hours to guarantee that the turbulence reached an equilibrium state. In this state of equilibrium the mean temperature of the water in the bulk, i.e. in the middle of the vessel, was measured using a *Pt100 thermo sensor*. Additionally, this sensor was used to measure an average temperature difference between the heated bottom of the vessel and the free water surface that was cooled by the environment due to processes such as evaporation and conductive heat transfer. All measured temperatures are listed in Table 6.2. This

Item	Value	Comment
mean temperature	$T = (51 \pm 0.2)\,°\mathrm{C}$	
temperature difference	$\Delta T = (23 \pm 0.3)\,°\mathrm{C}$	
bPSV dye concentration	$c_{\mathrm{bPSV}} = 12\,\mathrm{mg/l}$	used for the bichromatic depth extraction
pPSV dye concentration	$c_{\mathrm{pPSV}} \approx 5\,\mathrm{mg/l}$	used to remove scattered light from below the measurement volume
kinematic viscosity of water	$\nu_{55°C} = 0.551 \cdot 10^{-6}\,\mathrm{m^2/s}$	(Kestin et al., 1978)
isobaric thermal expansion coefficient	$\alpha_{\mathrm{i}}\,(50°C) = 4.578 \cdot 10^{-4}\,\mathrm{1/K}$	(Irvine Jr and Duignan, 1985)
thermal diffusivity	$\kappa = 1.44 \cdot 10^{-7}\,\mathrm{m^2/s}$	(Salazar, 2003)

Table 6.2: Summary of the experimental parameter in the RB experiments. This table shows the parametrization of the experimental setup as well as the most important material properties of the deionized water at the equilibrium temperature.

table also summarizes the most important parameters of the turbulent RB convection that were generated for the characterization experiments.

As motivated in Section 2.1, a set of dimensionless scaling parameters has to be approximated to enable a comparison of the measured turbulence characteristics with the outcome of other studies and to use scale-invariant models for the description of the observed processes.

6.3.1 Scaling Parameters

For a quantitative description of the turbulence that was generated in the previously described RB experiments, the dimensionless *Rayleigh number* (Ra) and the dimensionless *Reynolds number* (Re) were estimated according to the derivation described in Section 2.1 of Chapter 2.

Ra can therefore be approximated as described in Equation (2.1) using the material properties from Table 6.2.

$$Ra \approx 7 \cdot 10^7 \tag{6.6}$$

Common turbulences in the field of industrial engineering lie in the *Rayleigh number* interval between $Ra = 10^6$ and $Ra = 10^8$. Therefore, the turbulence generated in the

RB vessel can be seen as a feasible model of a turbulent process from an industrial application.

The *Reynolds number* can be interpreted as the ratio between the kinematic forces and the viscous forces that occur in the turbulence (cf. Chapter 2). It can be computed by using Equation (2.2) as follows:

$$
\begin{aligned}
Re &= \frac{ul}{\nu} \\
&\approx 115
\end{aligned}
\tag{6.7}
$$

The *Reynolds numbers* that were extracted from the single turbulence measurements in this study were all within the same order of magnitude. The estimated numbers scatter with a standard deviation of about ± 10 around the mean value given in (6.7).

As motivated in Chapter 2, a characterization of the observed turbulence by microscopic scaling variables is quite useful and common in turbulence models that describe Lagrangian turbulence characteristics.

The most prominent scaling parameters that are used in this context are the Kolmogorov microscales. These characteristic scales are given by the smallest scales that can be observed in a turbulent flow. As described in Section 2.1, these scales define a length scale η_K, a time scale τ_K and a velocity scale u_K. By definition the Kolmogorov microscales can be computed from the fluids kinematic viscosity ν and the *energy dissipation rate* $\langle \epsilon \rangle$.

Since a precise estimate of the *energy dissipation* $\langle \epsilon \rangle$ is not obtainable from the measured PSV sequences, we use the correlation between the Kolmogorov microscales and the *Reynolds number* derived in Section 2.1. The equations (2.4), (2.5) and (2.6) that were derived in Chapter 2 of this thesis provide an approximation of these microscales. They depend on the characteristic length scales and the characteristic velocities that can be observed in the turbulence.

In the present study we estimated the characteristic length of the large-scale eddies l by visual inspection from the measured image series. The characteristic velocity was approximated from the root mean squared (rms) velocity of the fastest $10\,\%$ of all measured trajectories. Slower trajectories, corresponding to small-scale turbulences, were ignored in this averaging. Together with the kinematic viscosity of water $\nu_{55^\circ C} = 0.511 \cdot 10^{-6}\,\frac{\text{m}^2}{s}$ (Kestin et al., 1978) the turbulent Rayleigh-Bénard convection can be characterized by the small-scale turbulence characteristics summarized in Table 6.3.

measurement	Re	$\eta_K [\mathrm{m}]$	$\tau_K [\mathrm{ms}]$	$u_K [\mathrm{mm/s}]$
Measurement#1	103	$3.3 \cdot 10^{-4}$	209	0.15
Measurement#2	128	$3.0 \cdot 10^{-4}$	174	0.17
Measurement#3	115	$3.2 \cdot 10^{-4}$	205	0.15
Measurement#4	115	$3.2 \cdot 10^{-4}$	204	0.16

Table 6.3: Turbulence characteristics and Kolmogorov microscales observed in the turbulent RB flow fields

6.3.2 Bichromatic Particle Streak Velocimetry Measurements

As visualized in Figure 6.5 on page 123, the hybrid bPSV approach that uses a bichromatic depth extraction (cf. Section 3.2) allows *three-dimensional three-component* (3D3C) measurements in a 10 mm thick boundary layer at the air-water interface of the generated turbulent RB convections.

This restriction to a thin measurement volume was achieved by using an E112 concentration of $12\,\mathrm{mg/l}$. It has to be pointed out that this is not the resolution limit of the measurement technique. By using higher concentrations of the absorbing dye, it would even be possible to restrict the measurement volume to a thinner volume-of-interest. In contrast to the plenoptic approach a fine resolution of the upper boundary layer using the bPSV technique is possible. The precision of these measurements can be estimated according to the preliminary considerations in Section 6.1. It amounts to $4\,\%$ of the penetration depth.

In the calibration measurements conducted previously to each measurement, this penetration depth was measured for each wavelength. For the violet light source $\lambda_1 = 405\,\mathrm{nm}$ at the used concentration of $12\,\mathrm{mg/l}$ it was found to be $9\,\mathrm{mm}$. This means that the precision of the depth estimate can be approximated to be $0.1\,\mathrm{mm}$. The precision of the horizontal information is even higher. This is because of the sub-pixel precise center-line extraction routine (cf. Chapter 5) and the relative small pixel size $\alpha = 0.03\,\mathrm{mm/px}$ of the camera (cf. Chapter 4). According to the considerations in Section 6.1, it is reasonable to approximate the measurement error in the horizontal directions by $10\,\%$ of α, i.e. $3 \cdot 10^{-3}\,\mathrm{mm/px}$.

In short it can be said that the resolution of the velocity information and the depth estimate are sufficient to resolve interfacial processes in the first centimeter of the air-water interface of the turbulent RB convection.
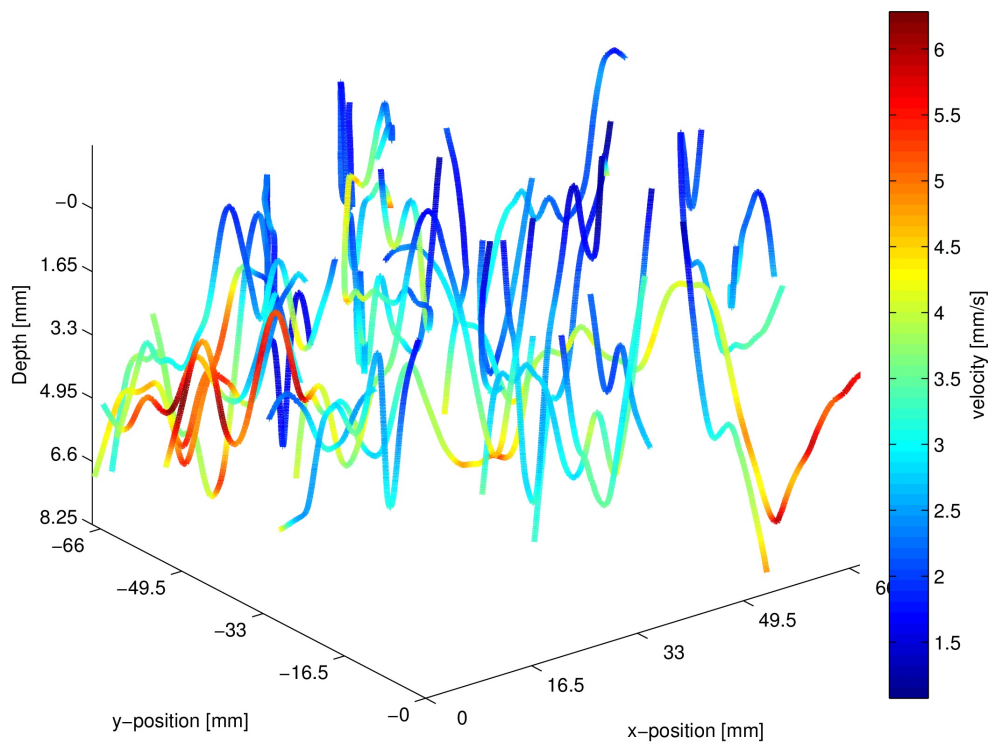
Figure 6.5: 3D bPSV trajectories measured in the turbulent RB convection characterized in Table 6.2 on page 120

6.3.3 Plenoptic Particle Streak Velocimetry Measurements

In all experiments that were performed by means of the *focused plenoptic camera*, E112 was used to block the light from deeper regions lying below the extended focal depth of the "all-in-focus" images (cf. Chapter 2). This strategy yields a significant improvement in the quality of the measured data sets since interfering reflections caused by particles in deeper regions were absorbed by the dye.

In the pPSV measurements that were performed to extract flow information from the turbulent RB convection, the horizontal dimensions of the measurement volume amount to 75 mm × 55 mm. As described in Section 6.1, the depth range of the used *focused plenoptic camera* is correlated with the horizontal dimensions of the measurement volume. Therefore, the depth range of the measurement volume was approx. 50 mm. The trajectories extracted from a short pPSV image-sequence are plotted in the right image of Figure 6.6 on page 125. With respect to the original aim of this thesis, i.e. the development of a measurement technique for the extraction of interfacial flow information, the fixed correlation between the depth range and the horizontal size of the measurement volume yields three major disadvantages.

- Although a restriction of the measurement volume to a thin layer in the interface would be possible by means of an absorbing dye, the relative precision of the depth estimate would still be approx. 6 % of the original depth range. This means, if we restricted the measurement shown in Figure 6.6 on page 125 to the upper 10 mm using a high E112 concentration in the liquid, there would still be an uncertainty of ±3 mm in the depth information.

- Due to the high depth range, the seeding density of the used tracer particles has to be reduced drastically. This is necessary to avoid multiple crossings of the measured particle streaks. These crossings would hamper the center-line extraction and reduce the number of valid streaks extracted from the images.

- Another shortcoming that is connected with the low seeding density is that it is impossible to compute Lagrangian multi-particle statistics from the recorded pPSV data. As explained in Chapter 2, these Lagrangian measures rely on pairs of particles or even clusters of multiple particles that have a small initial distance.

Since a characterization of interfacial processes on the basis of the presented pPSV technique is not possible due to the previously stated reasons, we focus on the data measured by means of the bPSV approach in the following extraction of Lagrangian turbulence statistics. These data were measured in a thin volume under the air-water interface of the turbulent RB convection with a high spatial and temporal resolution that enables the extraction of valid acceleration statistics. Furthermore, the bPSV technique allows to use seeding densities that enable the extraction of Lagrangian particle pair dispersion statistics.
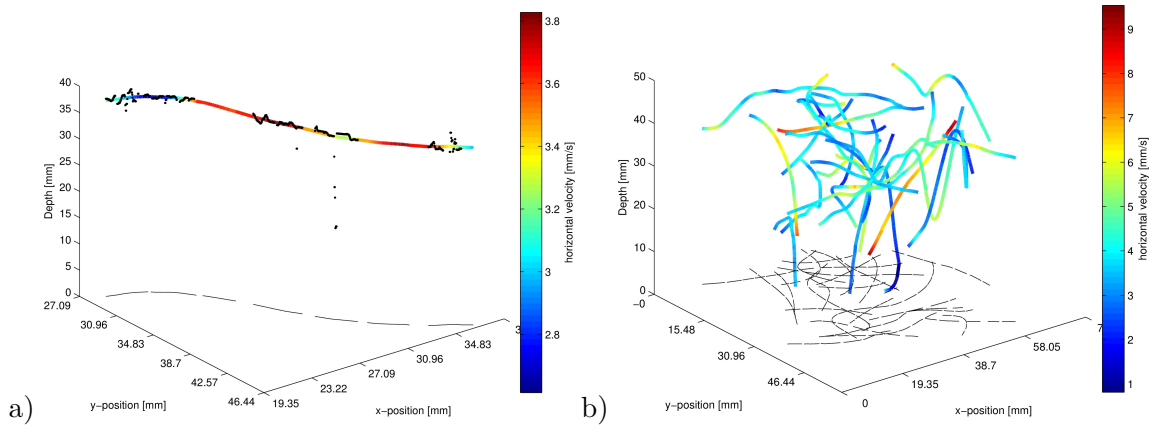
Figure 6.6: 3D pPSV trajectories of tracer particles with color-coded velocity information measured at the convection tank. The water surface in this experiment was at $z = 50\,\text{mm}$. The black lines show the horizontal information obtained from seven "all-in-focus" images. The depth information was obtained from the depth maps of a stereo algorithm. **a)** Single trajectory with black dots to show the sparse depth information that was interpolated by using a penalized smoothing spline. **b)** Example for a set of particle trajectories from a time interval of 6*s* at the convection experiment.

6.4 Lagrangian Statistics

This section focuses on the Lagrangian turbulence statistics that were computed from Lagrangian trajectories measured in the bPSV experiments on a turbulent RB convection.

To characterize the turbulent flow and to validate the applicability of the developed measurement technique, the single particle acceleration was evaluated and compared to two existing models that describe the acceleration distribution. Therefore, the *Probability Density Functions* (PDF)s of these models were fitted to the acceleration distributions of Lagrangian particle trajectories observed in the upper the centimeter of the air-water boundary layer in the turbulent RB convection. Additionally the three-dimensional Lagrangian two-particle dispersion was extracted from these trajectories. Both statistical turbulence characteristics were computed from large ensembles of Lagrangian particle trajectories. Each ensemble corresponds to one of the measurements summarized in Table 6.3 on page 122.

6.4.1 Lagrangian Acceleration Statistics

As already explained in detail in Section 2.1, Lagrangian acceleration statistics play an important role in turbulence characterization. This is mainly due to the fact that the
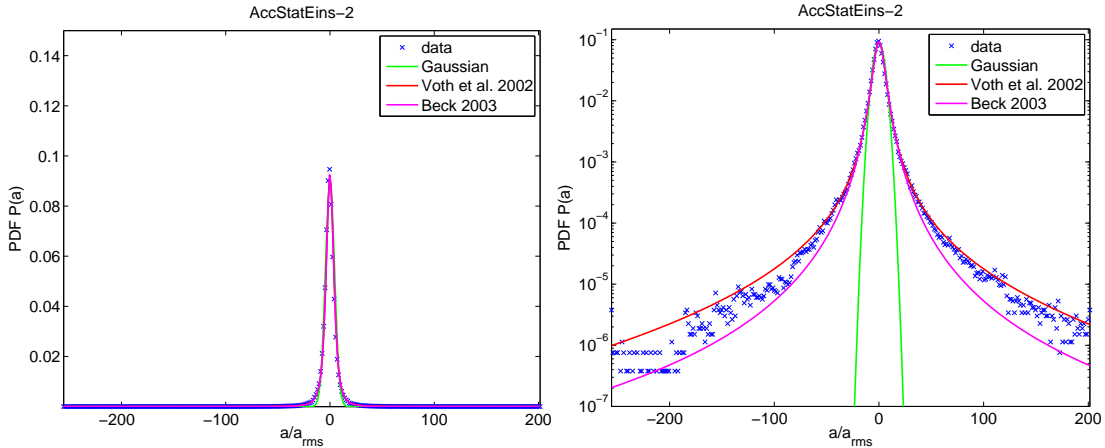
Figure 6.7: Lagrangian acceleration statistic of a single measurement. On the left hand side the data (blue dots), a normalized Gaussian bell-curve (green line) and the two model fits (red, magenta) are plotted in a regular spaced coordinate system. The right hand side shows the same data and the same fit in a semi-logarithmic plot.

acceleration directly enters the right hand side of the *Navier-Stokes equation* (NSE) described by Equation (2.8).

The Lagrangian particle acceleration statistics, presented in this section, were computed from the first temporal derivative of the instantaneous velocity signal of all particle trajectories recorded in the RB convection experiments. This velocity signal directly results from the frequency analysis of the periodic intensity patterns on the extracted particle streaks. The statistical evaluation was performed separately for each bPSV measurement series listed in Table 6.3 on page 122.

All four acceleration statistics were used to fit a Gaussian bell-curve and the two Lagrangian acceleration distribution models that are presented in Chapter 2. The first model fitted to the Lagrangian acceleration distribution was proposed by Voth et al. (2002) and is based on a phenomenological description of the observed distribution. As explained in Section 2.1, the model can be formulated by the *Probability Density Function* (PDF) given in Equation (2.12).
The second model is based on a theoretical derivation by Beck (2002, 2003) and was used by Aringazin and Mazhitov (2004) to formulate the model PDF of the second model (Equation (2.13)).
Both models were fitted by means of a non-linear least squares fit to the data that were extracted from the bPSV experiments.

The large range of the Lagrangian acceleration distributions requires a proper visualization to evaluate the quality of the different models. This is shown on the basis of a acceleration histogram extracted from *Measurement#1.* For a visual comparison the diagram on the left hand side of Figure 6.7 shows a conventional plot of the Lagrangian

acceleration distribution, a fitted normalized Gaussian bell-curve and the fitted model functions (2.12) and (2.13). The very same data are plotted by means of a semi-logarithmic plot in the diagram on the right hand side of this figure. Here it becomes clear that the quality of the model can only be judged by means of semi-logarithmic diagrams that also visualize the deviations at the tails of the distributions. While in the diagram on the left hand side, both models seem to fit the data equally well and the normalized Gaussian bell-curve seems to yield only a slight underestimation of the tails of the distribution, the semi-logarithmic plot on the right hand side shows the performance of the models in the lower probability range of the distribution.

Furthermore, it can be seen that the measured Lagrangian acceleration statistic is highly non-Gaussian. The figure shows that the distribution proposed by Voth et al. (2002) slightly overestimates the tails of the measured distribution while the model formulated by Beck (2002) and Aringazin and Mazhitov (2004) yields a slight underestimation.

Semi-logarithmic plots of the Lagrangian acceleration distributions extracted from all four interfacial bPSV measurement series (summarized in Table 6.3 on page 122) are shown in Figure 6.8 on page 128. Furthermore, this figure comprises the fits of normalized Gaussian bell-curves, and the PDFs of both Lagrangian acceleration distribution models. These plots show that both models can be used to describe the distribution down to very low probabilities.

The summary in Table 6.4 on page 129 gives an overview of the parametrization of the two models and the normalized Gaussian bell-curve computed by the non-linear least squares fit routine.

Here it can be seen that the width parameter σ from the phenomenological model by Voth et al. (2002) corresponds nicely with the width that results from the fit of a normalized Gaussian bell-curve. For the two parameters that model the non-Gaussian behavior of the tails of the distribution, we observed an accordance to the results observed by Voth et al. (2002) (i.e. $\beta = 0.539$ and $\gamma = 1.588$).

The parameters that were fitted by means of the theoretical model (2.13) show an underlying problem of this model. Due to the strong correlation of the model parameters and because of the existence of multiple locale minima in the parameter space, the result of the model fit relies strongly on the initialization. Especially the normalization parameter C and the parameter a_c that models the exponential decrease of the tails of the distribution rely strongly on each other. The large variations of the extracted parameters of the second model shown in Table 6.4 on page 129 are a result of this strong correlation between the model parameters and the vulnerability of the non-linear least squares fit on locale minima in the parameter space.

In short, it can be said that the acceleration distributions extracted from the flow fields in the free air-water interface of a turbulent RB convection comply nicely with the model PDF proposed by Voth et al. (2002) for isotropic turbulences. The extracted
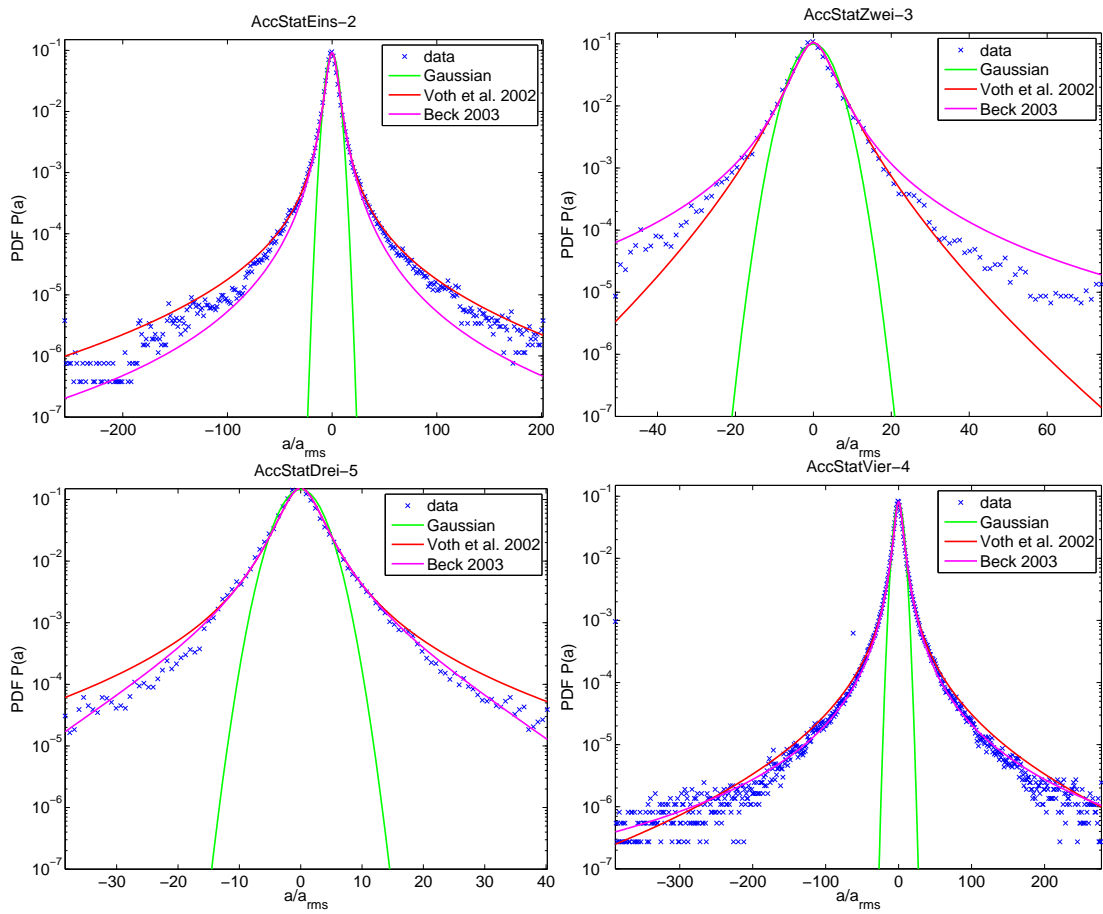
Figure 6.8: Separate fits of the Lagrangian acceleration models on the measured bPSV data sets. As indicated by the normalized Gaussian bell-curves (green lines), all four distributions are highly non-Gaussian. All the distributions are described well by the models down to probabilities of 10^{-5} to 10^{-6}.

Model/*Measurement*	Parameter			
Normalized Gaussian distribution	σ			
Measurement#1	4.4618			
Measurement#2	3.974			
Measurement#3	2.7228			
Measurement#4	5.1605			
Phenomenological model (Voth et al., 2002) (cf. Equation (2.12))	σ	C	β	γ
Measurement#1	4.5812	0.092881	0.47877	1.7015
Measurement#2	3.5306	0.10727	0.62658	1.3382
Measurement#3	2.7058	0.15361	0.50956	1.6209
Measurement#4	4.8774	0.081256	0.52887	1.6607
Theoretical distribution (Aringazin and Mazhitov, 2004; Beck, 2003)(cf. Equation (2.13))	a_c	C	n	β_0
Measurement#1	$2.12 \cdot 10^6$	50.9079	1.7445	0.046967
Measurement#2	15.423	2.3916	1.0927	0.06243
Measurement#3	30.9809	7.8304	1.5744	0.12952
Measurement#4	$4.71 \cdot 10^4$	15.5902	1.4673	0.040779

Table 6.4: Summary of the model parametrization estimated by a non-linear least squares fit from the measured Lagrangian acceleration statistics

model parameters are quite similar to those obtained in the experiments by Voth et al. (2002). Although the fit of the second model proposed on the basis of theoretical studies by Beck (2003) and Aringazin and Mazhitov (2004) seems to describe the measured Lagrangian acceleration distribution quite well, the resulting model parameters are unreliable. Because of the ill-posed model function that describes the PDF of the distribution, there may be multiple parameterizations yielding the same result. Furthermore, the model seems to comprise many local minima in the parameter space, so that a global optimum is very unlikely to be obtained by means of a non-linear least squares fit.

6.4.2 Lagrangian Particle-Pair Dispersion

In this section the results of the Lagrangian particle pair dispersion measurements recorded in the boundary layer of the turbulent RB convection are presented. This turbulence characteristic is defined by the mean squared average of the particle pair dispersion. As described in Chapter 2, it is computed by averaging large ensembles of Lagrangian particle pairs that were all seeded with a certain initial separation. In

this study the particle pairs were chosen from sets of Lagrangian trajectories that were extracted from the bPSV-measurements of the previously described RB convection.

Due to the definition of the Lagrangian particle pair dispersion, the only restriction is that for each particle pair there has to be a point in time t_0, when the particle distance is equal to a predefined initial separation r_0. The initial separation has to be within the *inertial subrange*. This subrange is defined by the range between the Kolmogorov microscale and the Lagrangian integral length scale $\eta_K \ll r_0 \ll L$ (cf. Chapter 2). A detailed description of the particle pair extraction routine used to obtain the data presented in this section is given in Chapter 5. For a characterization of the particle pair separation behavior, the evolution of the mean squared pair separation $\left\langle |\vec{r}(t) - \vec{r}_0|^2 \right\rangle_L$ is averaged over the whole ensemble.

Four particle pairs from the ensemble extracted from the *Measurement#4* are shown in Figure 6.9. In these images the 3d data of both member trajectories are visualized and the instantaneous velocity of the single particles is color-coded along the trajectories. As shown in these images, the movement at the "seeding point" $t = t_0$, when the particle distance is close to r_0, is quite correlated. Later in time this correlation of the particle movement vanishes. The scaling parameters of *Measurement#4* are summarized in Table 6.3 on page 122.

For a detailed description of the derivation and the meaning of this turbulence characteristic we refer to its introduction in Chapter 2. As described in this chapter, a common strategy to visualize the transition from the *Batchelor* regime to the *Richardson-Obukhov* (R-O) regime and from the R-O regime to the diffusive regime is to scale the mean squared pair separation with the factor t^{-3}. In a double logarithmic plot the scaled time evolution of the mean shows a t^{-1} slope in the *Batchelor* regime, a plateau in the R-O regime and a t^{-2} slope in the diffusive regime. According to the theory developed by Richardson (1926) and Batchelor (1950), this transition only occurs for ensembles with a small initial separation. Ensembles with larger initial separations don't show an intermediate *Batchelor* regime but a direct transition from the t^{-1} scaling to a t^{-2} scaling. This behavior was observed in all bichromatic measurements of the air-water interface summarized in Table 6.3 on page 122. The three regimes and the transitions for different initial separations are shown in Figure 6.10 on page 133.

In order to allow a comparison on the basis of a scale-invariant characterization, the time axis was scaled by means of the Kolmogorov time τ_K.

To enable a quantitative comparison of the observed transition, a measure is needed that allows a simple extraction of the position of the R-O regime. In this context we defined the center of the R-O regime t_{RO} to be at the position of the inflection point in the middle of the R-O regime. This point can easily be assessed from the particle pair dispersion curves that comprise a plateau of the R-O regime. The exact positions of these inflection points for different initial separations are summarized in Table 6.5 on page 132. This table contains the evaluation of all bPSV measurements that were
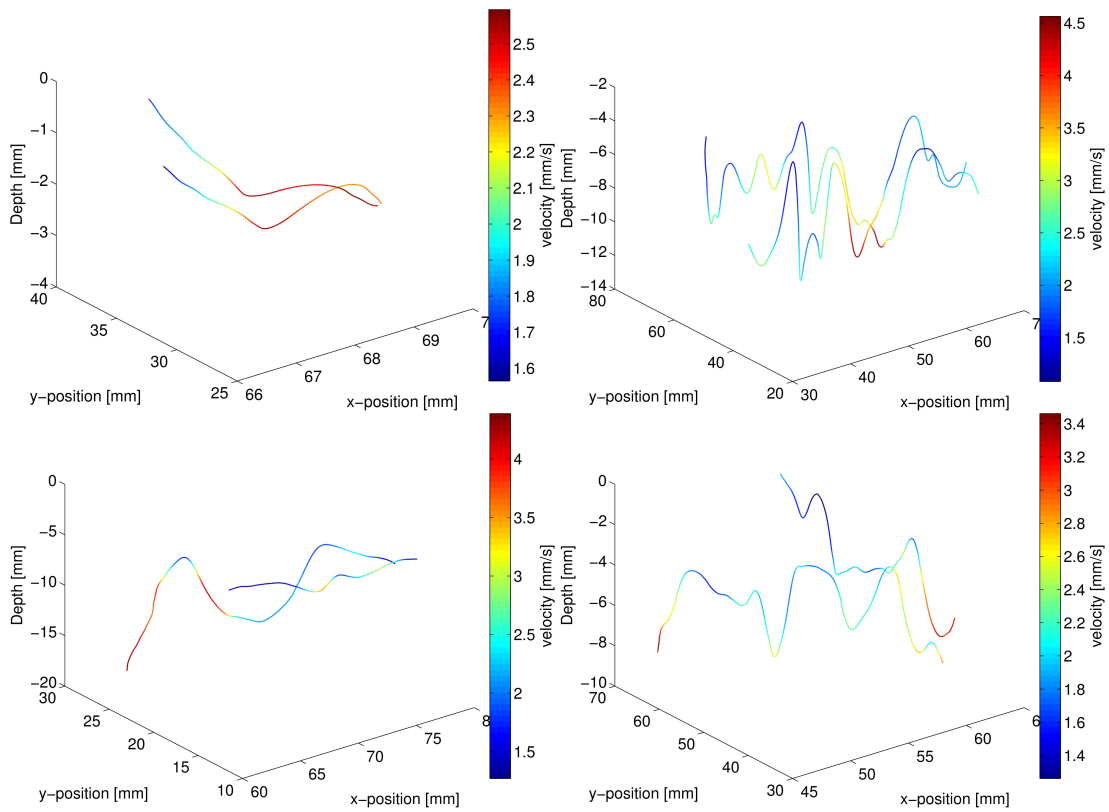
Figure 6.9: This figure contains four of the particle pairs extracted from *Measurement#4*. The color encodes the velocity information along the line. In these figures one can see that the particle movements at small times are correlated while the movements of the single particles at later times are quite individual.

taken in the air-water interface of the turbulent RB convection (cf. Table 6.3 on page 122). Since the plateau of the R-O regime can only be observed for small initial pair separations, it was not possible to extract the R-O regime time t_{RO} for ensembles that were extracted with large r_0 value.

The results shown in Table 6.5 on page 132 and Figure 6.10 on page 133 match nicely with the results published recently by Schumacher (2009) in a *direct numerical simulations* (DNS) study on convective turbulence in air. In this study the author observed a R-O regime in form of a plateau for initial separations between $r_0 = 0.5\,\eta_{\rm K}$ and $r_0 = 4\,\eta_{\rm K}$. At higher initial separations (i.e. $r_0 = 16\,\eta_{\rm K}$) no plateau was observed in the transition from the Batchelor t^{-1} regime to the diffusive t^{-2}. A similar behavior was also described in a recent review by Salazar and Collins (2009).

The transition points $t_{\rm RO}$ observed in the interfacial measurements in this study tend to be smaller than the times observed in literature. While the transition points that were observed in the measurements in this thesis lay in a time range between $1.0\,\tau_{\rm K}$ and $3.1\,\tau_{\rm K}$, the transitions observed by Salazar and Collins (2009) and Schumacher (2009) range between $10\,\tau_{\rm K}$ and $40\,\tau_{\rm K}$.

A possible reason for this shift of the transition points can be the fact that the simulations by Schumacher (2009) and the measurements that are summarized in the review by Salazar and Collins (2009) assume an isotropic turbulence. Since the measurements in this study are recorded in a highly anisotropic turbulence in the interfacial region of a boundary layer, an application of Kolmogorovs scaling theory might cause this kind of errors. Another much simpler explanation is the approximation of the Kolmogorov time scale made in this thesis. As described earlier in this chapter, the Kolmogorov time-scale had to be approximated from the *Reynolds number* because it was not possible to assess the energy dissipation rate from the measured data. Therefore, the approximation error of the Kolmogorov time-scale might be another plausible explanation for the observed shift of $t_{\rm R\text{-}O}$.

In conclusion of this section, it can be said that the three regimes described by Richardson (1926) and Batchelor (1950) for isotropic turbulences could also be measured in the anisotropic turbulence of an interface. A comparison with two recent studies showed that the initial separations at which a plateau of a R-O regime occurs are similar to those observed in literature. Furthermore, a shift of the transition point of the R-O transition was observed.

Measurement#1		*Measurement#2*		*Measurement#3*		*Measurement#4*	
r_0	t_{RO}	r_0	t_{RO}	r_0	t_{RO}	r_0	t_{RO}
$3.64\eta_K$	$1.11\tau_K$	$5.01\eta_T$	$1.10\tau_K$	$3.75\eta_K$	$1.54\tau_K$	$3.75\eta_K$	$1.97\tau_K$
$4.55\eta_K$	$1.03\tau_K$	$6.0\eta_T$	$0.87\tau_K$	$4.69\eta_K$	$2.26\tau_K$	$4.69\eta_K$	$2.19\tau_K$
$6.36\eta_K$	$1.32\tau_K$	$6.95\eta_T$	$1.01\tau_K$	$5.63\eta_K$	$2.79\tau_K$	$5.63\eta_K$	$3.31\tau_K$
$9.10\eta_K$	NA	$8.08\eta_T$	NA	$14.06\eta_K$	NA	$7.5\eta_K$	NA

Table 6.5: Overview over the extracted Lagrangian particle pair dispersion statistic. In the extraction the mean squared particle separation of Lagrangian trajectories was computed for different initial separations. For each measurement four initial separations were tested that lie in the *inertial subrange*. NA entries indicate that no clear transition between the three regimes was observed.
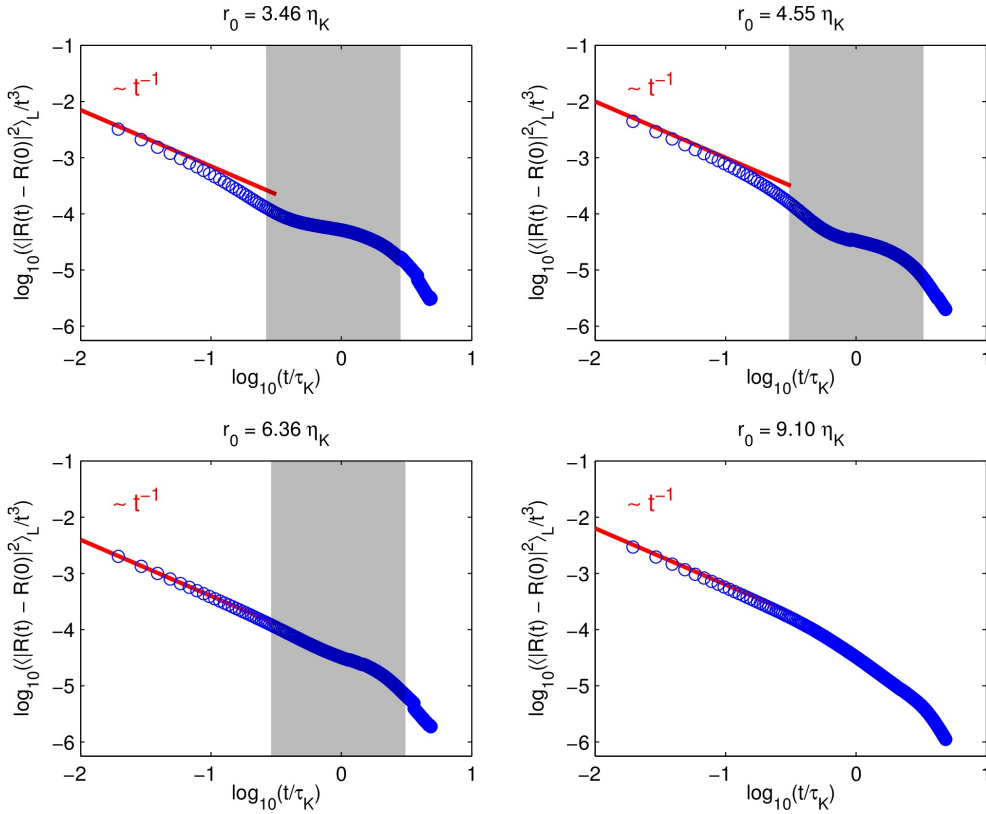
Figure 6.10: Visualization of the 3D pair dispersion of the data set *Measurement#1*. The particle pair dispersion was plotted as a function of the time scaled with the Kolmogorov time scale for four initial pair separations ($R(0) = 3.46\eta_K, 4.55\eta_K, 6.36\eta_K, 9.1\eta_K$). The data were normalized by the factor t^{-3}. The dissipation subrange corresponds to the $\sim t^{-1}$ part, the inertial subrange (gray labeled area) is represented by the plateau in the curves of small inertial pair separation $R(0)$, followed by the diffusion subrange.

7 Conclusion

This thesis describes two particle streak based measurement techniques purpose-built for Lagrangian *three-dimensional three-component* (3D3C) measurements of flow characteristics in the interfacial region of a transparent boundary layer. It contains a thorough description of the implemented measurement setups and a detailed characterization of the techniques with an estimation of precision that can be achieved by the presented methods.

Furthermore, this thesis successfully applied both techniques to measure turbulent flow fields in a *Rayleigh-Bénard* (RB) convection. On the basis of these measurements several turbulence characteristics were extracted. The comparison of these measures, taken in the anisotropic interfacial region, shows good agreements with theoretical predictions for isotropic turbulence and recent experimental studies and therefore proves the applicability of the method. To the best of our knowledge such a verification of theoretical predictions in the interfacial region has not been conducted previously.

Both developed measurement techniques rely on the *Particle Streak Velocimetry* (PSV) measurement principle that uses long time exposures of a single camera setup to record blurred streak structures caused by the reflections of neutrally buoyant tracer particles moving with the fluid. To overcome the loss of temporal resolution caused by the integration in the long time exposure images, a periodically modulated illumination is used coding temporal information into the PSV images. By analyzing the spatial frequency of the gray-value signal along the particle streaks, both methods extract the instantaneous particle velocity along the individual trajectories.

The two developed measurement techniques can be distinguished by the depth estimation strategy that is used to assess *three-dimensional* (3d) information. The first technique was named *bichromatic Particle Streak Velocimetry* (bPSV). It relies on an absorption-based approach that uses an absorbing dye and a two-wavelength illumination to resolve the depth of individual tracer particles below the interface. This approach was already presented to the scientific community in two conference contributions (Voss and Garbe, 2010; Voss et al., 2010).

Due to a sub-pixel precise particle streak extraction routine both presented methods provide a continuous spatial description of the particle trajectories with a very high precision comparable to the precision obtained by state of the art 3d *Particle Tracking Velocimetry* (PTV) approaches. In contrast to current PTV measurements that determine particle positions at discrete times and compute velocities from the particle displacements, the presented PSV methods enable the measurement of continuous

particle velocity signals. The extraction of a dense sampled velocity especially pays off when it comes to the extraction of particle accelerations that can simply be computed from the first temporal derivative of the instantaneous velocity signal.

In the context of interfacial measurements the bichromatic PSV technique clearly outperforms the plenoptic method because the plenoptic approach is restricted to a fixed ratio between the horizontal measurement range and the depth range. Therefore, it is infeasible to achieve high resolutions in a thin interfacial layer by means of the *plenoptic Particle Streak Velocimetry* (pPSV) approach. Nonetheless, this method presents an appropriate alternative to state-of-the-art 3D3C PTV approaches. In contrast, the bPSV technique can be easily adapted for measurements in thin boundary layers by adjusting the concentration of the dye used. Since the precision of the depth estimate is relative to the penetration depth of the light, it is possible to extract interfacial information with a very high depth resolution. Another advantage of the bPSV technique is that it directly measures data relative to the position of the interface. This makes an additional tracking as used in other interfacial measurement techniques dispensable and reduces the error associated with such an approach.

Additionally, the developed techniques were used in a set of characterization experiments that aimed for the extraction of Lagrangian flow statistics from a turbulent RB convection. Due to its better interfacial resolution the results of the bPSV measurements were used to extract Lagrangian acceleration statistics and Lagrangian two-particle dispersion statistics. A comparison of the extracted acceleration statistics from the boundary layer of the turbulent air-water interface with a phenomenological model proposed by Voth et al. (2002) and a theoretically motivated model by Beck (2003) and Aringazin and Mazhitov (2004) showed very good agreements. A direct analysis of the obtained model parameters showed nice correspondences with the experimental results published by Voth et al. (2002). Due to the ill-posed model *Probability Density Function* (PDF) in the theoretical approach (Aringazin and Mazhitov, 2004) no meaningful parameters could be extracted from this model.

In the Lagrangian particle pair dispersion statistics of the interfacial region the theoretical predicted transitions from the small scale *Batchelor* regime to the *Richardson-Obukhov* (R-O) regime and from the R-O regime to the diffusive regime were observed. The center of the intermediate R-O estimated from the average of the measured Lagrangian pair dispersion measurements could be extracted for initial pair separations below $6.95\,\eta_K$. This result matches with the results published by Schumacher (2009), who observed an R-O regime for initial pair separations smaller than $4\,\eta_K$. For higher initial separations we observed a transition from a *Batchelor* regime to a diffusive regime that was also recorded by Schumacher (2009). The temporal position of the observed R-O regimes tend to be smaller compared to the times observed in the experiments summarized by (Salazar and Collins, 2009). An appropriate reason for this deviation might be the anisotropic nature of the observed interfacial flow field.

Due to the high spatial precision and the reliable intensity extraction of the imple-

mented particle streak extraction routine the approach was also sucessfully applied to the analysis of data from cell-biology (Herzog et al., 2012). In this study the intensity profiles along rod shaped cells obtained in fluorescence microscopic measurements were extracted to analyze the concentration distribution of fluorophore-tagged proteins along the cell spine.

7.1 Outlook

Although the original aim, i.e. the development of an interfacial measurement technique for the estimation of Lagrangian 3D3C flow characteristics was reached, there is still room for refinements. In this context automating the calibration measurement that has to be performed previously to each bPSV measurement would drastically alleviate the usability of this method.

Furthermore, the dependency of the presented Lagrangian characteristics on various boundary conditions such as viscosity, *Rayleigh number* or aspect ratio could be analyzed in the turbulent boundary layer region of RB convections.

A challenge that has not been addressed in the this thesis is the measurement of mobile wave-influenced air-water surfaces. In this context reflections at the mobile interface present a major challenge that needs to be solved to extend the applicability to moving interfaces.

Additionally, the particle streak extraction algorithm could be improved by a routine that allows the identification and extraction of crossing particles. With such a routine it would be possible to measure flow fields with much higher particle seeding densities. These higher densities would allow the measurement of dynamical Lagrangian characteristics in unsteady flow fields because shorter time ranges could be taken into account in the averaging.

Another extension that would help to establish the presented methods in the field of particle-based measurement techniques is the development of a *Graphical User Interface* (GUI) for an easy application of the implemented routines in the laboratory environment.

Furthermore, it would be possible to implement a novel measurement technique by measuring PSV data of a fluid seeded with particles that are coated with a *Temperature Sensitive Paint* (TSP). Such a TSP-PSV hybrid approach would profit from the high reliability of the extracted intensities and from the high temporal resolution that can be achieved.

Acronyms

Nomenclature

α_{i} Isobaric thermal expansion coefficient, page 10

α_h Hamming window function coefficient, see equation (5.38), page 96

α_{mie} Dimensionless Mie parameter, see equation (3.12), page 38

$\Delta z(I_1, I_2)$ Error of the bichromatic depth estimate

ϵ_i Extinction coefficient of the absorbing dye for the Wavelength λ_i

$\eta(\lambda)$ Total quantum efficiency, see equation (5.1), page 75

η_{K} Kolmogorov length scale, see equation (2.4), page 11

$\hat{\mathcal{S}}$ A set of streak-lists that correspond to a PSV image sequence, page 100

$\hat{\mathcal{T}}$ A set of trajectories called trajectory-list, page 100

λ Wavelength

λ_i Wavelength of the light sources used for the intensity modulated illumination

$\langle \epsilon \rangle$ Energy dissipation, see equation (2.3), page 11

$\langle \vec{r}(t) \rangle_L$ Averaged Lagrangian pair separation statistic, see equation (2.20), page 16

$\mathbf{B}_k$ Temporal median computed for image $\mathbf{I_k}$, see equation (5.27), page 86

$\mathcal{B}$ Boundary Tensor, see equation (5.33), page 89

$\mathcal{H}_t\left(X\left(c\right)\right)$ Hilbert transform of the spatial signal $X(c)$, see equation (3.24), page 45

$\mathcal{J}$ Three dimensional, spatiotemporal structure tensor, see equation (5.29), page 88

$\mathcal{J}$ *Three-Dimensional* (3D) *Structure tensor*, see equation (5.30), page 88

$\mathcal{S}_i$ A single streak-list in a set of streak-lists, page 100

$\mathcal{T}_k$ Single trajectory in a trajectory-list, page 100

μ_e Number of electrons, page 75

μ_p Number of photons that hit a single pixel of a *charge-coupled device* (CCD) detector during the exposure, see equation (5.2), page 75

μ_y Digital gray-value of a pixel [DN], see equation (5.3), page 76

$\mu_{e.\mathrm{sat}}$ Saturation capacity of the image sensor pixels, see equation (5.19), page 81

$\mu_{y.50}$ Mean pixel gray-value extracted from $50\,\%$ saturated images, see equation (5.21), page 83

$\phi\,(c)$ Instantaneous phasing of a spatial signal

Φ_R Radiant flux of the *light-emitting diode* (LED) array, see equation (4.1), page 64

σ_d^2 Sensor noise produced during the readout and the camera-intern amplification [*digital number* (DN)], page 77

σ_e^2 *Shot Noise:* Variance of quantum mechanical fluctuations of the number of electrons induced in the imaging sensor [DN], page 77

σ_q^2 Image noise generated by the quantization in the *analog digital converter* (ADC) [DN], page 77

σ_y^2 Complete noise as determined by the noise model proposed in the EMVA1288 standard [DN], see equation (5.7), page 77

$\sigma_{y.\mathrm{sat}}$ Saturation gray-value of the imaging system, page 77

τ_{K} Kolmogorov time scale, see equation (2.5), page 11

DSNU_{1288} *Dark Signal Non-Uniformity* (DSNU) value defined by the *European Machine Vision Association* (EMVA)1288 standart, see equation (5.25), page 84

L^{p} Lebesgue spaces, page 46

PRNU_{1288} *Photo Response Non-Uniformity* (PRNU) value defined by the EMVA1288 standart, see equation (5.25), page 84

$\tilde{\mathbf{I}}_k(i, j)$ Image k from an image-stack. (i, j) describes the pixel position within the image, page 86

$\tilde{H}$ Height of the water surface in the RB vessel

$\vec{v}(t)$ Time dependent 3d velocity vector of a tracer-particle in a Lagrangian trajectory

$\vec{x}(t)$ Time dependent 3d position of a tracer-particle in a Lagrangian trajectory

$a(t)$ Instantaneous amplitude of a spatial signal, see equation (3.25), page 46

c Speed of light [m/s]

C_D Drag coefficient, see equation (3.2), page 36

$d_e\left(\cdot,\cdot\right)$ Euclidean distance metric, see equation (3.31), page 57

E Irradiance on the CCD-array [W/m²], page 75

$E_{boundary}$ Boundary Energy, see equation (5.34), page 90

E_{edge} Edge Energy, see equation (5.34), page 90

$E_{junction}$ Junction Energy, see equation (5.34), page 90

$f(c)$ Spatial frequency extracted along the center-line of a streak structure, see equation (3.26), page 46

g Gravitational acceleration, page 10

$G(x)$ Gray-value signal extracted along the streaks center-line

h Planck's constant [Js]

$I(z,\lambda_i)$ Intensity signal a particle in the dyed fluid at the depth z, illuminated with the wavelength λ_i

J_1 First order Bessel Function, page 39

K Overall system gain of an imaging system [DN/e⁻], page 76

P_{therm} Thermal power of the LED array, see equation (4.1), page 64

R Quality measure of the extracted trajectories, Large R-values indicate errors in the velocity estimation, see equation (5.49), page 104

Ra Dimensionless Rayleigh Number, see equation (2.1), page 10

Re Dimensionless Reynolds Number, see equation (2.2), page 10

$s_{y.50}^2$ Spatial variance of the *Photo Response Non-Uniformity* (PRNU)-signal, see equation (5.23), page 84

$s_{y.\text{dark}}^2$ Spatial variance of the *Dark Signal Non-Uniformity* (DSNU)-signal, see equation (5.23), page 84

t_b Batchelor time, see equation (2.26), page 18

T_L Lagrangian integral time scale, page 18

t_{exp} Exposure time [s], page 75

t_{RO} Center of the *Richardson-Obukhov* (R-O) regime

u_{K} Kolmogorov velocity scale, see equation (2.6), page 11

$v_h(c)$ Horizontal particle velocity as a function of the position on the center-line, see equation (3.18), page 41

$w(c)$ Hamming window function $w(n) : \mathbb{N} \to \mathbb{R}$, see equation (5.38), page 96

$Z(c)$ Spatial analytic signal, see equation (3.23), page 45

SNR   Signal to noise ratio, see equation (5.12), page 79

DR   Dynamic Range of the sensor array in the used imaging device , see equation (5.17), page 80

List of Figures

List of Tables

8 Bibliography

Adamczyk, A. and Rimai, L. 2-Dimensional particle tracking velocimetry (PTV): Technique and image processing algorithms. *Experiments in Fluids*, 6:373–380, 1988.

Adelson, Edward H. and Wang, John Y. A. Single lens stereo with a plenoptic camera. *IEEE Transactions on Pattern Analysis and Machine Intelligence*, 14:99–106, 1992.

Adrian, R.. Particle-imaging techniques for experimental fluid mechanics. *Annual Review of Fluid Mechanics*, 23:261–304, 1991.

Adrian, R. Twenty years of particle image velocimetry. *Experiments in Fluids*, 39:159–169, 2005. doi: 10.1007/s00348-005-0991-7.

AEON Verlag & Studio Walter H. Dorn e.K., . heurisko: Development environment and tools for digital image processing. Web Page, January 2012. URL `http://www.heurisko.de/`.

Ahlers, G.; Grossmann, S., and Lohse, D. Heat transfer and large scale dynamics in turbulent Rayleigh-Bénard convection. *Reviews of Modern Physics*, 81(2):503, 2009.

Akimoto, S.; Mitsumata, M.; Sasaguri, T., and Yoshida, Y. Laminar shear stress inhibits vascular endothelial cell proliferation by inducing cyclin-dependent kinase inhibitor p21sdi1/cip1/waf1. *Circulation research*, 86(2):185–190, 2000.

Aringazin, A. K. and Mazhitov, M. I. Stochastic models of lagrangian acceleration of fluid particle in developed turbulence. *International Journal of Modern Physics B*, 18:3095–3168, 2004. doi: 10.1142/S0217979204026433.

Arroyo, MP and Greated, CA. Stereoscopic particle image velocimetry. *Measurement Science and Technology*, 2:1181, 1991.

Banner, M. L. and Peirson, W. L. Tangential stress beneath wind-driven airwater interfaces. *Journal of Fluid Mechanics*, 364:115–145, 1998.

Barnhart, D.H.; Adrian, R.J., and Papen, G.C. Phase-conjugate holographic system for high-resolution particle-image velocimetry. *Applied Optics*, 33(30):7159–7170, 1994.

Batchelor, G. K. The application of the similarity theory of turbulence toatmospheric diffusion. *Quarterly Journal of the Royal Meteorological Society*, 76(328):133–146, 1950. ISSN 1477-870X. doi: 10.1002/qj.49707632804. URL `http://dx.doi.org/10.1002/qj.49707632804`.

Beck, C. Generalized statistical mechanics and fully developed turbulence. *Physica A: Statistical Mechanics and its Applications*, 306:189–198, 2002.

Beck, C. Lagrangian acceleration statistics in turbulent flows. *EPL (Europhysics Letters)*, 64: 151, 2003.

Berthe, A.; Kondermann, D.; Jähne, B., and Ketzscher, U. The wall piv measurement technique for near wall flow fields in biofliud mechanics. In Nitsche, W. and Dobriloff, C., editors, *Imaging Measurement Methods for Flow Analysis, Results of the DFG Priority Programme 1147 Imaging Measurement Methods for Flow Analysis 2003-2009*, volume 106 of *Notes on Numerical Fluid Mechanics and Multidisciplinary Design*, pages 11–20. Springer, 2009. doi: 10.1007/978-3-642-01106-1.

Berthe, A.; Kondermann, D.; Christensen, C.; Goubergrits, L.; Garbe, C.; Affeld, K., and Kertzscher, U. Three-dimensional, three-component wall-piv. *Experiments in Fluids*, 48: online, 2010. doi: 10.1007/s00348-009-0777-4.

Bishop, T. and Favaro, P. Full-resolution depth map estimation from an aliased plenoptic light field. *Computer Vision–ACCV 2010*, pages 186–200, 2011.

Biswas, G. *Introduction to fluid mechanics and fluid machines*. Tata McGraw-Hill Education, 2003.

Biwole, Pascal Henry; Yan, Wei; Zhang, Yanhui, and Roux, Jean-Jacques. A complete 3D particle tracking algorithm and its applications to the indoor airflow study. *Measurement Science and Technology*, 20(11):115403, 2009. ISSN 0957-0233. doi: 10.1088/0957-0233/20/11/115403. URL `http://iopscience.iop.org.ubproxy.ub.uni-heidelberg.de/0957-0233/20/11/115403`.

Bochkanov, Sergey. Alglib, 2010. `http://mloss.org/software/view/231/`.

Boffetta, G.; Celani, A.; Cencini, M.; Lacorata, G., and Vulpiani, A. Nonasymptotic properties of transport and mixing. *Chaos*, 10(1):50–60, 2000.

Brücker, Ch. Digital-particle-image-velocimetry (dpiv) in a scanning light-sheet: 3D starting flow around a short cylinder. *Experiments in Fluids*, 19:255–263, 1995.

Brücker, Ch. 3D PIV via spatial correlation in a color-coded light-sheet. *Experiments in Fluids*, 21:312–314, 1996.

Burgmann, S.; Dannemann, J., and Schröder, W. Time-resolved and volumetric piv measurements of a transitional separation bubble on an sd7003 airfoil. *Experiments in Fluids*, 44: 609–622, 2008. ISSN 0723-4864. URL `http://dx.doi.org/10.1007/s00348-007-0421-0`. 10.1007/s00348-007-0421-0.

Butler, P.J.; Norwich, G.; Weinbaum, S., and Chien, S. Shear stress induces a time-and position-dependent increase in endothelial cell membrane fluidity. *American Journal of Physiology-Cell Physiology*, 280(4):C962–C969, 2001.

Cenedese, A. and Paglialunga, A. A new technique for the determination of the third velocity component with piv. *Experiments in Fluids*, 8:228–230, 1989. ISSN 0723-4864. URL `http://dx.doi.org/10.1007/BF00195799`. 10.1007/BF00195799.

Chapman, Barbara; Jost, Gabriele, and Pas, Ruud van der. *Using OpenMP: Portable Shared Memory Parallel Programming (Scientific and Engineering Computation)*. The MIT Press, 2007. ISBN 0262533022, 9780262533027.

Cho, Young I. and Greene, George A. *Advances in heat transfer*, volume 43. ELSEVIER, 2011. ISBN 978-0-12-381529-3.

Corrsin, S. Heat transfer in isotropic turbulence. *Journal of Applied Physics*, 23(1):113–118, 1952.

De Boor, C. *A practical guide to splines*, volume 27. Springer Verlag, 2001.

Debaene, P. *Neuartige Messmethode zur zeitlichen und örtlichen Erfassung der wandnahen Strömung in der Biofluidmechanik.* Phd thesis, TU Berlin, 2005.

Debaene, P.; Kertzscher, U.; Gouberits, I., and Affeld, K. Visualization of a wall shear flow. *Journal of Visualization*, 8(4):305–313, 2005.

Dickey, T. D.; Hartman, B.; Hurst, E., and Isenogle, S. Measurement of fluid flow using streak photography. *American Journal of Physics*, 52:216–219, March 1984. doi: 10.1119/1.13695.

Dimotakis, P. E.; Debussy, F. D., and Koochesfahani, M. M. Particle streak velocity field measurements in a two-dimensional mixing layer. *Physics of Fluids*, 24:995–999, June 1981. doi: 10.1063/1.863481.

Dinkelacker, F.; Schäfer, M.; Ketterle, W.; Wolfrum, J.; Stolz, W., and Köhler, J. Determination of the third velocity component with PTA using an intensity graded light sheet. *Experiments in Fluids*, 13:357–359, 1992. ISSN 0723-4864. URL http://dx.doi.org/10.1007/BF00209511. 10.1007/BF00209511.

Dixon, Lisa; Cheong, Fook C., and Grier, David G. Holographic particle-streak velocimetry. *Opt. Express*, 19(5):4393–4398, Feb 2011. doi: 10.1364/OE.19.004393. URL http://www.opticsexpress.org/abstract.cfm?URI=oe-19-5-4393.

Dring, RP. Sizing criteria for laser anemometry particles. *ASME, Transactions, Journal of Fluids Engineering*, 104:15–17, 1982.

Durbin, PA. A stochastic model of two-particle dispersion and concentrationfluctuations in homogeneous turbulence. *Journal of Fluid Mechanics*, 100(2):279–302, 1980.

EFSA, . Wissenschaftliches Gutachten zur Neubewertung von Tartrazin (E102). *European Food Safety Authority (EFSA)*, November 2009. doi: 10.2903/j.efsa.2009.133.

Einstein, A. and others, . The foundation of the general theory of relativity. *Annalen der Physik*, 49(769-822):31, 1916.

Elsinga, G. E.; Scarano, F., and Wieneke, B. Tomographic particle image velocimetry. *Experiments in Fluids*, 41:933–947, 2006.

EMVA, . *EMVA Standard 1288 - Standard for Characterization of Image Sensors and Cameras.* European Machine Vision Association, release 3.0 edition, November 2010.

ENFIS Ltd., . Enfis uno tile array blue 465nm. Data Sheet, July 2008a. URL http://www.enfis.com/files/Uno-Tile%20Blue.pdf.

ENFIS Ltd., . Enfis uno tile array violet 405nm. Data Sheet, July 2008b. URL http://www.enfis.com/files/Uno-Tile%20Violet.pdf.

Fage, A. and Townend, H. C. H. An examination of turbulent flow with an ultramicroscope. *Proceedings of the Royal Society of London. Series A*, 135(828):656–677, 1932. doi: 10.1098/rspa.1932.0059. URL http://rspa.royalsocietypublishing.org/content/135/828/656.short.

Felsberg, M. and Sommer, G. The monogenic signal. *IEEE Transactions on Signal Processing*, 49:3136–3144, 2001.

Fouras, A.; Lo Jacono, D., and Hourigan, K. Target-free stereo piv: a novel technique with inherent error estimation and improved accuracy. *Experiments in Fluids*, 44(2):317–329, 2008.

Gabor, D. Theory of communication. *Journal of the Institute of Electrical Engineers Part III*, 93:429–457, 1946.

Garbe, C. S.; Schimpf, U., and Jähne, B. A surface renewal model to analyze infrared image sequences of the ocean surface for the study of air-sea heat and gas exchange. *Journal of Geophysical Research-Oceans*, 109(C8):1–18, 2004. ISSN 0148-0227. doi: doi:10.1029/2003JC001802.

Georgiev, T. and Lumsdaine, A. Focused plenoptic camera and rendering. *Journal of Electronic Imaging*, 19:021106, 2010.

Gerrard, A. and Burch, J.M. *Introduction to matrix methods in optics*. Dover Publications, 1994.

Grant, I. Particle image velocimetry: A review. In *Proceedings of the Institution of Mechanical Engineers*, volume 211 of C, pages 55–76, 1997.

Grothe, RL and Dabiri, D. An improved three-dimensional characterization of defocusing digital particle image velocimetry (ddpiv) based on a new imaging volume definition. *Measurement Science and Technology*, 19:065402, 2008.

Hanjalić, Kemal and Launder, Brian. *Modelling Turbulence in Engineering and the Environment*. Cambridge University Press, 2011.

Harris, F. J. On the use of windows for harmonic analysis with the discrete fourier transform. In *Proceedings of the IEEE*, volume 66-1, January 1978.

Hastie, T. *The Elements of Statistical Learning. Data Mining, Inference, and Prediction*. Springer Verlag, 2003.

Haußecker, H.; Spies, H., and Jähne, B. Tensor-based image sequence processing techniques for the study of dynamical processes. In *Proc. Intern. Symp. On Real-time Imaging and Dynamic Analysis*, pages 704–711, Hakodate, Japan, 1998. International Society of Photogrammetry and Remote Sensing, ISPRS, Commision V.

Herzog, Alexandra G.; Voss, Björn; Keilberg, Daniela; Sogaard-Andersen, Lotte; Garbe, Christoph S., and Kostina, Ekaterina A. Cipsa: Cellular intensity profile extraction as an extension of streak analyzer. *Journal of Structural Biology*, 2012. submitted.

Hinsch, K. D. Holographic particle image velocimetry. *Measurement Science and Technology*, 13:R61–R72, 2002.

Hoyer, K.; Holzner, M.; Lüthi, B.; Guala, M.; Liberzon, A., and Kinzelbach, W. 3D scanning particle tracking velocimetry. *Experiments in Fluids*, 39:923–934, 2005. doi: 10.1007/s00348-005-0031-7.

Huang, N. E.; Long, S. R., and Zheng, S. The mechanism for frequency downshift in nonlinear wave evolution. *Advances in Applied Mechanics*, 32:59, 1996.

Huang, N. E.; Shen, Z., and Long, S. R. A new view of nonlinear water waves. *Annual Review of Fluid Mechanics*, 31:417–457, 1999.

Huang, N.E.; Shen, Z.; Long, S.R.; Wu, M.C.; Shih, H.H.; Zheng, Q.; Yen, N.C.; Tung, C.C., and Liu, H.H. The empirical mode decomposition and the hilbert spectrum fornonlinear and non-stationary time series analysis. *Proceedings of the Royal Society of London. Series A:Mathematical, Physical and Engineering Sciences*, 454(1971):903, 1998.

Irvine Jr, T.F. and Duignan, M.R. Isobaric thermal expansion coefficients for water over largetemperature and pressure ranges. *International communications in heat and mass transfer*, 12(4):465–478, 1985.

Janesick, J.R. CCD characterization using the photon transfer technique. In Prettyjohns, K. and Derenlak, E., editors, *Solid State Imaging Arrays*, volume 570, pages 7–19. SPIE Proc., 1985.

Jehle, M. *Spatio-temporal analysis of flows close to water surfaces.* Dissertation, IWR, Fakultät für Physik und Astronomie, Univ. Heidelberg, 2006. URL `http://www.ub.uni-heidelberg.de/archiv/7060/`.

Jehle, M. and Jähne, B. A novel method for three-dimensional three-component analysis of flow close to free water surfaces. *Experiments in Fluids*, 44:469–480, 2008. doi: 10.1007/s00348-007-0453-5.

Jeys, T.H.; Herzog, W.D.; Hybl, J.D., and R.N.and SanchezCzerwinski, A. Advanced trigger development. *Lincoln Laboratory Journal*, 17(1):29–62, 2007.

Jullien, M.C.; Paret, J., and Tabeling, P. Richardson pair dispersion in two-dimensional turbulence. *Physical review letters*, 82(14):2872–2875, 1999.

Jähne, Bernd. *Digital Image Processing.* Springer, Berlin, 6 edition, 2005. doi: 10.1007/3-540-27563-0.

Kertzscher, U.; Berthe, A.; Goubergrits, L., and Affeld, K. Particle image velocimetry of a flow at a vaulted wall. *Proceedings of the Institution of Mechanical Engineers, Part H: Journal of Engineering in Medicine*, 222(4):465–473, 2008.

Kestin, J.; Sokolov, M., and Wakeham, W. A. Viscosity of liquid water in the range - 8°c to 150°c. *Journal of Physical and Chemical Reference Data*, 7:941–948, 1978.

Kim, M.C.; Nam, J.H., and Lee, C.S. Near-wall deposition probability of blood elements as a new hemodynamic wall parameter. *Annals of biomedical engineering*, 34(6):958–970, 2006.

Kunz, Jakob. Visualisierung der wasserseitigen massengrenzschicht beim konvektionsgetriebenen gasaustausch mithilfe einer lumineszenzmethode und thermografie. Bachelor thesis, Institut für Umweltphysik, Fakultät für Physik und Astronomie, Univ. Heidelberg, 2011.

Kähler, C.J. and Kompenhans, J. Fundamentals of multiple plane stereo particle image velocimetry. *Experiments in Fluids*, 29:70–77, 2000.

Köthe, U. *Generische Programmierung für die Bildverarbeitung.* PhD thesis, Universität Hamburg, 2000.

Köthe, U. and Felsberg, M. Riesz-transforms versus derivatives: On the relationship between the boundary tensor and the energy tensor. In Kimmel,R., ; Sochen, N., , and Weickert, J., , editors, *Scale Space and PDE Methods in Computer Vision*, pages 179–191, Berlin, 2005. Springer. URL `http://kogs-www.informatik.uni-hamburg.de/koethe/papers/abstracts/GEToperator.html`.

Köthe, Ullrich. Low-level feature detection using the boundary tensor. In *Visualization and Processing of Tensor Fields*, pages 63–79. 2006.

Lauffs, Hans-Georg; Jacques, Harald, and Sureck, Achim. Praktikum Sensorsysteme: gesteuerte Spannungs und Stromquellen. Internship Instructions, 2011.

Leue, C.; Hering, F.; Geißler, P., and Jähne, B. Segmentierung von Partikelbildern in der Strömungsvisualisierung. In Jähne, B.; Geißler, P.; Haußecker, H., and Hering, F., editors, *Proceedings of 18th DAGM-Symposium Mustererkennung*, Informatik Aktuell, pages 118–129, 1996.

Liberzon, A.; Gurka, R., and Hetsroni, G. XPIV-multi-plane stereoscopic particle image velocimetry. *Experiments in Fluids*, 36:355–362, 2004.

Lumsdaine, Andrew and Georgiev, Todor. The focused plenoptic camera. In *IEEE International Conference on Computational Photography*, pages 1–8, 2009.

Martin, W. and Flandrin, P. Wigner-Ville spectral analysis of nonstationary processes. *Acoustics, Speech and Signal Processing, IEEE Transactions on*, 33(6):1461–1470, 1985. ISSN 0096-3518. doi: 10.1109/TASSP.1985.1164760.

McGregor, TJ; Spence, DJ, and Coutts, DW. Laser-based volumetric colour-coded three-dimensional particle velocimetry. *Optics and lasers in engineering*, 45(8):882–889, 2007.

Müller, D.; Müller, B., and Renz, U. Three-dimensional particle-streak tracking (PST) velocity measurements of a heat exchanger inlet flow. *Experiments in Fluids*, 30(6):645–656, 2001. ISSN 0723-4864. doi: 10.1007/s003480000242.

Ng, R.; Levoy, M.; Brédif, M.; Duval, G.; Horowitz, M., and Hanrahan, P. Light field photography with a hand-held plenoptic camera. *Computer Science Technical Report CSTR*, 2, 2005.

Niegel, Daniel. Messung konvektionsgetriebener Transfergeschwindigkeit von Sauerstoff an der Luft-Wasser-Grenzfläche. Bachelor thesis, Institut für Umweltphysik, Fakultät für Physik und Astronomie, Univ. Heidelberg, 2010.

Nobach, H.; Damaschke, N., and Tropea, C. High-precision sub-pixel interpolation in particle image velocimetry image processing. *Experiments in Fluids*, 39:299–304, 2005. doi: 10.1007/s00348-005-0999-z.

Nyquist, H. Certain factors affecting telegraph speed. *Bell System Technical Journal*, 3:324, 1924.

Obukhov, AM. On the distribution of energy in the spectrum of turbulent flow. In *Doklady Akademii Nauk SSSR*, volume 32, pages 22–24, 1941.

Otte, M. Elastic registration of fmri data using bezier-spline transformations. *IEEE Transactions on Medical Imaging*, 20(2):193–206, February 2001.

Pereira, F.; Gharib, M.; Dabiri, D., and Modarress, M. Defocusing PIV: a three component 3D DPIV measurement technique. Application to bubbly flows. *Experiments in Fluids*, 29: S78–S84, 2000.

Pereira, F.; Lu, J.; Castaño Graff, E., and Gharib, M. Microscale 3D flow mapping with μDDPIV. *Experiments in Fluids*, 42:589–599, 2007. doi: 10.1007/s00348-007-0267-5.

Perez Nava, F. and Luke, J.P. Simultaneous estimation of super-resolved depth and all-in-focus images from a plenoptic camera. In *3DTV Conference: The True Vision - Capture, Transmission and Display of 3D Video, 2009*, pages 1 –4, may 2009. doi: 10.1109/3DTV. 2009.5069675.

Perwass, C. The next generation of photography. *White Paper, www.raytrix.de*, 2011.

Piccardi, M. Background subtraction techniques: a review. In *Systems, Man and Cybernetics, 2004 IEEE InternationalConference on*, volume 4, pages 3099–3104. Ieee, 2004.

Prandtl, L. *Strömungslehre*. Vieweg, 1957.

Prasad, A. K. Stereoscopic particle image velocimetry. *Experiments in Fluids*, 29:103–116, 2000.

Raffel, Markus; Willert, Christian E., and Kompenhans, Jürgen. *Particle image velocimetry*. Springer, Berlin ; Heidelberg [u.a.], 1998. ISBN 3-540-63683-8.

Raytrix GmbH, . Raytrix model: R11. Data Sheet, January 2012. URL `http://www.raytrix. de/tl_files/downloads/R11_GigE.pdf`.

Richardson, Lewis F. Atmospheric diffusion shown on a distance-neighbour graph. *Proceedings of the Royal Society of London. Series A*, 110(756):709–737, 1926. doi: 10.1098/rspa.1926. 0043. URL `http://rspa.royalsocietypublishing.org/content/110/756/709.short`.

Rosenstiel, Marcus and Rolf-Rainer Grigat, . Segmentation and classification of streaks in a large-scale particle streak tracking system. *Flow Measurement and Instrumentation*, 21(1): 1–7, March 2010. ISSN 0955-5986. doi: 10.1016/j.flowmeasinst.2009.10.001.

Salazar, A. On thermal diffusivity. *European journal of physics*, 24:351, 2003.

Salazar, Juan P. L. C. and Collins, Lance R. Two-particledispersion in isotropicturbulent flows. *Annual Review of Fluid Mechanics*, 41(1):405+, 2009. doi: 10.1146/annurev.fluid.40.111406. 102224. URL `http://dx.doi.org/10.1146/annurev.fluid.40.111406.102224`.

Schröder, A. and Kompenhans, J. Investigation of a turbulent spot using multi-plane stereo particle image velocimetry. *Experiments in fluids*, 36(1):82–90, 2004.

Schröder, Andreas; Geisler, Reinhard; Elsinga, Gerrit; Scarano, Fulvio, and Dierksheide, Uwe. Investigation of a turbulent spot and a tripped turbulent boundary layer flow using time-resolved tomographic piv. *Experiments in Fluids*, 44:305–316, 2008. ISSN 0723-4864. URL `http://dx.doi.org/10.1007/s00348-007-0403-2`. 10.1007/s00348-007-0403-2.

Schumacher, Jörg. Lagrangian studies in convective turbulence. *Physical Review E*, 79:056301, May 2009. doi: 10.1103/PhysRevE.79.056301. URL `http://link.aps.org/doi/10.1103/ PhysRevE.79.056301`.

Sheng, J.; Malkiel, E., and Katz, J. Using digital holographic microscopy for simultaneous measurements of 3d near wall velocity and wall shear stress in a turbulent boundary layer. *Experiments in Fluids*, 45:1023–1035, 2008. ISSN 0723-4864. URL `http://dx.doi.org/10.1007/s00348-008-0524-2`. 10.1007/s00348-008-0524-2.

Sinha, S. K. and Kuhlman, P. S. Investigating the use of stereoscopic particle streak velocimetry for estimating the three-dimensional vorticity field. *Experiments in Fluids*, 12:377–384, 1992. ISSN 0723-4864. URL `http://dx.doi.org/10.1007/BF00193884`. 10.1007/BF00193884.

Smith, Julius O. *Mathematics of the Discrete Fourier Transform (DFT)*. W3K Publishing, 2007. ISBN 978-0-9745607-4-8. URL `https://ccrma.stanford.edu/~jos/mdft/mdft.html`.

Sony Electronics Inc., . XCL-5005 B/W. Data Sheet, February 2008. URL `http://pro.sony.com/bbsc/assetDownloadController/XCL-5005_5005CR_final.pdf`.

Taylor, GI. Diffusion by continuous movements. *Proceedings London Mathematical Society*, 20 (2):196–211, 1922.

Tennekes, H. and Lumley, J. L. *A First Course in Turbulence*. MIT Press, Cambridge,MA, 14th edition, 1992. First Edition: 1972.

Tricomi, F.G. On the finite Hilbert Transformation. *The Quarterly Journal of Mathematics*, 2(1):199–211, 1951. doi: 10.1093/qmath/2.1.199. URL `http://qjmath.oxfordjournals.org/content/2/1/199.short`.

Tropea, Cameron; Yarin, Alexander L., and Foss, John F. *Springer Handbook of Experimental Fluid Dynamics*. Springer, Berlin, Heidelberg, 2007. doi: 10.1007/978-3-540-30299-5.

Tsallis, C. Possible generalization of boltzmann-gibbs statistics. *Journal of statistical physics*, 52(1):479–487, 1988.

Turney, D. E.; Anderer, A., and Banerjee, S. A method for three-dimensional interfacial particle image velocimetry (3D-IPIV) of an air-water interface. *Measurement Science and Technology*, 20(4):045403; 1–12, April 2009. doi: 10.1088/0957-0233/20/4/045403.

Vikas, R.; Conrad, S.; Brian C, L., and others, . A low-complexity algorithm for static background estimation fromcluttered image sequences in surveillance contexts. *EURASIP Journal on Image and Video Processing*, 2011, 2010.

Voss, B. and Garbe, C. S. Novel strategy for water sided interfacial 3d3cflow-visualization using a single camera. In *14th International Symposium on Flow Visualization*, pages D1–018, Daegu, Korea, 2010.

Voss, Björn; Stapf, Julian; Berthe, André, and Garbe, Christoph S. Bichromatic Particle Streak Velocimetry bPSV. *Experiments in Fluids*, 2012. submitted.

Voss, Björn; Heinlein, Alexander; Jähne, Bernd, and Garbe, Christoph. A new approach for 3c3d measurements of aqueous boundary layer flows relative to the wind-wave undulated interface. In *6th Int. Symp. Gas Transfer at Water Surfaces, Kyoto, May 17–21, 2010*, 2010. poster.

Voth, G.A.; La Porta, A.; Crawford, A.M., and J.and BodenschatzAlexander, E. Measurement of particle accelerations in fully developedturbulence. *Journal of Fluid Mechanics*, 469:121–160, 2002.

Wanner, S.; Fehr, J., and Jähne, B. Generating epi representations of 4d light fields with a single lens focused plenoptic camera. *Advances in Visual Computing*, pages 90–101, 2011.

Wanninkhof, Rik; Asher, William E.; Ho, David T.; Sweeney, Colm, and McGillis, Wade R. Advances in quantifying air-sea gas exchange and environmental forcing. *Annual Review of Marine Science*, 1:213–244, 2009. doi: 10.1146/annurev.marine.010908.163742.

Wernet, Mark P. Planar particle imaging doppler velocimetry: a hybrid piv/dgv technique for three-component velocity measurements. *Measurement Science and Technology*, 15(10): 2011, 2004. URL `http://stacks.iop.org/0957-0233/15/i=10/a=011`.

Willert, C. E. and Gharib, M. Three-dimensional particle imaging with a single camera. *Experiments in Fluids*, 12:353–358, 1992.

Wung, T.S. and Tseng, F.G. A color-coded particle tracking velocimeter with application to natural convection. *Experiments in Fluids*, 13(4):217–223, 1992. ISSN 0723-4864. URL `http://www.springerlink.com/content/w4625h282mh6u312/fulltext.pdf`.

A Appendix

A.1 Data-sheets of the LED-Arrays

Figure A.1: Technical specification of the violet LED-Array (ENFIS UNO Tile Array Violet 405 nm; ENFIS LIMITED, Swansea, SA18PJ, UK) given in the data sheet of the manufacturer (ENFIS Ltd., 2008a).

ENFIS UNO Tile Array Blue 465nm

Technical Specification

Electro-Optical Characteristics

Item	Min	Typ	Max
Rated Current If (mA)		2350	
Forward Voltage Vf (Volts)	14	16	20
Peak Wavelength λp (nm)	450	465	470
Dominant Wavelength λd (nm)	455	470	475
Spectral Width Δλ (nm)	15	23	30
Total Radiant Flux ΦR (mW)	4000	6070	
Radiant Flux Density ΦR/A (mW/cm^2)	8000	12140	
Total Luminous Flux ΦL (Lumens)	220	350	
Luminous Flux Density ΦL/A (lm/cm^2)	440	700	
Total Electrical Power P (W)		38	

All measurements performed at a heatsink temperature of 25°C

Spectral Data

Peak @ 455 nm
FWHM 25 nm

Angular Distribution

LIV Graph

P-I
V-I

Figure A.2: Technical specification of the violet LED-Array (ENFIS UNO Tile Array Blue 465 nm; ENFIS LIMITED, Swansea, SA18PJ, UK) given in the data sheet of the manufacturer (ENFIS Ltd., 2008b).

A.2 Non-Uniformities of the CCD-sensor
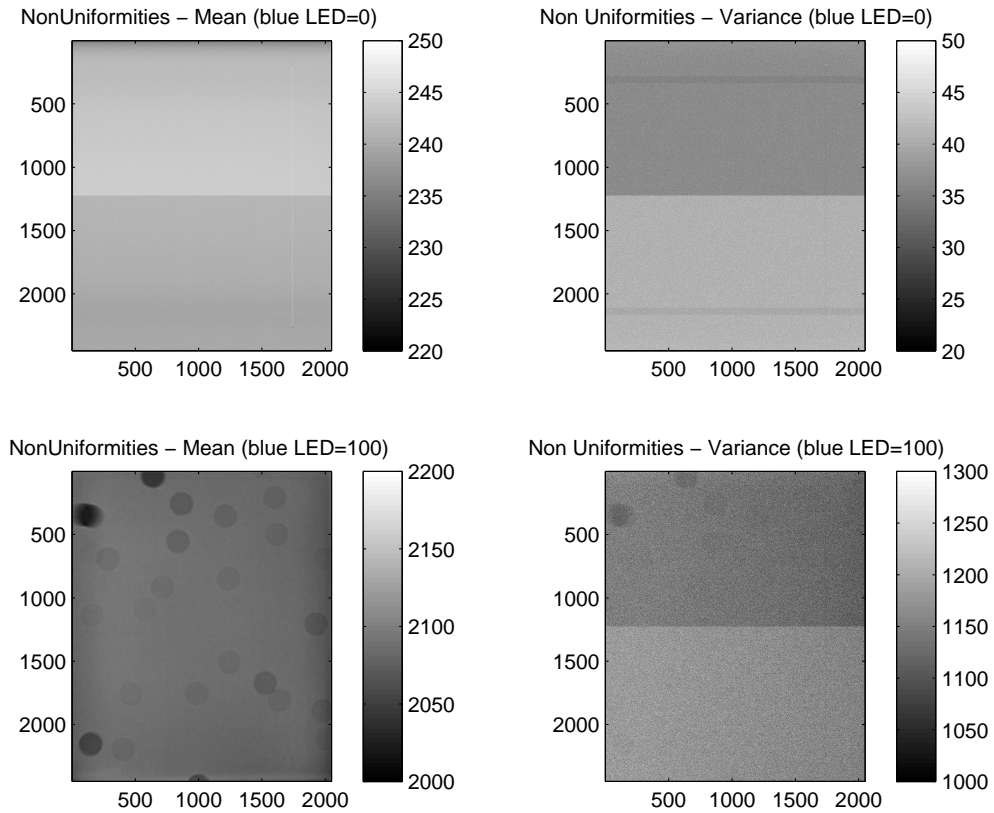
Figure A.3: Sensor non-uniformities of the used CCD measured with the EMVA1288 calibration setup. Since the camera is used to record the scattered light of a blue and a violet LED array, only the non-uniformities from the 'blue'-calibration are shown in this study. The upper row illustrates the result of the 'dark'-measurement. The lower row shows a some circular spatial non-uniformities of the *overall system gain K* that may be caused by manufacturing imperfections.

A.3 35mm Macro Objective

For FA/Machine Vision
Fixed Focal

HF35SA-1

Applicable camera (model)

| 1 | 2/3 | 1/2 | 1/3 | 1/4 |

FIXED Fixed Focal | **5 Mega** For Megapixel Camera | **MANUAL** Manual Iris | **C-mt** C Mount | **METAL** Metal Mount | **F1.4** Wide Aperture Rate
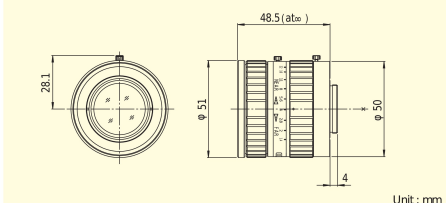
NEW

- High-resolution design, providing support for up to 5 megapixel camera resolution.
- Wide-aperture (F1.4) design achieves clear images under low light intensity.
- Enhanced image recognition accuracy achieved by reduction of distortion and improvement of illumination uniformity.
- Robust enclosure resistant to vibrations and shocks. Equipped with locking knobs for the iris and the focus.

48.5 (at ∞)

28.1 φ 51 φ 50

4

Unit : mm

Focal Length (mm)		35
Iris Range		F1.4 ~ F22
Operation	Focus	Manual
	Iris	Manual
Angle Of View (H× V)	2/3"	14°20′ × 10°46′
	1/2"	10°27′ × 7°51′
	1/3"	7°51′ × 5°53′
Focusing Range (From Front Of The Lens) (m)		∞ ~ 0.2
Object Dimensions at M.O.D. (H× V) (mm)	2/3"	50 × 38
	1/2"	37 × 27
	1/3"	27 × 21
Back Focal Distance (in air) (mm)		14.99
Exit Pupil Position (From Image Plane) (mm)		−37
Filter Thread (mm)		M49 × 0.75
Mount		C
Mass (g)		185

Remarks
· With Metal Mount
· With Locking Knob for Iris and Focus

Figure A.4: Data-sheet of the used Fujinon HF35SA-1 2/3" 35mm camera objective

A.4 Focused Plenoptic Camera R11

Specifications	
Max. 2D resolution	3 megapixel
Depth of field factor	up to 6 times of standard cameras
Video frame rate	6.2 fps at full resolution (CameraLink: 10 fps)
Light field resolution	10.7 Megarays
Aperture	F=8 (constant), **we offer full customization**
3D depth resolution	>100 different layers
Readout frequency	28 MHz
Dimensions (W x H x D)	2.76" x 2,80" x 2.10"
Weight	300 g
Power consumption	external 12 V DC, 2 A, 12 W
Operation temperature	-10°C (non condensing) to +40°C
Operation humidity	5% - 95%, non-condensing
Shutter	global shutter
Auto exposure	automatic / manual
White balance	automatic / manual
Gain	programmable / 1 to >3x optimizable
Interface	GigE Ethernet, Camera Link optional
Lens mount	F-mount / M 58 x 0.75 mount / Nikon / Canon
Integration time	130 µs to 2 sec
Image sensor	43.3mm large format interline 10.7MP CCD, color/mono

Figure A.5: Data-sheet of the *focused plenoptic camera* (Model: R11, Raytrix GmbH, Kiel, Germany) Raytrix GmbH (2012).

A.5 Circuit Board of the *Operational-Transconductance-Amplifier* (OTA)
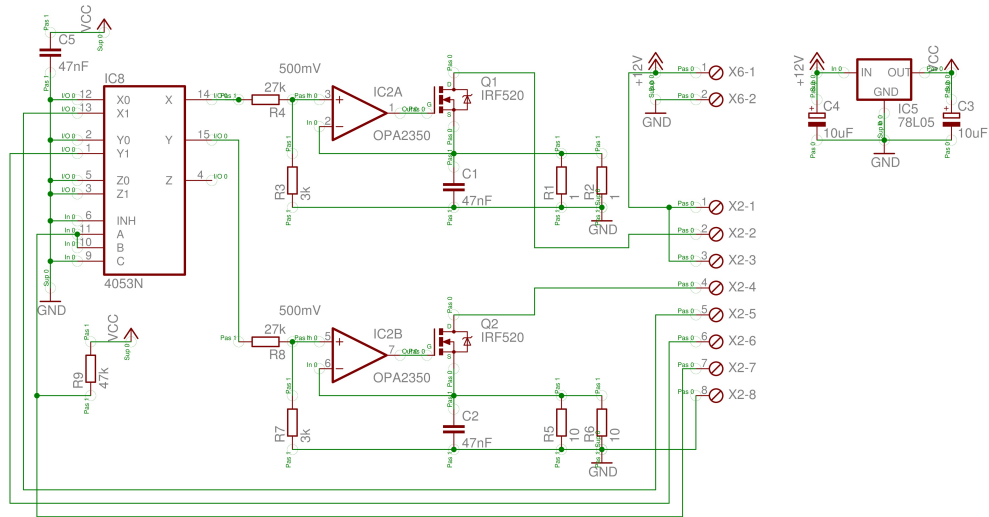
Figure A.6: Circuit Board of the *Operational-Transconductance-Amplifier* (OTA) that was built to drive the LED-arrays

A.6 microEnable IV VD4-CL framegrabber

Bezeichnung	microEnable IV VD4 CL	Produkteigenschaften			
		Bildpuffer	512 MB	Kamera Standard	Camera Link
		Bildaufnahme	FPGA System Prozessor	Kamerastecker	2* MDR26
		Bildverarbeitung	FPGA Vision Prozessor	Formate	BASE, DualBASE MEDIUM, FULL, FULL 10taps
		Übertragsungsrate	900 MB/s	Pixeltakt	85 MHz
		PC Interface	PCIe x4	Kameratyp	Flächenkameras Zeilenkameras
		AddOn Produkte	GPIO/Trigger Board GPIO/Trigger Board, optoisoliert CLIO PixelPlant	Sensortyp	Graustufen, 8 16bit Farbsensor (RGB), 24 48bit
		Software Produkte (Lieferumfang)	microDisplay microDiagnostics microEnable SDK	Applet Unterstützung (Lieferumfang)	Acquisition Applets SmartApplets (Base) VisualApplets (Base)
Hardware Kompatibilität	microEnable IV FULL x4	Treiberunterstützung für Betriebssysteme (Lieferumfang)	Windows XP, 32bit / 64bit Windows Vista, 32bit / 64bit Windows 7, 32bit / 64bit Linux (Kernel 2.6), 32bit / 64bit	Applet Unterstützung optional	SmartApplets Extended VisualApplets 1D/2D Blob VisualApplets JPEG
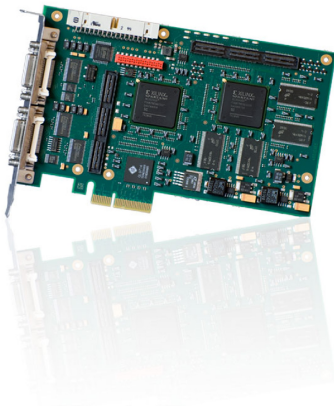
Figure A.7: microEnable IV VD4-CL frame grabber (SILICONSOFTWARE GmbH, Mannheim, Germany)

Danksagung

Erklärung gemäß § 8(3)b) und c) der Promotionsordnung

Hiermit erkläre ich, dass ich in die vorliegende Dissertation selbstständig verfasst und mich dabei keiner anderen als der von mir ausdrücklich bezeichneten Quellen und/oder Hilfen bedient habe. Des Weiteren bestätige ich hiermit, dass ich an keiner anderen Stelle ein Prüfungsverfahren beantragt, bzw. diese Dissertation in der vorliegenden oder anderer Form bereits anderweitig verwendet oder einer anderen Fakultät als Dissertation vorgelegt habe.

Björn Magnus Voß